2 Euratom fusion programme

2.1 Theory and modelling

Calculation of radiation profiles inside the separatrix in DEMO reactor

Roman Stankiewicz (roman.stankiewicz@ipplm.pl) Irena Ivanova-Stanik, Roman Zagórski Institute of Plasma Physics and Laser Microfusion

Abstract

The reduction of power load to divertor plates to acceptable level by impurity radiation becomes essential for future tokamak reactor. Code Corediv [1,2] has been used to analyzed sputtered and seeded impurity radiation for several demo design concepts. The sputtering of tungsten from divertor plates by all ions is considered. Corediv solves self-consistently the transport equation in the core and SOL (scrape off layer and divertor) regions. The coupling between both region is imposed by continuity of the value and respective fluxes of the solutions at the separatrix. In the core the 1D radial equations for densities of bulk ions and of each ionization states of impurity ions together with equations for electron and ion temperatures are solved. In SOL, EPIT code[3] is used with 2D fluid equations of Braginskii type for densities, momentum for each ions, electron temperature and common for all ions temperature. The coupling between two region takes into the interaction between sputtered and seeded impurity. It turned out that the seeded impurities radiation is very small but the seeded impurity play essential role in tungsten sputtering.

Introduction

The DEMO1 design concepts obtained by using system code has been analyzed [4]. The dependence of radiation on the concentration of seeded impurity (Argon) was analyzed. In the core the transport coefficients are the sum of anomalous and neoclassical contributions. In the core anomalous transport relies on the energy confinement scaling law. More precisely the ion and electron conductivity are defined by the formula:

$$\chi_e^{an} = \chi_i^{an} = C_e \frac{a^2}{\tau_e} \left(0.25 + 0.75 \left(\frac{r}{a} \right)^4 \right) FSB(r)$$

where a is the minor radius, τ_e is energy confinement time calculated from scaling law(IPB98(y,2))[5] and the function FSB describes the conductivity drop near separatrix. The constant C_e is adjusted to keep the calculated confinement time obtained from solution equal to the value defined by scaling law. For all ions we used the same anomalous transport coefficient for ions defined by

$$D_i^{an} = 0.35 \chi_i^{an}$$
 , $V_i^{pinch} = -C_p \left(\frac{\tau_e}{2.8}\right)^2 D_i^{an} \frac{r}{a^2}$

The typical diffusion coefficient and velocity pinch profiles are shown on Fig.1 and Fig.2.The dependence of radiation profiles on the value of pinch velocity has been also studied.

In SOL, 2D EPIT code based on Braginskii [5] is used. The SOL region is approximated by simple slab geometry (poloidal and radial direction) with poloidal classical transport and anomalous in radial direction (D_i = χ_i =0.5 χ_c =0.25 m²/s). An analytical description of neutrals is employed which takes into account recycling of bulk ions and seeded impurities and sputtering processes at the target plates. The recycling coefficients are external parameters. The energy losses due to energy exchange with deuterium atoms as well as due to atomic processes (ionization, recombination and charge exchange) are taken into account. Schematically the integration domain and SOL and boundary condition are shown on Fig.3.

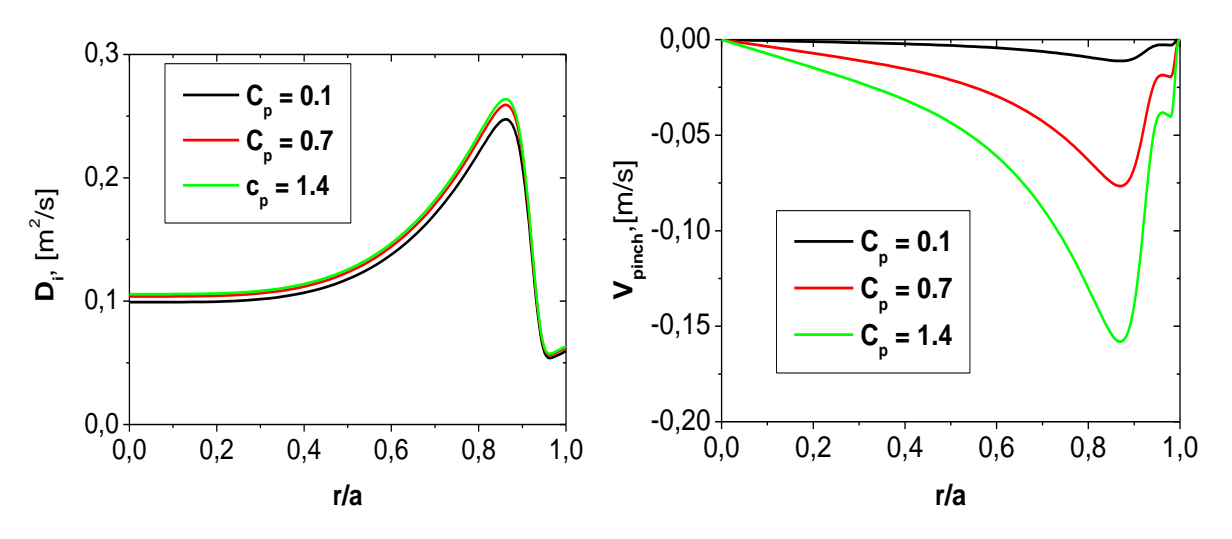


Fig. 1. Anomalous diffusion coefficient profile

Fig. 2. Velocity pinch.

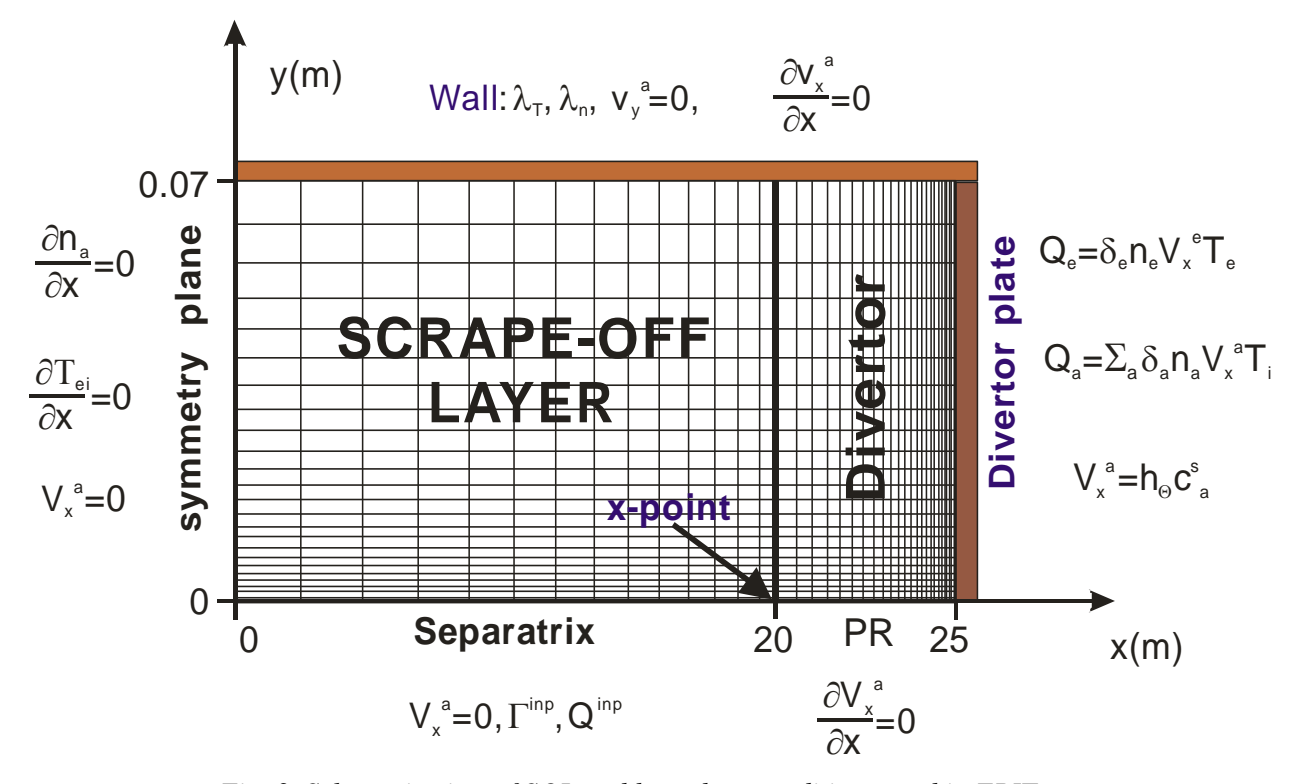


Fig. 3. Schematic view of SOL and boundary conditions used in EPIT.

Numerical simulation of DEMO1 design concept presented in [5]

The basic parameters for the design presented in [5] obtained by Process and COREDIV are shown in Table 1.

Table 1. Global parameters for P_{inj} =50*MW*(*yellow color*). *and for* P_{inj} =100*MW* (*blue color*)

The basic plasma parameters for DEMO with auxiliary heating 50MW and 100 MW as function of Argon concentration are compared on Fig. 4 and Fig. 5.

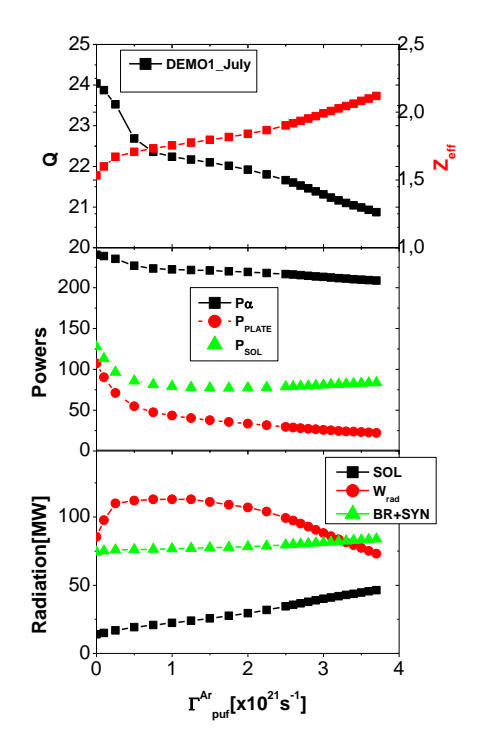
The difference between the alpha power and the power to plates is almost constant for high concentration of Argon. It means that the total radiated power remains constant and the reduction of power load to target plates is caused by alpha power reduction mostly due to dilution of plasma. Consequently the Q factor is also reduced. The concentration of argon can be increase to certain level above which the solution does not exist. The reason for this limits is not fully clear. The possible explanation , supported by the numerical results, can be summarized as follows:

- It is observed, that helium concentration increases together with the increase of the seeding intensity and at some puffing level burning is stopped by plasma dilution by helium.
- The termination of the solution is very sharp and caused by the negative feedback which starts

• The termination of the	Solution 18	very snarp	anu causeu	by the nega	ilive recuba	ick willen si	aris
Fusion power, P _{fus} (MW)	1572	1200	1095	1040	1350	1240	1175
Auxiliary current drive	0.0	0.	0	0.	0.	0	0.
fraction							
Auxiliary heating, P _{inj} (MW)	50.0	50.	50.	50.	100	100	100
P _{synch} (MW)	28.3	46	45	45	50	50	50
P _{brem} (MW)	74.5	27	33	39	37	39	46
P _{line} (MW)	84.0	67	67	67	108	134	118
H-mode threshold, P _{L-H}	136±42.						
(MW)		91	91	91	91	91	91
Confinement time, $\tau_{E}(s)$	2.92	2.44	2.57	2.65	2.07	2.16	2.21
H-factor	1	1	1	1	1	1	1
Power to divertor (MW)	250.2	131	79	85	150	89	96
$n_{e}(0)/< n_{e}>$	1.5	1.09	1.09	1.09	1.09	1.09	1.09
$T_{e}(0)/< T_{e}>$	2.5	2.63	2.59	2.55	2.55	2.75	2.66
Separatrix density (10 ²⁰ m ⁻³)	0.36	0.44	0.44	0.44	0.4.3	0.44	0.44
Parameter	Process	COR	COR	COR	COR	COR	COR
AR gas_puff (10 ²¹ s ⁻¹)		5E17	2.0E21	3.7E21	5E17	2.0E21	3.7E21
R ₀ , a (m)	9.0,2.25	9.0,2.25	9.0,2.25	9.0,2.25	9.0,2.25	9.0,2.25	9.0,2.25
Plasma current, I _P (MA)	14.0	14.0	14.0	14.0	14.0	14.0	14.0
Elongation, κ ₉₅	1.56	1.56	1.56	1.56	1.56	1.56	1.56
Triangularity, δ95	0.33						
Safety factor, q ₀ ,q ₉₅	1.0,3.0	1.0,3.0	1.0,3.0	1.0,3.0	1.0,3.0	1.0,3.0	1.0,3.0
Temperature, $\langle T_{e,vo}l \rangle$ (keV)	10.5	12.7	12.4	12.4	13.8	13.6	1.36
Z _{eff}	1.98	1.53	1.84	2.12	1.57	1.82	2.21
Helium fraction	0.1	0.029E	0.046E	0.046	0.0287	0.0445	0.0432
Power to plate (MW)		107	33	22	121	40	27

when the puffing limit is exceeded:

• Increase of Γ_{puff} leads to decrease of P_{α} and increase of helium confinement time τ_{HE} and helium concentration c_{HE} and due to dilution P_{α} is reduced.



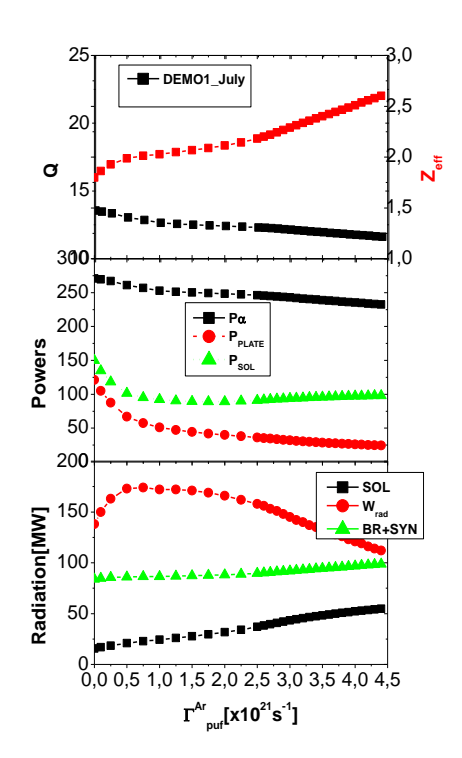


Fig. 4. Plasma parameters versus gas puff levels for P_{inj} =50MW: Q-factor and Z_{eff} ,) alpha power, power to target plate P_{PLATE} , and P_{SOL} , power radiated by SOL, W_{RAD} and brem+syn.

Fig. 5. Plasma parameters versus gas puff levels for P_{inj} =100MW: Q-factor and Z_{eff} ,) alpha power, power to target plate P_{PLATE} , and P_{SOL} , power radiated by SOL, W_{RAD} and brem+syn.

The profiles of densities and temperatures dependence on gas puff of Argon intensity is presented on Fig. 6 for auxiliary heating 50 MW and the impurity concentration and radiation profiles on Fig. 7.

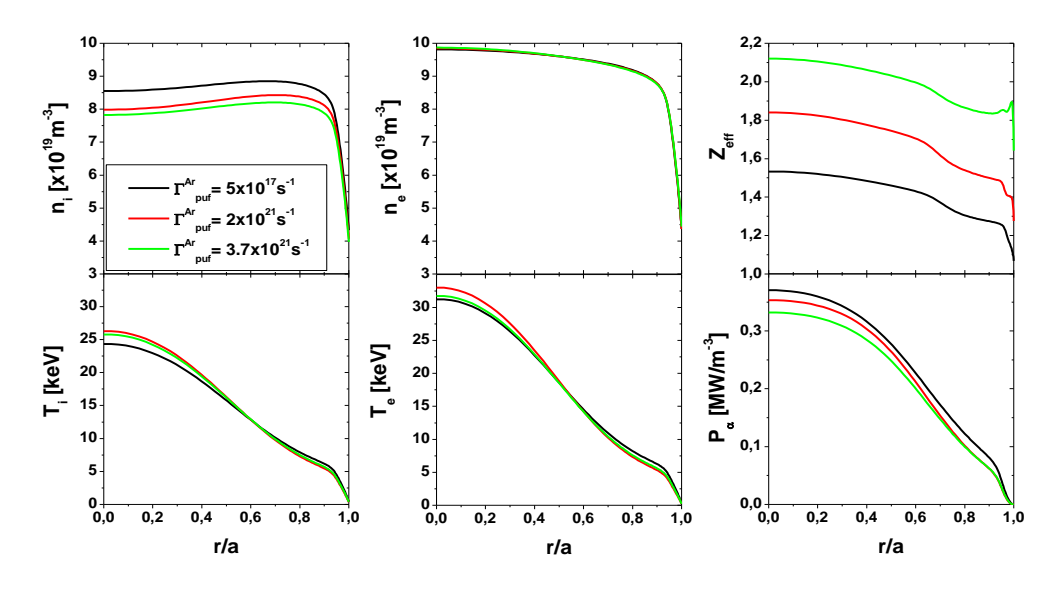


Fig. 6. The profiles of densities and temperatures, Z_{eff} and the alpha power for various argon gas puff and P_{inj} =50 M

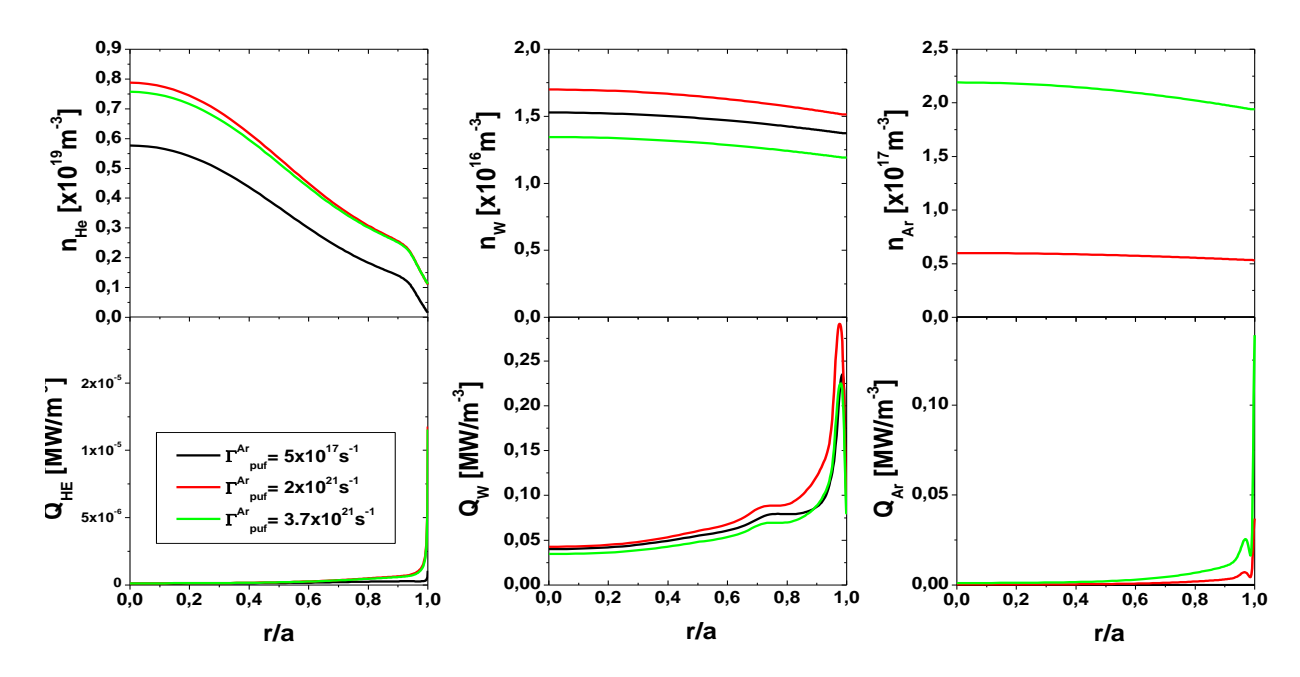


Fig. 7. The concentration and radiation profiles for various argon gas puff for P_{inj} =50MW

The profiles of densities and temperatures dependence on gas puff of Argon intensity is presented on Fig. 8 for auxiliary heating 100 MW and the impurity concentration and radiation profiles on Fig. 9.

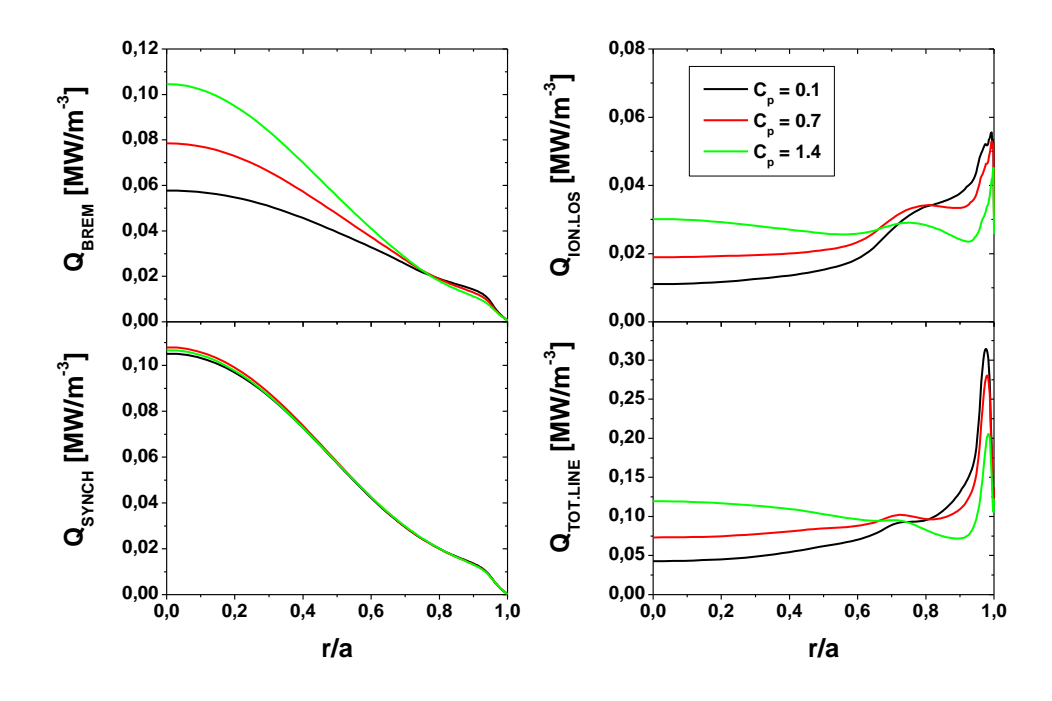


Fig. 8. The profiles of densities and temperatures, Z_{eff} and the alpha power for various argon gas puff and $P_{inj}=100 \text{ MW}$

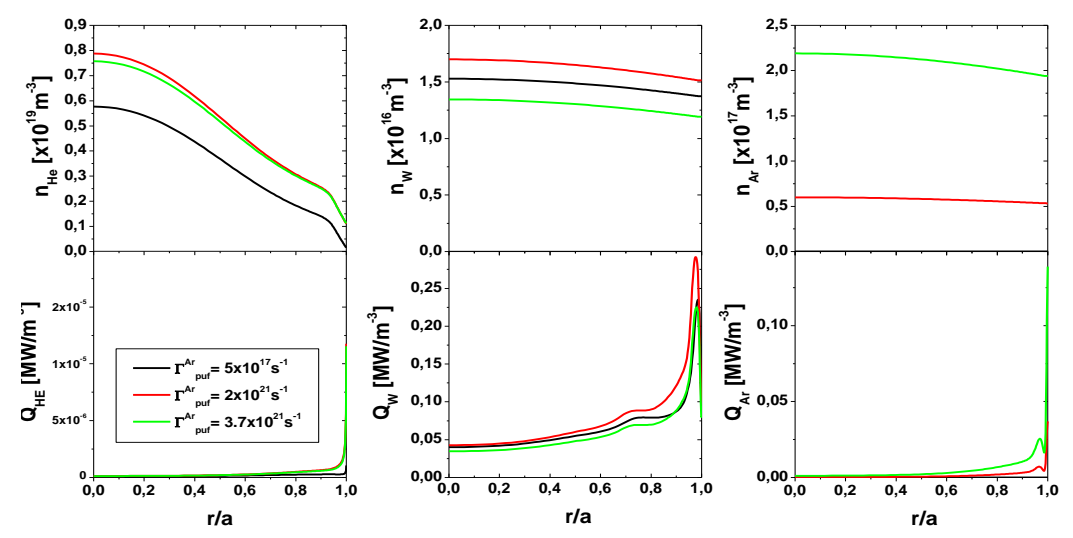


Fig. 9. The concentration and radiation profiles for various argon gas puff for P_{inj} =50MW

The line radiations is dominated by the tungsten radiation (>90%) and the line radiation is localized in the region closed to separatrix.

The dependence of the plasma profile on the velocity pinch has been studied . The results for P_{inj} of the numerical analysis for argon gas puff intensity $2.10^{-21} s^{-1}$ and P_{inj} are shown in Figs. 10-12.

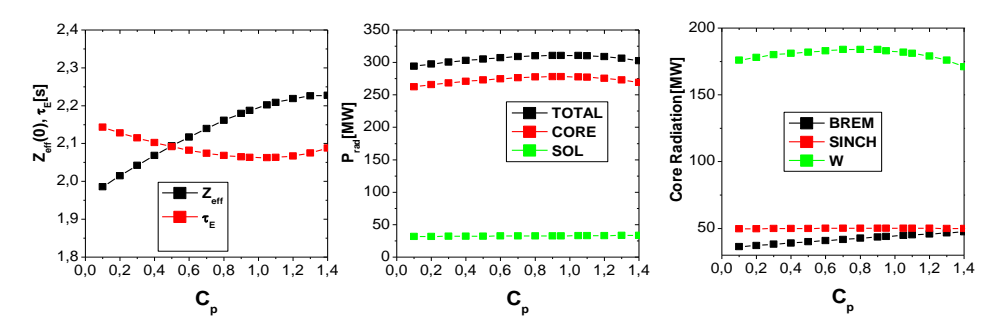


Fig. 10. The dependence of Zeff, τe , the total radiations in the core and SOL, and the core radiation for various processes.

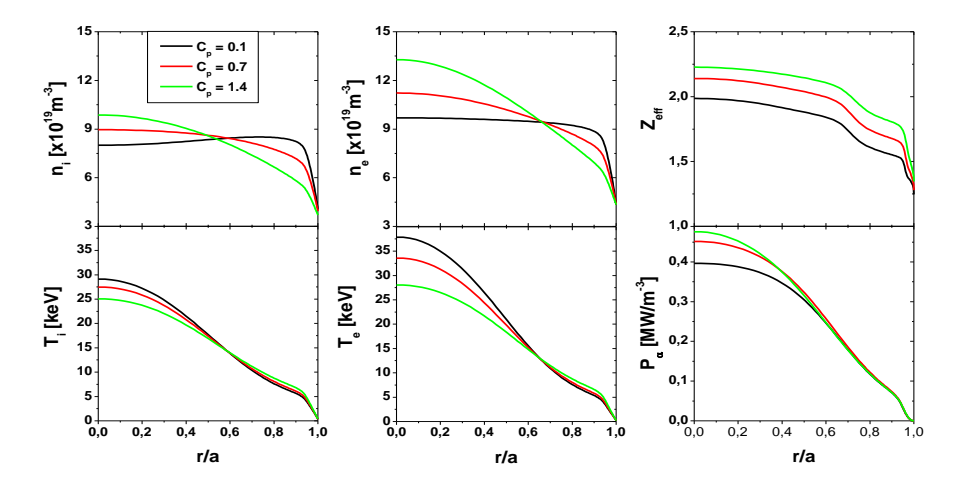


Fig. 11. Plasma profiles

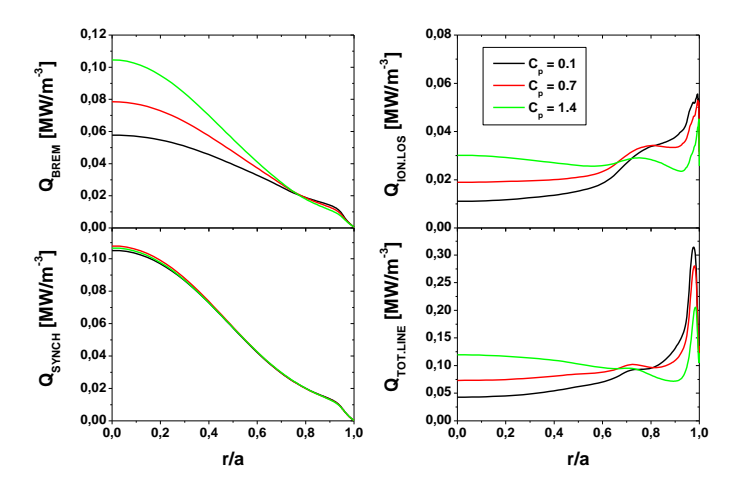


Fig. 12. Radiation profiles

The modification of inward pinch velocity for c_p increasing from 0.1 to 1.4 corresponds to peaking factor variation from 1.07 to 1.44. The line radiation of tungsten in the centre of plasma increases significantly.

Conclusions

The radiation dependence on the seeded impurity concentration has been studied numerically.

The concentration of argon can be increased to certain level above which the solution does not exist. The reason for this limits is not fully clear. The possible explanation , supported by the numerical results, can be summarized as follows:

- It is observed, that helium concentration increases together with the increase of the seeding intensity and at some puffing level burning is stopped by plasma dilution by helium.
- The termination of the solution is very sharp and caused by the negative feedback which starts when the puffing limit is exceeded:
- Increase of Γ_{puff} leads to decrease of P_{α} and increase of helium confinement time τ_{HE} and helium concentration c_{HE} and due to dilution P_{α} is reduced.

The power load to divertor plates can be significantly reduced. The reduction corresponds to the same reduction of alpha power caused mostly by dilution of plasma and consequently to the reduction of Q factor. The line radiation is dominated by tungsten (>:90%) and line radiation is localized in the region closed to separatrix. The introduction of the inward velocity pinch leads to increase of the line radiation in the region far from the separatrix.

Collaboration

Association EURATOM - IPP

Association EURATOM - CEA

Association EURATOM - CCFE

Association EURATOM - ENEA

References

- [1] R.Stankiewicz, R. Zagórski Czechoslovak J. of Phys. 52 Suppl.D (2002) 32
- [2] R.Stankiewicz, R. Zagórski J.Nucl.Mater. 337-339 (2005) 32
- [3] R.Zagórski, J.Techn.Phus.37 No.1 (1996)
- [4] R.Kemp, EFDA Report WP11-SYS-01-ACT05; DEMO design concepts from PPPT SYS, 20012
- [5] S.I.Braginski Rev.Plasma Phys 1 (1965) 914.

Modelling of DEMO reactor with the help of COREDIV code

Roman Stankiewicz (roman.stankiewicz@ipplm.pl) Irena Ivanova-Stanik, Roman Zagórski Institute of Plasma Physics and Laser Microfusion

Abstract

The reduction of power loads to divertor plates to an acceptable level is a critical issue for future fusion reactors. The radiative exhaust of energy by sputtered and externally seeded impurities is considered as possible way of spreading energy over wall area.

The report describes integrated numerical modelling of DEMO discharges with tungsten divertor plates and argon and neon as seeded impurities with help of COREDIV code[1]. Since the energy balance depends strongly on the coupling between the bulk and the scrape-off layer plasma, modelling requires the transport problem to be addressed in both regions simultaneously. The COREDIV code self-consistently solves radial 1D energy and particle transport equations of plasma and impurities in the core region and 2D multifluid transport in the SOL. The model is fully self-consistent with respect to both the effects of impurities on the alpha power level and the interaction between seeded and intrinsic impurities. The sputtering of tungsten by seeded impurities leads to a significant change in the intrinsic impurity fluxes, and it is found to be essential for a correct evaluation of alpha power and radiation losses.

Introduction

Several DEMO design concepts has been analyzed with the help of COREDIV code, which describes self consistently the core and the scrape off layer with the divertor regions (SOL). The coupling between core and SOL is imposed by continuity condition at separatrix of values and fluxes of temperatures and densities. In the core the 1D transport equations for densities and temperatures are used. The EPIT code [2] is used to analyze the SOL domain. The SOL is describe by 2D fluid equations developed by Braginskii. In both domains it is assumed that all ions have the same temperature. All ionization states of impurity ions are considered separately in both domains. The sputtering processes of tungsten at target plate by all ions are taken into account. Several DEMO design concepts have been analyzed and they are described in [3,4].

Preliminary analysis of baseline DEMO Concepts (<u>WP11-SYS-01-ACT5-02/IPPLM/BS</u> and <u>WP11-SYS-01-ACT5-02/IPPLM/PS</u>)

We have considered the following DEMO concepts obtained with help system code Process:

- DEMO1, DEMO2, DEMO3 and DEMO4 configurations from [3]
- DEMO1 configuration from[4] proposed for two auxiliary power $P_{inj} = 50MW$ and $P_{inj} = 100MW$.

The basic parameters of analyzed DEMO designs from [3] are summarized in the Table.1. The global parameters calculated by Process and COREDIV for Demo1 are presented in Table.2 and for DEMO3 in Table.3 for three different levels of argon seeding.

Table.1 The basic global parameters of DEMO design by COREDIV code

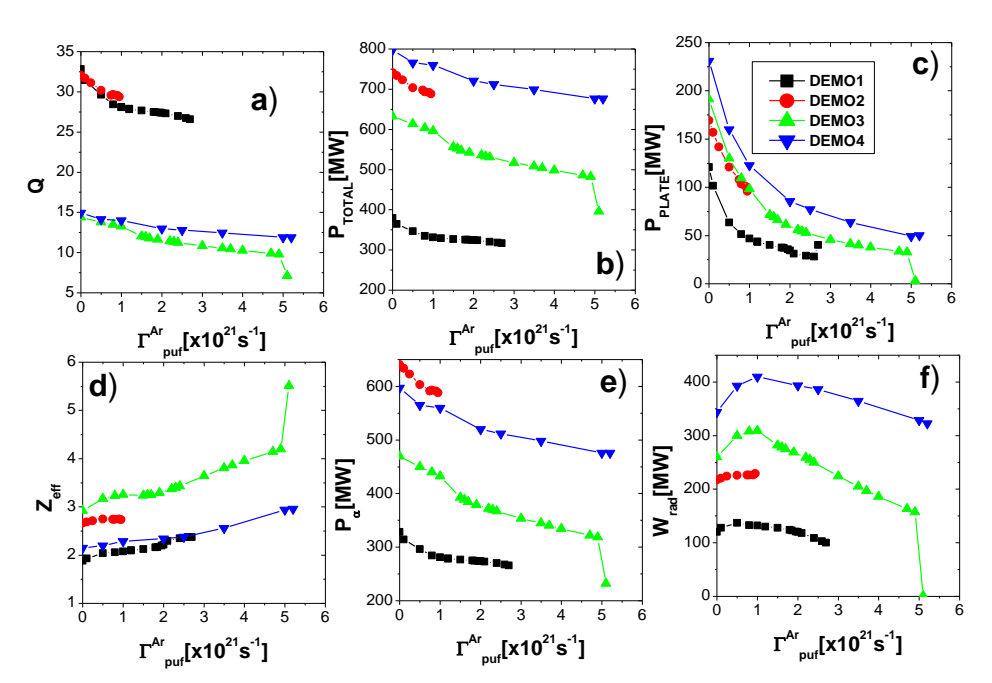
PARAMETERS	PULSED	PULSED		ГАТЕ
	DEMO1	DEMO 2	DEMO 3	DEMO 4
R ₀ , a (m)	9.0, 2.25	9.6, 2.4	8.5, 2.83	8.5, 2.83
Plasma current, I_P (MA)	16.44	18	19.75	23
Toroidal magnetic field, BT (T)	7.2	7.45	4.9	5.74
Density, $\langle n_{e, vol} \rangle$ (10 ²⁰ m ⁻³)	0.88	1	0.75	0.91
Separatrix density, n _{es} (10 ¹⁹ m ⁻³)	3.5	4	3.5	4
aH-factor (IPB98(y,2))	1	1.2	1.3	1.3
Auxiliary heating, P_{inj} (MW)	51.8	100	163	200

 $Table. 2. Parameters\ for\ Demo1$

Parameter	Process	COREDIV	COREDIV	COREDIV
AR gas_puff (s ⁻¹)		5 10 ¹⁷	1.2 10 ²¹	1.95 10 ²¹
R ₀ , a (m)	9.0,2.25	9.0,2.25	9.0,2.25	9.0,2.25
Plasma current, I _P (MA)	16.44	16.44	16.44	16.44
Elongation, κ ₉₅	1.66	1.66	1.66	1.66
Temperature, $\langle T_{e,vo}l \rangle$ (keV)	13.3	16.6	15.8	15.8
Z _{eff}	1.98	1.88	2.1	2.2
Helium fraction	0.1	0.045	0.72	0.72
Power to plate (MW)		120	43.6	37.2
Fusion power, P _{fus} (MW)	2119	1640	1395	1370
Auxiliary current drive fraction	0.005	0.0	0.0	0.0
Auxiliary heating, P _{inj} (MW)	51.8	50	50	50
P _{synch} (MW)	62.6	71	67	67
P _{brem} (MW)	78.1	39	42.	67
Pline (MW)	85.4	94	103	99
H-mode threshold, P _{L-H} (MW)	146±46.2	95	95	95
Confinement time, $\tau_E(s)$	2.98	2.48	2.73	2.76
H-factor	1	1	1	1
Power to divertor (MW)	250.2	148	86	86
$n_{e}(0)/< n_{e}>$	1.5	1.1	1.1	1.1
$T_{e}(0)/< T_{e}>$	2.5	2.3	2.3	2.3
Separatrix density (10 ²⁰ m ⁻³)	0.35	0.35	0.35	0.35

Table.3 Parameters for Demo3

Parameter	Process	COREDIV	COREDIV	COREDIV
AR gas_puff (s ⁻¹)		5 10 ¹⁶	$1.5 \ 10^{21}$	$2.2 \ 10^{21}$
R ₀ , a (m)	8.5,2.8	8.5,2.8	8.5,2.8	8.5,2.8
Plasma current, I _P (MA)	19.75	19.75	19.75	19.75
Safety factor, q ₀ ,q ₉₅	1.0,3.0	1.0,3.0	1.0,3.0	1.0,3.0
Temperature, $\langle T_{e,vo}l \rangle$ (keV)	17.6	23.1	21.8	21.6
Z _{eff}	2.71	2.92	3.24	3.37
Helium fraction	0.1	0.049	0.078	0.084
Power to plate (MW)		191	71.4	55.9
Fusion power, P _{fus} (MW)	1935	2445	1966	1850
Auxiliary current drive fraction	0.5969			
Auxiliary heating, P _{inj} (MW)	163	163	163	163
P _{synch} (MW)	57.5	57	55	54
P _{brem} (MW)	122.5	76	61	58
Pline (MW)	167.3	206	226	211
H-mode threshold, P _{L-H} (MW)	102.2+-32	71	71	71
Confinement time, τ_E (s)	3.81	2.51	2.74	2.81



In Fig. 1 the dependence of some plasma parameters on Argon gas puff intensity is shown.

Fig. 1. Plasma parameters versus gas puff levels: a) Q-factor, b) total radiation P_{TOTAL} c) power to target plate P_{PLATE} , d) Z_{eff} , e) alpha power, f) power radiated by $W^{RA}D$.

The following remarks follow from the calculation results presented in Fig. 1.

- In all cases significant amount of alpha power is produced but Q -factor is the highest (~ 30) for pulsed DEMO configurations (DEMO1-2) characterized by small additional heating.
- For steady state scenarios (DEMO3-4), relatively large additional heating is required to drive the plasma current and consequently Q factor is low (< 15).
- The increase of Ar influx is accompanied by increase of Z_{eff} and reduction of P_{α} and corresponding decrease of Q factor, due to dilution effect of argon and helium.
- The total plasma radiation depends very weakly on the argon influx, with majority of the radiation losses coming from the plasma core (> 90%, with significant Tungsten contribution (above 50%).
- The radiation in the SOL is usually small (< 10%), but sufficient to achieve high recycling or semi-detached conditions in the divertor.
- In the reactor with very high input powers, the plasma temperature at the target plates is set up mostly by the sputtering processes and remains slightly above the sputtering threshold for argon ions (5 eV).
- The low temperature conditions in the divertor do not guarantee strong enough reduction of the power to the target plates. Only for the highest seeding levels the heat load might be tolerable, mostly due to reduction of the input power (P_{α}) with increased seeding and not by cooling action of argon ions. We note however, that for strong seeding the power crossing the separatrix approaches the power threshold for L-H transition.

If the seeding impurity is changed from argon to neon the overall picture remains similar. In Fig. 2 the results of calculation for DEMO1 for Ar and Neon are compared.

For the steady state configurations (DEMO3-4) the input flux of additional impurity might be increased up to the level when the detached conditions in the divertor are achieved .In all cases, the maximum values of the seeding impurity puffing rate are relatively low, and consequently the contribution of the injected impurity ions to the total radiation is always small, even for detached plasmas.

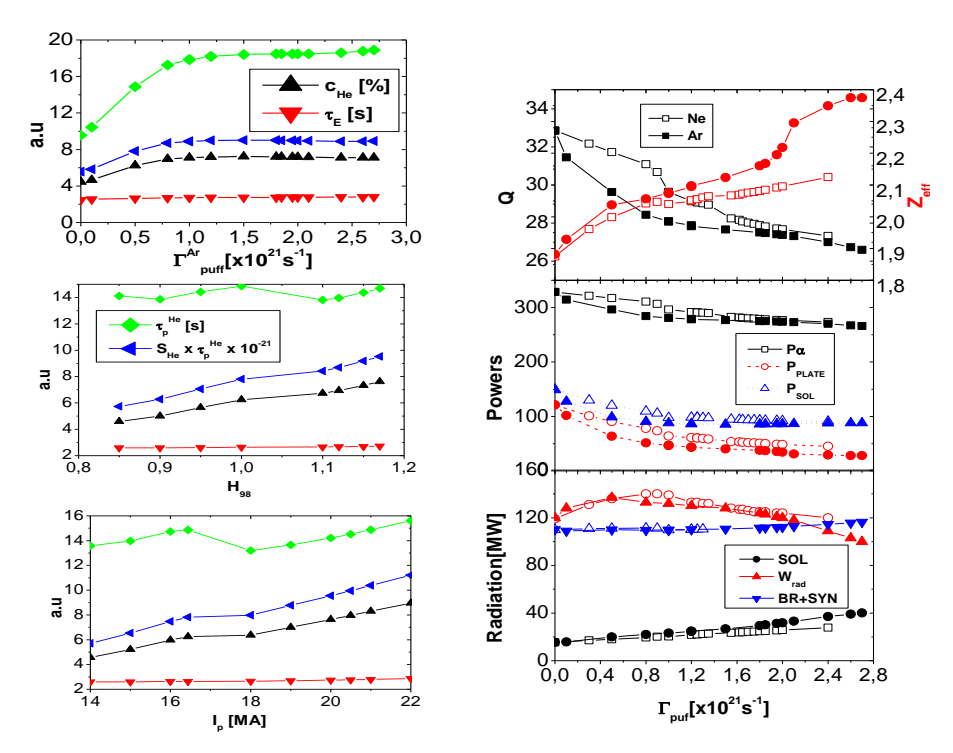


Fig. 2. DEMO1 parameters for different gas puff levels of Ar (full symbols) and Ne (open symbols).

Fig. 3. Helium concentration, confinement times for energy and helium, Helium, source multiplied by helium confinement time.

For pulsed DEMO configurations (DEMO1-2), we observe a maximum value of the allowed influx of seeded impurity above which the steady state solution does not exist. The reason for this limits is not fully clear. The possible explanation , supported by the results shown in Fig.3, can be summarized as follows:

- It is observed, that helium concentration increases with the increase of the seeding intensity and at some puffing level burning is stopped by plasma dilution by helium.
- The termination of the solution is very sharp and caused by the negative feedback which starts when the puffing limit is exceeded.
- Increase of Γ_{puff} leads to decrease of P_{α} and increase of helium confinement time τ_{HE} and helium concentration c_{HE} and due to dilution P_{α} is reduced.
- The product S_{He} X τ_E which drives the helium concentration is growing strongly with puffing. Although the increase of τ_E is quite moderate (from 2.48 sec up to 2.76 sec), the corresponding change to τ_{HE} is quite drastic (9.6 sec \rightarrow 18.5 sec) and the reason is still to be identified.
- In fact, there are different physics processes in the loop which lead to the instability and it is difficult to find out which one is the most important.
- Careful analysis of the simulation results indicates that the improvement of the plasma confinement seems to be the main driver for the instability.
- In order to check this hypothesis we have performed simulations for different confinement condition. At the fixed argon puff level ($\Gamma_{puff}^{Ar}=5 \times 10^{20} s^{-1}$), numerical scans were done with different H_{98} factors and plasma currents (I_p).
- It appears, that steady state solution does not exist if the maximum values of H_{98} (= 1.17) and I_p (= 22 MA) are exceeded.
- These results show that improved plasma confinement in the fusion reactor might lead to strong helium accumulation.

More information about the solution is presented in the next graphs:

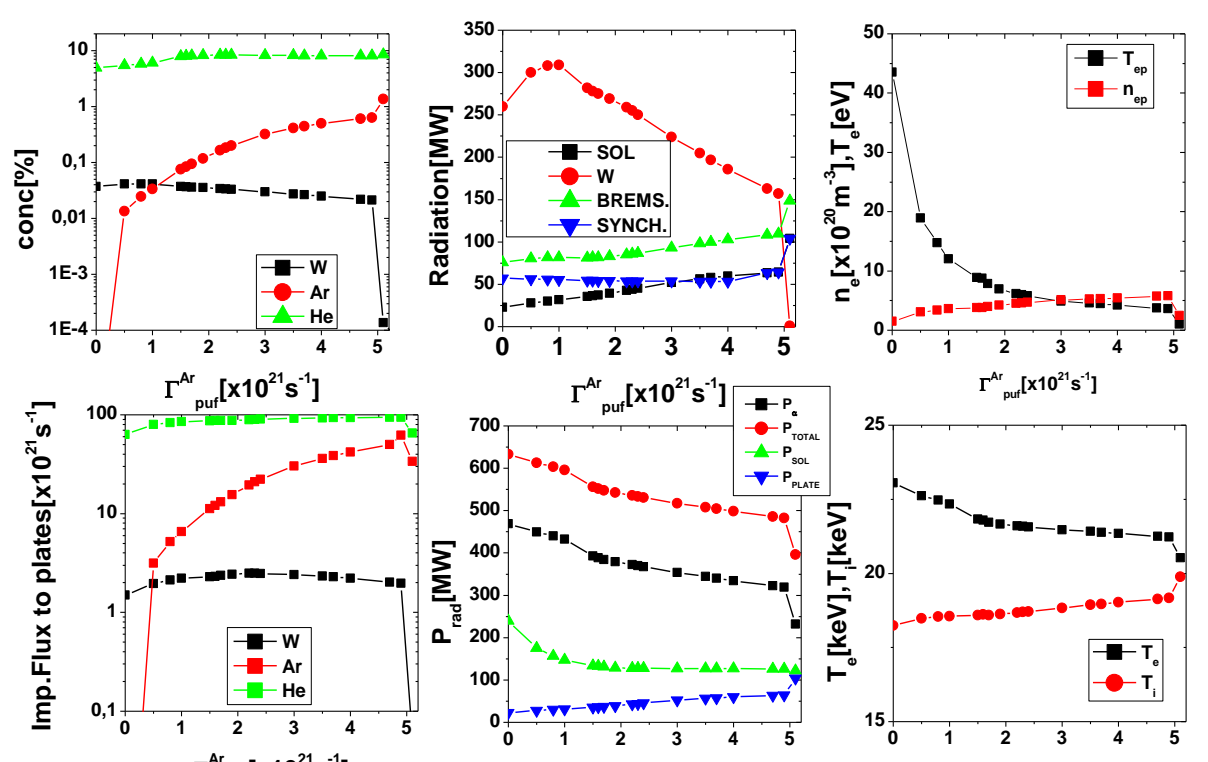


Fig. 5. **DEMO1** Dependence of plasma parameters on the seeded impurity influx (Argon).

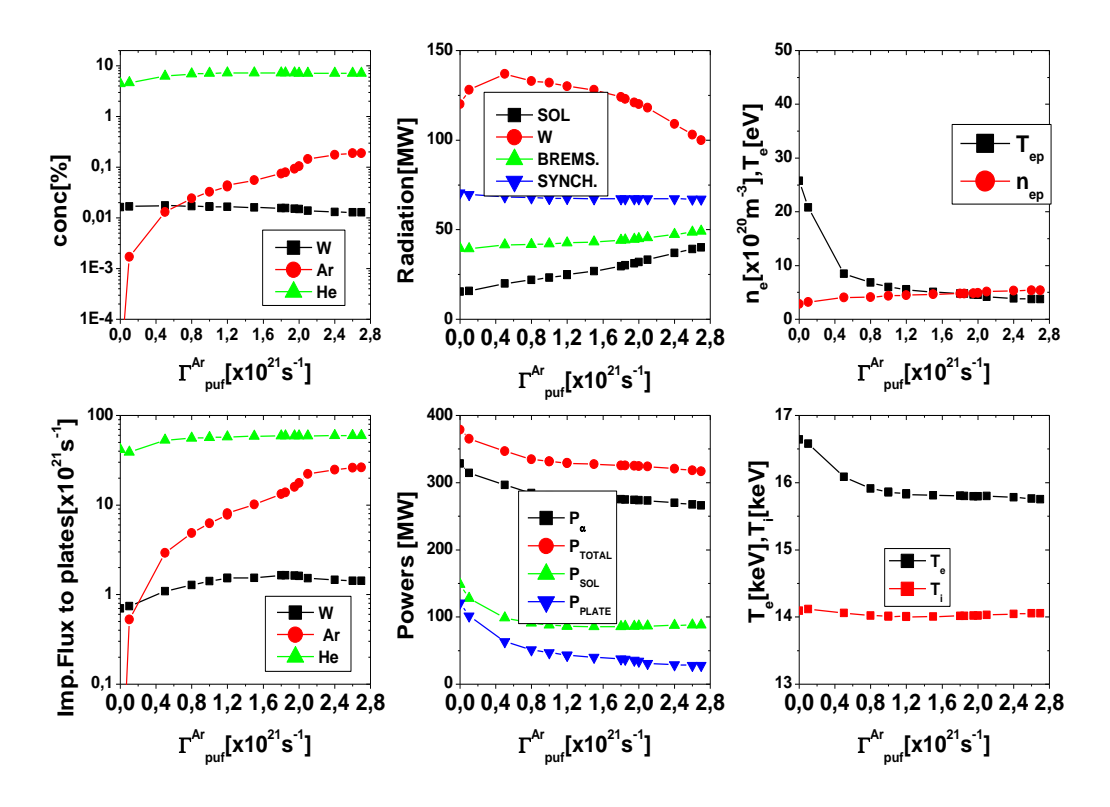


Fig. 4. Dependence of plasma parameters on the seeded impurity influx (Argon).

The global parameters calculated by Process and COREDIV for P_{inj} =50MW and 100MV for DEMO1 design concepts described in [4] are presented in Table. 4. The results of Process are given only for P_{ini} =50 MW.

Table4. Global parameters for P_{inj} =50*MW*(*yellow color*). *and for* P_{inj} =100*MW* (*blue color*)

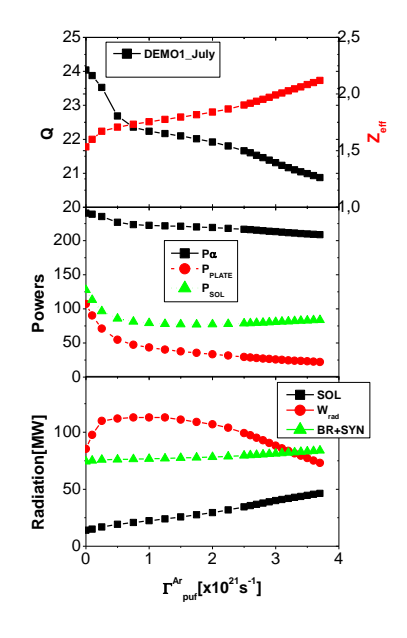
There are some differences between the results of Process and COREDIV. For example, the

Parameter	Process	COR	COR	COR	COR	COR	COR
AR gas_puff (10 ²¹ s ⁻¹)		5E17	2.0E21	3.7E21	5E17	2.0E21	3.7E21
R ₀ , a (m)	9.0,2.25	9.0,2.25	9.0,2.25	9.0,2.25	9.0,2.25	9.0,2.25	9.0,2.25
Plasma current, I _P (MA)	14.0	14.0	14.0	14.0	14.0	14.0	14.0
Elongation, κ ₉₅	1.56	1.56	1.56	1.56	1.56	1.56	1.56
Triangularity, δ95	0.33						
Safety factor, q ₀ ,q ₉₅	1.0,3.0	1.0,3.0	1.0,3.0	1.0,3.0	1.0,3.0	1.0,3.0	1.0,3.0
Temperature, $\langle T_{e,vo}l \rangle$	10.5						
(keV)		12.7	12.4	12.4	13.8	13.6	1.36
$Z_{ m eff}$	1.98	1.53	1.84	2.12	1.57	1.82	2.21
Helium fraction	0.1	0.029E	0.046E	0.046	0.0287	0.0445	0.0432
Power to plate (MW)		107	33	22	121	40	27
Fusion power, P _{fus} (MW)	1572	1200	1095	1040	1350	1240	1175
Auxiliary current drive	0.0	0.	0	0.	0.	0	0.
fraction							
Auxiliary heating, P _{inj}	50.0	50.	50.	50.	100	100	100
(MW)							
P _{synch} (MW)	28.3	46	45	45	50	50	50
P _{brem} (MW)	74.5	27	33	39	37	39	46
P _{line} (MW)	84.0	67	67	67	108	134	118
H-mode threshold, P _{L-H}	136±42.						
(MW)		91	91	91	91	91	91
Confinement time, $\tau_E(s)$	2.92	2.44	2.57	2.65	2.07	2.16	2.21
H-factor	1	1	1	1	1	1	1
Power to divertor (MW)	250.2	131	79	85	150	89	96
$n_{e}(0)/< n_{e}>$	1.5	1.09	1.09	1.09	1.09	1.09	1.09
$T_{e}(0)/< T_{e}>$	2.5	2.63	2.59	2.55	2.55	2.75	2.66
Separatrix density (10 ²⁰	0.36						
m ⁻³)		0.44	0.44	0.44	0.4.3	0.44	0.44

difference in core line radiation is quite big. This can be probably attributed to differences in the impurity densities, which are defined in COREDIV by sputtering processes. The lover radiation in COREDIV can be connected with lower temperature in COREDIV with comparison to that obtained in Process. This point should be discussed and the differences might be reduced by proper definition of conditions imposed in calculation in both codes. There is also big difference in density peaking factor and this will be discussed in the next section.

The basic plasma parameters for DEMO with auxiliary heating 50MW and 100MW are compared in Fig. 5 and Fig. 6.

It can be observed that that for large gas puff levels the difference between the alpha power and the power to the SOL corresponding to the total radiation losses is almost constant. It means that the reduction of power to the SOL results only from the reduction of the bulk ions density due to increase the impurity concentration (dilution effect).



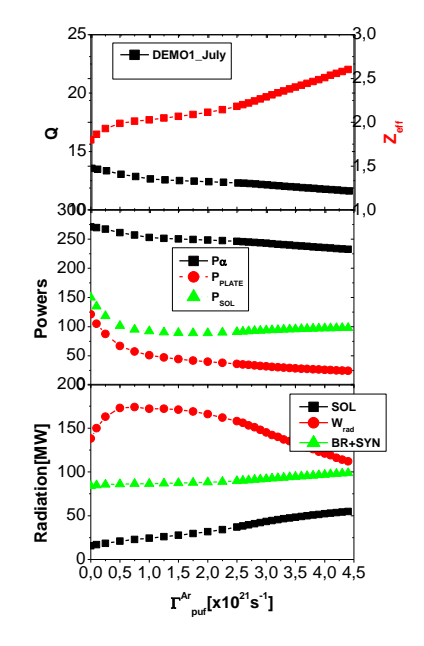


Fig. 5. Plasma parameters versus gas puff levelswith P_{inj} =50MW: Q-factor and Z_{eff} ,) alpha power, power to target plate P_{PLATE} , and P_{SOL} , power radiated by SOL, W_{RAD} and brem+syn.

Fig. 6. Plasma parameters versus gas puff levelswith P_{inj} =50MW: Q-factor and Z_{eff} ,) alpha power, power to target plate P_{PLATE} , and P_{SOL} , power radiated by SOL, W_{RAD} and brem+syn.

Check the consistency of the density, temperature and impurity concentration profiles for both DEMO options (WP12-SYS-02-T02-01/IPPLM)

The plasma parameters versus the seeded impurity influx(Argon) are presented in Fig.7 and Fig.8 for $P_{inj} = 50$ MW and $P_{inj} = 100$ MW, respectively. In Fig.9 and Fig.10. we present profiles of the electron and ion density, electron and ion temperatures, Z_{eff} and the radiation power.

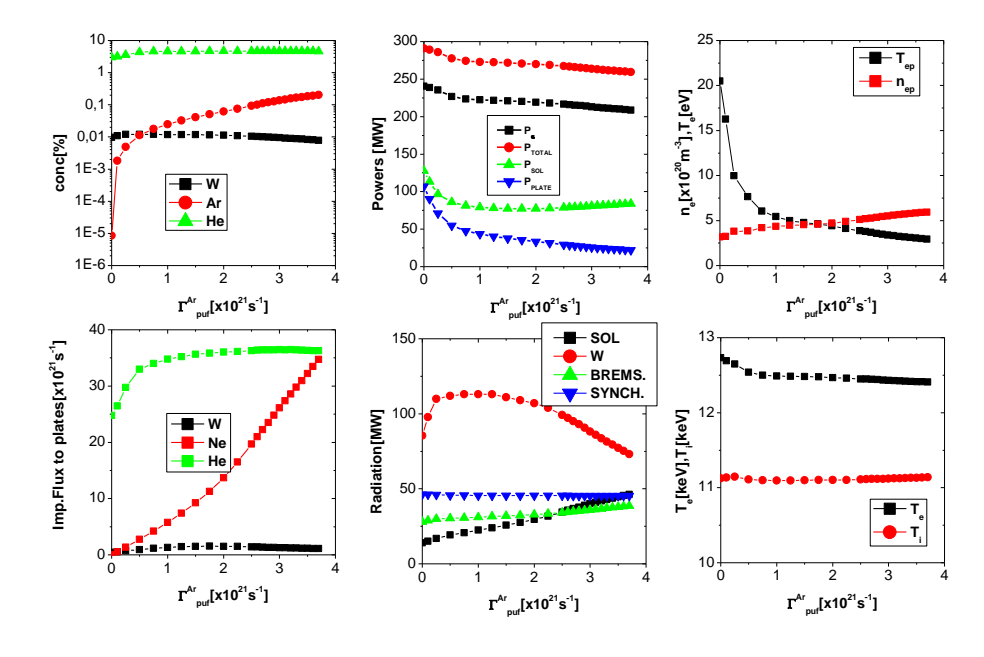


Fig. 7. Plasma parameters versus the seeded impurity influx (Argon) Pinj=50MW)

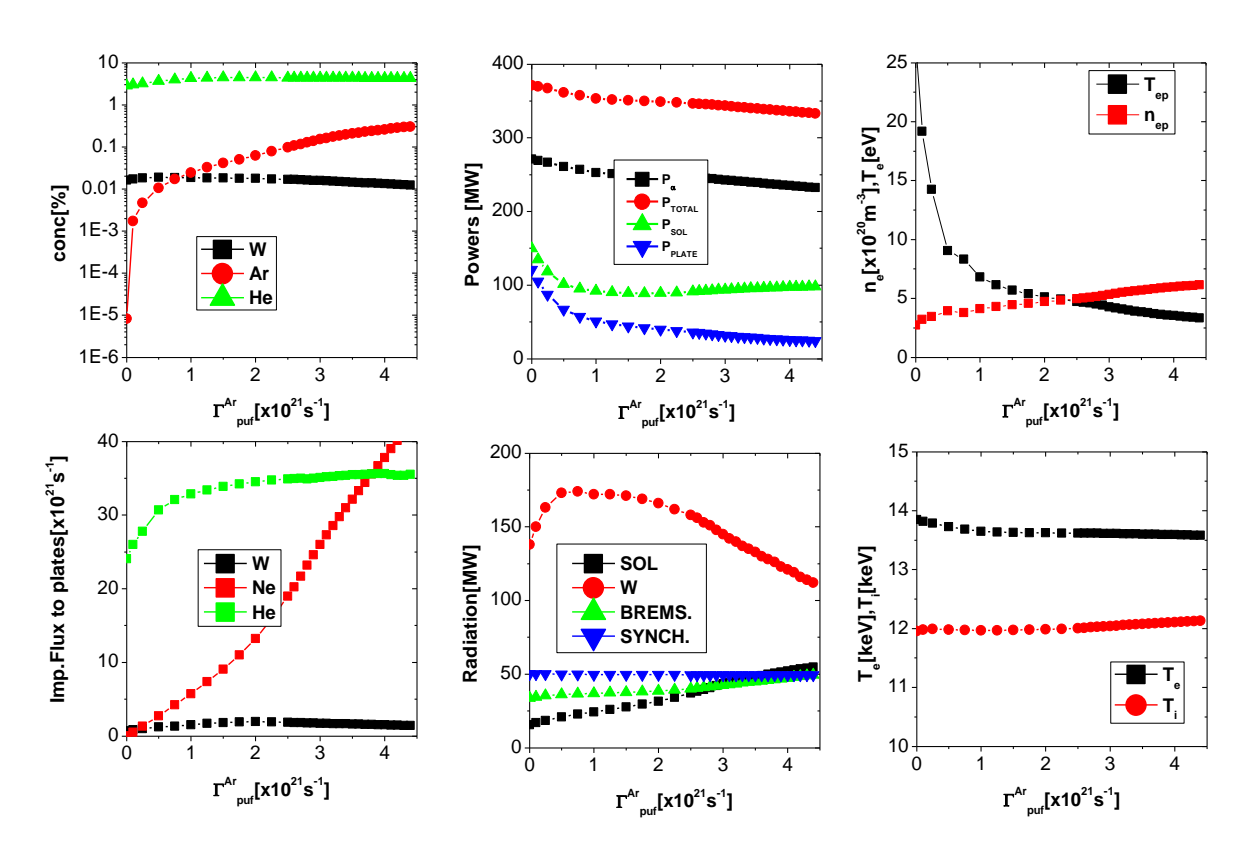


Fig. 8. Plasma parameters versus the seeded impurity influx (Argon) Pinj=100MW.

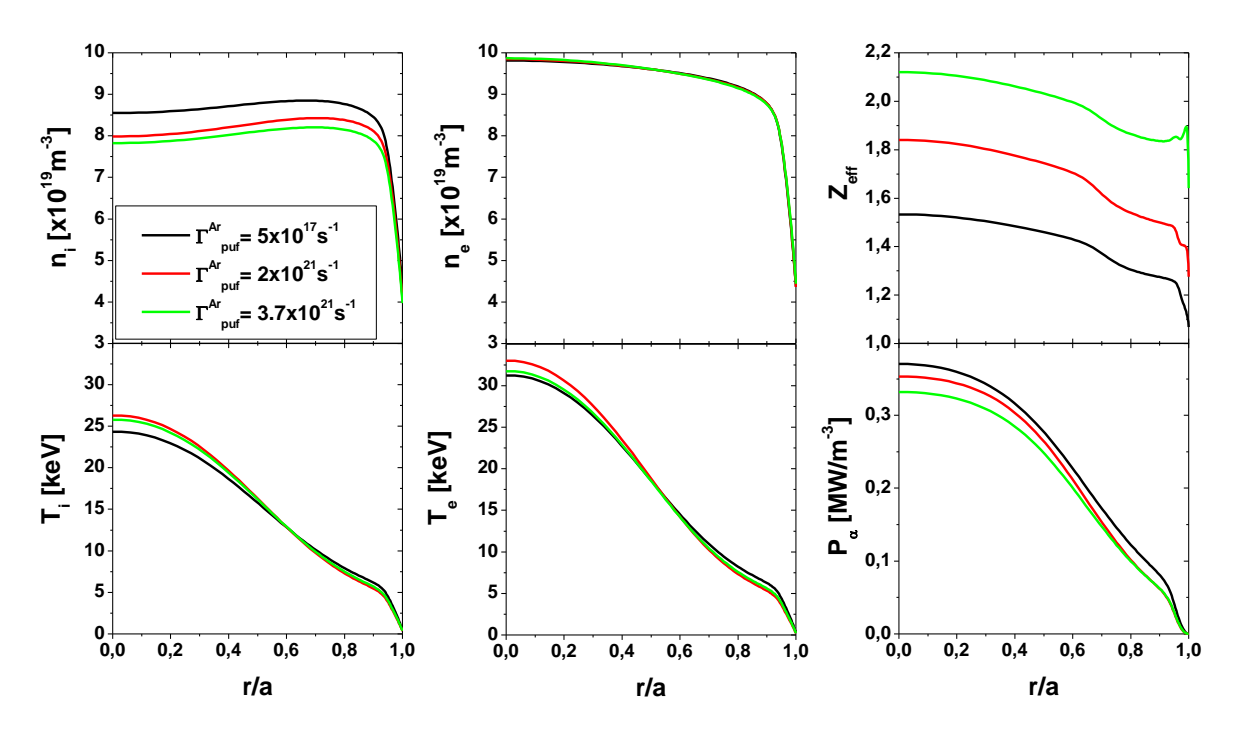


Fig. 9. Plasma profiles for P_{inj} =50MW.

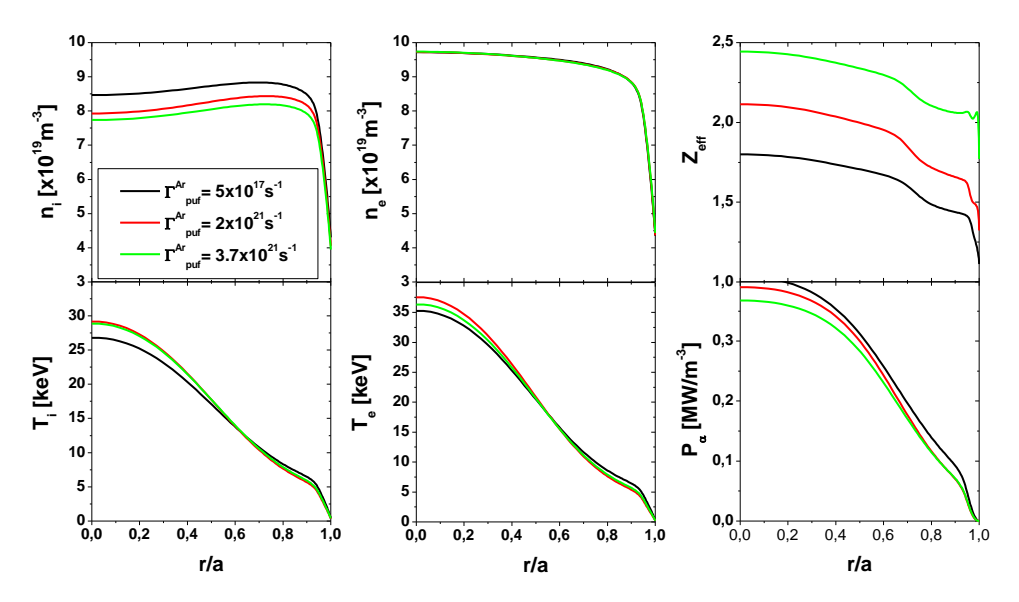


Fig. 10. Plasma profiles for $P_{inj}=100MW$.

Sensitivity analysis (WP12-SYS-02-T03-01/IPPLM)

- We have considered: the possibility of increase peaking factor by increasing the pinch velocity
- the dependence of the global parameters on anomalous transport models.

1. Numerical analyses of the influence of the inward velocity on the DEMO parameters

The density peaking factor as obtained by COREDIV standard simulations is smaller, than those obtained in calculation performed by Process. The possibility of increasing the pinch factor (C_p) by modifying the pinch velocity has been studied. The results are summarized in Table 4.

modifying the pinch velocity has been studied. The results are summarized in Table 4.	
Table 4. Results by COREDIV for different pinch velocity	

Parameter	Process	COREDI	COREDIV	COREDIV	COREDIV	COREDIV	COREDIV
AR gas_puff (s ⁻¹)		$2 \times 10^{21} \mathrm{s}^{-1}$	$2 \times 10^{21} \text{s}^{-1}$	$2 \times 10^{21} \text{s}^{-1}$	2 x 10 ²¹ s ⁻¹	$2 \times 10^{21} \text{s}^{-1}$	$2 \times 10^{21} \text{s}^{-1}$
Cp (pinch factor)		0.1	0.2	0.4	0.5	0.75	0.85
R ₀ , a (m)	9.0,2.25	9.0,2.25	9.0,2.25	9.0,2.25	9.0,2.25	9.0,2.25	9.0,2.25
Plasma current, I _P	14.0	14.0	14.0	14.0	14.0	14.0	14.0
Elongation, κ ₉₅	1.56	1.56	1.56	1.56	1.56	1.56	1.56
Triangularity, δ95	0.33						
Safety factor, q ₀ ,q ₉₅	1.0,3.0	1.0,3.0	1.0,3.0	1.0,3.0	1.0,3.0	1.0,3.0	1.0,3.0
Temperature, <t<sub>e,vol></t<sub>	10.5	12.47	12.32	11.97	12.18	11.98	11.88
$Z_{ m eff}$	1.98	1.74	1.80	1.91	1.82	1.87	1.88
Helium fraction	0.1	0.046	0.051	0.064	0.056	0.067	0.072
Power to plate (MW)		34	33.6	31.8	34.75	33.75	33.19
Fusion power, P _{fus}	1572	1105	1115	1107	1190	1208	1204
Auxiliary current drive	0.0	0.0	0.0	0.0	0.0	0.0	0.

Auxiliary heating, P _{inj}	50.0	50.	50.	50.	50.	50.	50.
P _{synch} (MW)	28.3	45.55	45.58	45.39	46.28	46.42	46.38
P _{brem} (MW)	74.5	30.78	32.08	34.6	34.49	36.82	37.62
P _{line} (MW)	84.0	114.6	116.18	113.25	124.33	124.05	121.63
H-mode threshold,	136±42.	91.	92.	93.7	93.7	95.3	96.
Confinement time, τ_E	2.92	2.56	2.55	2.56	2.46	2.44	2.44
H-factor	1	1	1	1	1	1	1
Power to divertor	250.2	79.79	79.72	78.8	83.6	84.95	85.75
$n_{\rm e}(0)/< n_{\rm e}>$	1.5	1.09	1.14	1.25	1.25	1.35	1.4
$T_{e}(0)/< T_{e}>$	2.5	2.67	2.59	2.42	2.48	2.35	2.29
Separatrix density (10 ²⁰ m ⁻³)	0.36	0.36	0.36	0.36	0.36	0.36	0.36

The green part of the table corresponds to cases when the pinch velocity is applied to all ion, whereas results in blue corresponds to situation where pinch velocity is applied only for bulk ions. The maximum value of density peaking factor ($n_e(0)/< n_e>$) achieved in calculation was 1.3 and was smaller than 1.5 assumed in Process (the results of Process code are given for $P_{inj}=50$ MW). The pinch velocity in COREDIV has been defined by the following formula:

$$V_j^{pinch} = -C_p \left(\frac{\tau_e}{2.8}\right)^2 D^{an} \frac{r}{a^2} \cdot$$

where au_E is the energy confinement time and D^{an} is the anomalous diffusion coefficient.

2. <u>Numerical analyses of the dependence of the global parameters on anomalous transport models</u>

In the COREDIV code, the anomalous transport coefficients are described by the formula:

$$\chi_e^{an} = \frac{C_e}{\tau_e} \left[0.25 + 0.75 \left(\frac{r}{a} \right)^4 \right] FSB(r)$$

$$\chi_i^{an} = \chi_e^{an}, \quad D_i^{an} = 0.35 \chi_e^{an}$$

where χ_e^{an} , χ_i^{an} are electron and ion anomalous conductivity and D_i^{an} denotes diffusion coefficient the same for all ions. The function FSB has been introduce to model the drop of the transport coefficients near the separatrix corresponding to transport barrier formation. The constant C_e is adjusted in calculation to fulfill the condition

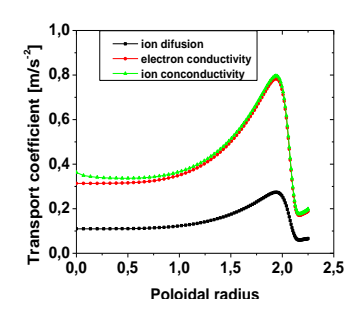
$$\frac{W_E}{P_h} = CP_h^{-0.7} \tag{1}$$

where W_e is the energy contained in plasma, P_h is total heating power and C is the part of the scaling law containing all the other parameters. This model of transport has been compared with the model using the profile of transport coefficient arising from Bohm-gyroBohm model. More precisely we have used the formulae:

$$\chi_{e}^{an} = \frac{C_{e}}{\tau_{e}} \left(\chi_{B} + \chi_{gB} \right) \times FSB^{2}(r), \quad \chi_{i}^{an} = \frac{C_{e}}{\tau_{e}} \left(2\chi_{B} + \chi_{gB} \right) \times FSB^{2}(r)$$

$$\chi_{B} = 2.5 \times 10^{-4} \frac{T_{e}}{B} \frac{a \nabla p_{e}}{p_{e}} q^{2}, \quad \chi_{gB} = 3.5 \times 10^{-2} \frac{T_{e}}{B} \frac{a \nabla T_{e}}{T_{e}} \rho^{*}$$

The same adjustment procedure has been used to determined the constant C_e. The obtained typical profiles of transport take the form shown in the Fig. 11 and Fig. 12. In the Fig. 13 the profiles of the solution are shown.



1,0 — ion diffusion electron conductivity — ion conconductivity —

Fig. 11. Transport coefficients Bohm-gyroBohm model.

Fig. 12. Transport coefficient COREDIV model.

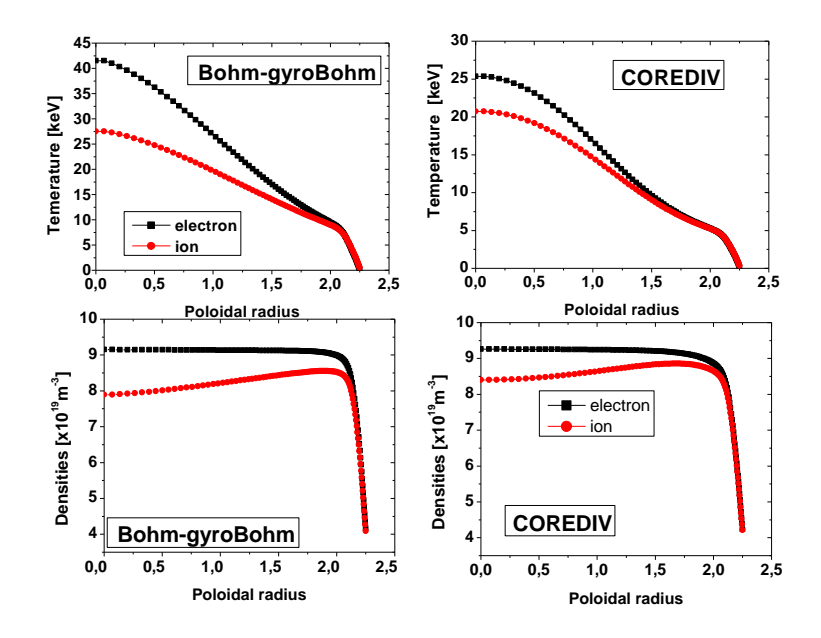


Fig. 12. The profiles of temperatures and densities.

It should be noted that ion conductivity are twice the value for electron conductivity in BGB model. In contrast, in the COREDIV model both conductivities are almost equal. This leads to big difference in electron temperatures obtained using two models.

The global parameters obtained using both model are presented in Table 5 and 6.

Gas puff AR	PαBGB	P _α Corediv	Z _{EFF} BGB	Z _{EFF} Corediv
5.0E17	319MW	328MW	1.59	1.65
1.0E20	319MW	314MW	1.62	1.66
5.0E20	316MW	291MW	1.81	1.76
1.0E21	295MW	280MW	1.85	1.79
2.0E21	284MW	273MW	2.01	1.92

Table 5. Comparision the \mathbf{Z}_{EFF} and \mathbf{P}_{α}

Gas puff	P _{LIN} BGB	P _{LIN} Coredi	P _{SOL} BGB	P _{SOL} Cordiv	τBGB	τ Corediv
AR		v				
5.0E17	86 MW	94MW	151MW	148MW	2.53	2.48
1.0E20	91MW	100MW	144MW	128MW	2.53	2.55
5.0E20	119MW	108MW	101MW	94MW	2.54	2.66
1.0E21	115MW	104MW	87MW	88MW	2.65	2.72
2.0E21	104MW	96MW	86MW	86MW	2.70	2.72

Table 6. Comparison the P_{LIN} P_{SOL} and τ between transport coefficient BgB and COREDIV

For different transport coefficient profiles the global plasma parameters are closed if the confinement scaling law Eq.(1) is fulfilled. The ion conductivity is twice the value for electron conductivity in BGB model. In contrast in COREDIV model the both conductivities are equal. This leads to big difference in electron temperatures obtained using two models.

In order to have agreement with the experimental energy scaling law (Eq.(1)) Bohm-gyro Bohm transport has to be reduced by one order of magnitude in comparison with standard Bohm-gyro Bohm formula (the adjustment of constant C_e). This fact might be explained by the fact that the standard formulae in BGB model were adjusted for existing tokamaks without the fusion energy production.

Conclusions

The reduction of divertor target power load due to radiation of sputtered and externally seeded impurities in fusion reactor was investigated by means of numerical simulations of DEMO discharges with the COREDIV code, which self consistently solves 1D radial transport equations of plasma and impurities in the core region and 2D multifluid transport in the SOL.

Calculations were performed for inductive DEMO and steady-state scenarios with tungsten walls and Ar/Ne seeding. For all considered DEMO scenarios significant fusion power can be achieved. Increase of seeded impurity influx leads to the reduction of fusion power and Q-factor due to plasma dilution. Helium contributes predominantly to Z_{eff} and the total radiation is almost independent on Γ_{puff} , dominated by the core radiation (> 90%): (W+Bremst.+Synch). W radiates predominantly inside separatrix. Power crossing separatrix is close to L-H threshold, in particular for strong seeding. The radiation due to seeding impurity is small and the results are weakly affected by seeded impurity type. The seeding impurity play the important role in sputtering of Tungsten.

For pulsed DEMO concepts, accessible seeding level is limited. There is no steady state solution for stronger puffing. The solution terminates due to helium accumulation, if confirmed by more detailed investigations, might strongly affect DEMO design.

The differences between COREDIV and Process results should be discussed and possibly lead to some modification of assumptions used in Process/COREDIV.

Collaboration

Association EURATOM – IPP Association EURATOM – CEA Association EURATOM – CCFE

Association EURATOM – ENEA

References

- [1] R. Stankiewicz, R. Zagórski Czechoslovak J. of Phys. 52 Suppl.D (2002) 32
- [2] S.I. Braginski, Rev.Plasma Phys.,1 (1965) 205
- [3] R. Kemp, EFDA Rep. WP11-SYS-01-ACT5, DEMO design concepts from PPPT-SYS, 2012
- [4] R. Kemp, EFDA Rep. WP11-SYS-01-ACT5, DEMO design concepts from PPPT-SYS, July 2012.

Verification and validation of ETS. Physics application of the ETS and ITM tools

Roman Stankiewicz (roman.stankiewicz@ipplm.pl)
Irena Ivanova-Stanik
Institute of Plasma Physics and Laser Microfusion

Abstract

The "European Transport Simulator" (ETS) is the new modular package for 1-D discharge evolution developed within the EFDA Integrated Tokamak Modelling (ITM) Task Force. It consists of precompiled physics modules combined into a workflow through standardized input/output data-structures. Ultimately, the ETS will allow for an entire discharge simulation from the start up until the current termination phase, including controllers and sub-systems. The report presents the first physics applications of the ETS for the analysis of JET tokamak discharges

Introduction

A substantial part of present ITM-TF activities is dedicated to the verification and validation of the developed tools and integrated workflows. This is done by means of comparison with analytical results using the method of manufactured solutions, by self-benchmarking (reduction tests)^[19], by benchmarking of modules describing the same kind of process against each-other within the same workflow (cross benchmarking) and by benchmarking of the entire workflow against existing transport codes.

Maintenance, continuing development, verification and validation of the ETS and other core components. Verification and validation of the modules for impurities and neutrals (WP12-ITM-IMP3-ACT1-01/IPPLM/PS).

1. Verification and validation of the impurity module.

Verification of the module for impurity by comparison with SANCO code was performed for parabolic profiles for ion density $n_i(r) = (7.5x(1-x^2) + 0.5)x10^{19}$ [m-3], and for electron temperature $T_e(0) = 1 keV$, $T_e(1) = 100 eV$, $T_e = T_i$. The bulk plasma transport equations were not are not used. ADAS data base is for atomic data. The diffusion coefficient for all impurities ions was assumed equal to 1m2/s and convective velocity was neglected. The simulation was done for JET geometry, for JET shot 71827 and for the different boundary conditions imposed on the impurity density at the separatrix . The boundary density for the tungsten is present in Table 1.

The comparison of the W density between SANCO and ETS for different ionization state is present in Fig.1. The very good agreement between SANCO and IMPURITY/ETS results for densities of impurity and Z_{eff} was observed.

Table 1. The boundary density for tungsten

W	Boundary	W	Boundary	W	Boundary	W	Boundary	W	Boundary
	density for		density for		density for		density for		density for
	Sanco/ET		Sanco/ET		Sanco/ET		Sanco/ET		Sanco/ET
	S		S		S		S		S
$\mathbf{W}^{^{+}}$	2,62. 10-12	\mathbf{W}^{10}	2,23. 10 ¹¹	\mathbf{W}^{19}	1,15. 10 ¹⁶	\mathbf{W}^{28}	7,79. 10 ¹³	\mathbf{W}^{37}	1,06. 10 ¹⁰
		+		+		+		+	
\mathbf{W}^2	1,48. 10 ⁻⁷	\mathbf{W}^{11}	9,58. 10 ¹¹	\mathbf{W}^{20}	2,04. 10 ¹⁵	W ²⁹	5,46. 10 ¹⁴	\mathbf{W}^{38}	1,98. 10 ¹⁰
+		+		+		+		+	
\mathbf{W}^{3}	7,12 .10 ⁻⁴	W ¹²	5,93. 10	\mathbf{W}^{21}	5,9. 10	\mathbf{W}^{30}	8,83. 10 ¹⁴	W ³⁹	1,1. 10
+		+		+		+		+	
\mathbf{W}^4	0,75133	W ¹³	2,82. 10	W ²²	9,08. 10 ¹⁴	\mathbf{W}^{31}	2,75. 10 ¹⁴	W ⁴⁰	3,3. 10 ⁵
+		+		+		+		+	
\mathbf{W}^{5}	216,562	\mathbf{W}^{14}	2,45. 10 ¹³	\mathbf{W}^{23}	1,1. 10 ¹⁵	\mathbf{W}^{32}	9,41. 10 ¹³	\mathbf{W}^{41}	2,4649. 10 ⁴
+		+		+		+		+	
\mathbf{W}^{6}	1,4238. 10	W ¹⁵	9,98. 10 ¹⁴	\mathbf{W}^{24}	1,62. 10 ¹⁴	\mathbf{W}^{33}	2,12. 10 ¹³	W ⁴²	43,53
+		+		+		+		+	
\mathbf{W}^7	4,4022. 10	W ¹⁶	1,26. 10 ¹⁵	\mathbf{W}^{25}	4,97. 10 ¹³	W ³⁴	9,06. 10 ¹²	W ⁴³	1,501
+		+		+		+		+	
\mathbf{W}^{8}	1,64. 109	W ¹⁷	1,22. 10 ¹⁶	W ²⁶	5,76. 10 ¹⁴	W ³⁵	3,75. 10 ¹³	W ⁴⁴	1,319
+		+		+		+		+	
\mathbf{W}^9	2,78. 10 ¹⁰	\mathbf{W}^{18}	6,62. 10 ¹⁶	W ²⁷	4,15. 10	\mathbf{W}^{36}	5,99. 10 ⁹		
+		+		+		+			

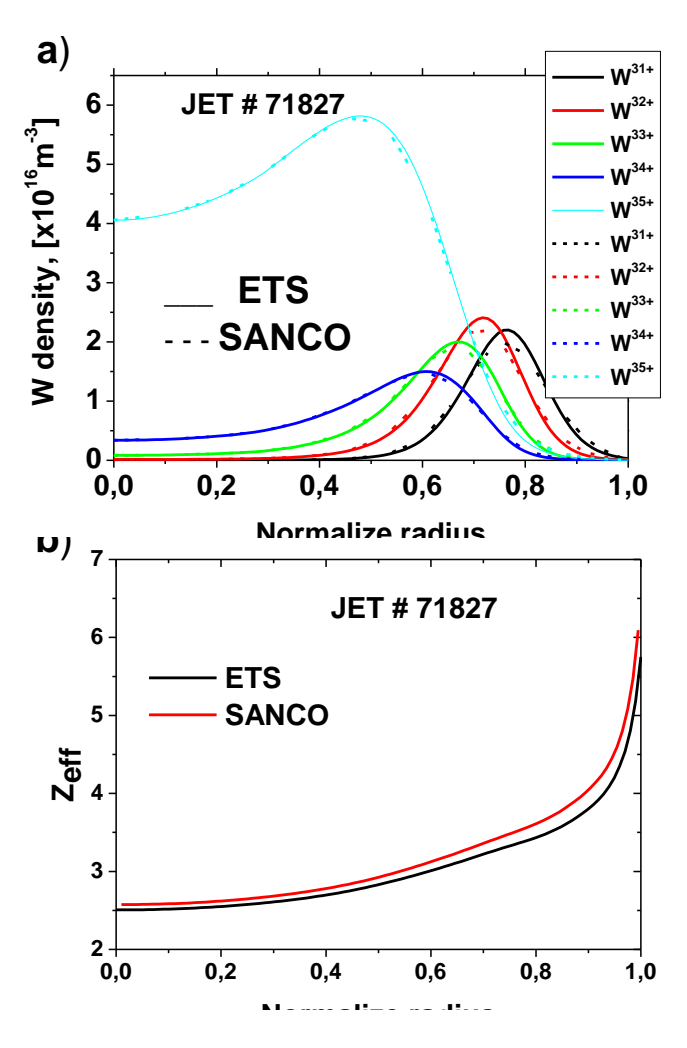


Fig. 1. The tungsten density for 31-35 ionization state (a) and $Z_{\text{eff}}(b)$ for JET # 71827

The radiation power is present at Fig. 2. We have very good agreement between two codes.

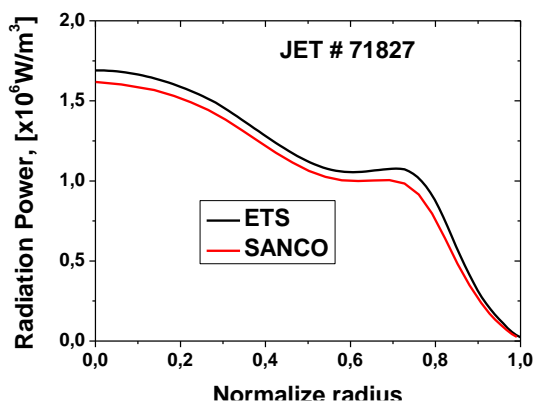


Fig.2. The radiation power from ETS and SANCO.

The next verification test for the IMPURITY/ETS module was done for nickel, for this same condition for as for tungsten. The boundary value for different ionization state for nickel is present in Table 2.

Ni	Boundary density for Sanco/ETS	Ni	Boundary density for Sanco/ETS	Ni	Boundary density for Sanco/ETS	Ni	Boundary density for Sanco/ETS
Ni ⁺	6,357. 10	Ni ⁸⁺	1,622.10	Ni ¹⁵⁺	2,393.10	Ni ²²⁺	2,054.10
Ni ²⁺	2,5083.10	Ni ⁹⁺	5,496.10	Ni ¹⁶⁺	2,358.10 ¹⁶	Ni 23+	1,4764.10
Ni ³⁺	6,379.10	Ni ¹⁰⁺	9,2048.10	Ni ¹⁷⁺	$1,6605.10^{16}$	Ni ²⁴⁺	7,453.10
Ni ⁴⁺	1,263.10	Ni 11+	1,0053.10	Ni 18+	1,0439 10	Ni ²⁵⁺	3,718.10 ¹³
Ni ⁵⁺	2,256.10	Ni 12+	1,2195.10	Ni 19+	1,5365 10 ¹⁵	Ni ²⁶⁺	2,166.10
Ni ⁶⁺	1,202.10	Ni ¹³⁺	6.547.10	Ni ²⁰⁺	8,319.10	Ni ²⁷⁺	1,318.10
Ni ⁷⁺	1,941.10	Ni 14+	1,426.10	Ni ²¹⁺	4,974.10	Ni ²⁸⁺	1,318.10

Table 2. The boundary density for nickel

The calculated Zeff and radiation power is present in Fig. 3.

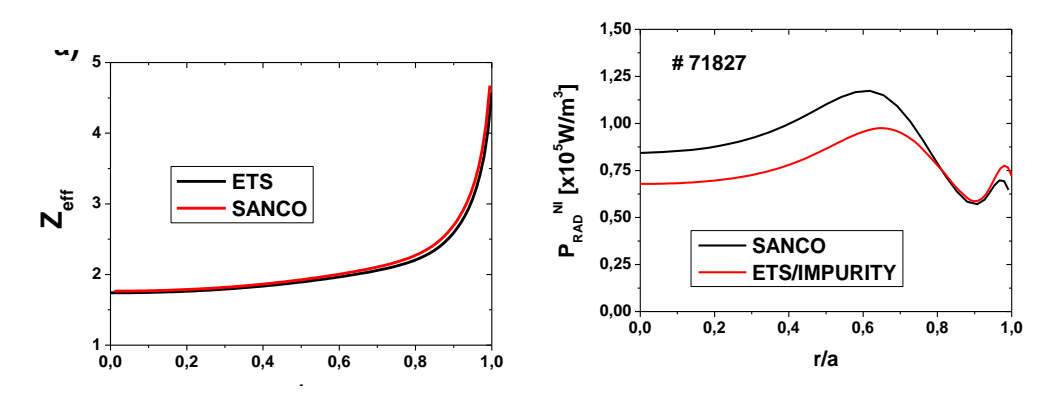


Fig. 3. The simulated the $Z_{eff}(a)$ and radiation power (b) from nickel

We have very good agreement for Zeff, but the big differences are observed for radiativity power. The differences are about 15%. The difference in atomic data (Sanco uses the older version of ADAS data) may account for the disagreement between two codes.

2. Verification and validation of neutrals module.

The module for neutral in ETS solves equations for neutrals in the following form:

$$\frac{\partial}{\partial t} \left(\overrightarrow{V} n_{neuti} \right) + \frac{\partial}{\partial \rho} \left[\overrightarrow{V} \left\langle \left| \nabla \rho \right|^{2} \right\rangle \left(-D_{i} \frac{\partial n_{neut}}{\partial \rho} \right) \right] = \overrightarrow{V} \left(S_{neut, \exp} - S_{neut, imp} . n_{neut} \right)$$

where n_{neut} is density of the neutrals, D_i is diffusion coefficient, S_{neut} is the source term taking into account the ionization, recombination and charge exchange condition. The two groups of neutrals; slow and fast are consider. The generalized form of diffusion equation for quantity used in the ETS is:

$$\frac{a(\rho).Y(\rho)-b(\rho)Y^{t-1}(\rho)}{h}+\frac{1}{c(\rho)}\frac{\partial}{\partial\rho}\left(-d(\rho).\frac{\partial Y(\rho)}{\partial\rho}+e(\rho).Y(\rho)\right)=f(\rho)-g(\rho).Y(\rho)$$

Definition for numerical coefficients for neutrals density equation for slow and fast groups of the neutrals are in Table 3.:

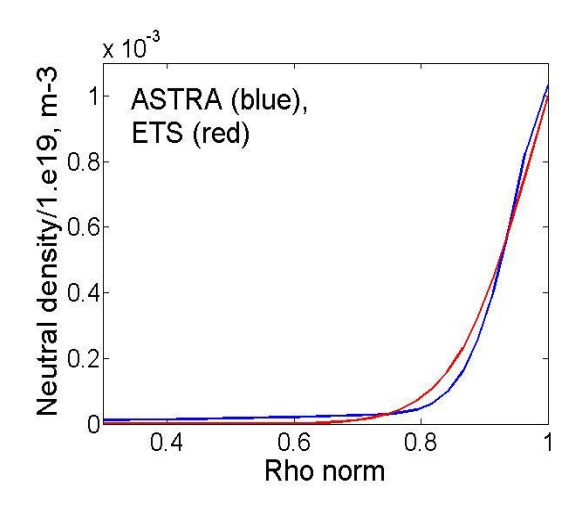
SLOW NEUTRALS	FAST NEUTRALS		
$a(\rho) = V'$	$a(\rho) = V'$		
$b(\rho) = V'^-$	$b(\rho) = V'^-$		
$Y^{t-1}(\rho) = n_{neuts}^-$	$Y^{t-1}(\rho) = n_{neutf}^-$		
$c(\rho) = 1$	$c(\rho) = 1$		
$d(\rho) = V' \langle \left \nabla \rho \right ^2 \rangle D_i$	$d(\rho) = V' \langle \left \nabla \rho \right ^2 \rangle D_i$		
$e(\rho) = 0$	$e(\rho) = 0$		
$f(\rho) = V'S_{neutrs, exp}$	$f(\rho) = V'S_{neutrf, exp} + V'n_i n_{neuts} C_{change} + Vn_e'n_i \beta_{rec}$		
$g(\rho) = V'n_e\alpha + V'n_iC_{charge}$	$g(\rho) = V' n_e \alpha + V' n_i C_{charge}$		
h= au	h= au		

SLOW NEUTRALS	FAST NEUTRALS
$D_{neuts} = \frac{9.56.10^7 T_{neutrs}}{3.m_{neut}(\alpha n_e + C_{chang} n_i)}$	$D_{neuts} = \frac{9.56.10^{7} T_{i}}{3.m_{neut}(\alpha n_{e} + C_{chang} n_{i})}$

The source for the fast neutrals are defined by ion recombination and charge change between slow neutral and ions. We use for diffusion coefficient for neutrals of the form:

Where T_{neuts} is temperature for slow neutrals and T_i is temperature for the ions.

We compared the results for slow neutrals of the ETS/NEUTRALS module with ASTRA results for 1eV neutrals. We use equilibrium for JET#71827 at 52s. The neutral species at the boundary is: N_s =1.10¹⁶m⁻³, E_s =1eV and n_f = 0, E_f =100eV. We simulated only neutrals using fixed background profiles for ion (T_i) and electron (T_e) temperatures, ion(n_i ,) and electron density (n_e) (Fig. 4 and 5).



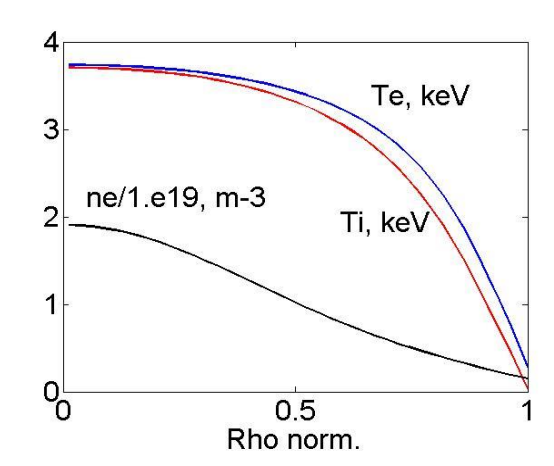
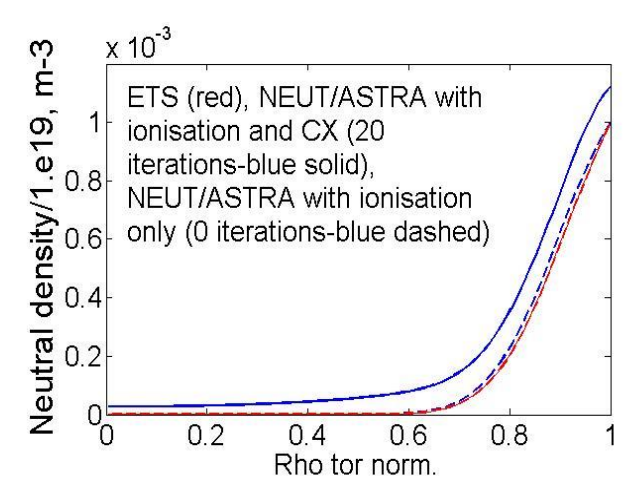


Fig. 4. Input parameters for ETS and ASTRA.

Fig. 5. Simulated result by ETS and ASTRA.

The agreement for slow neutrals with 1eV is very good. The simulation for fast neutrals with 10 eV is presented on the Fig. 6.

We have good agreement.



Support to the validation and physics application of the ETS and ITM tools ($\underline{WP12-ITM-ISM-ACT1-01/IPPLM/PS}$)

ETS was applied to simulate impurity transport for the conditions of JET discharge #81856 (ITER like wall) with two phases of 3.5 MW of auxiliary heating delivered by ICRH and NBI respectively (Fig. 7). In the ICRH heating phase the effective charge, Z_{eff} , and radiative power P^{RAD} are greater than for the NBI phase. Main plasma profiles are less affected by the choice of auxiliary heating.

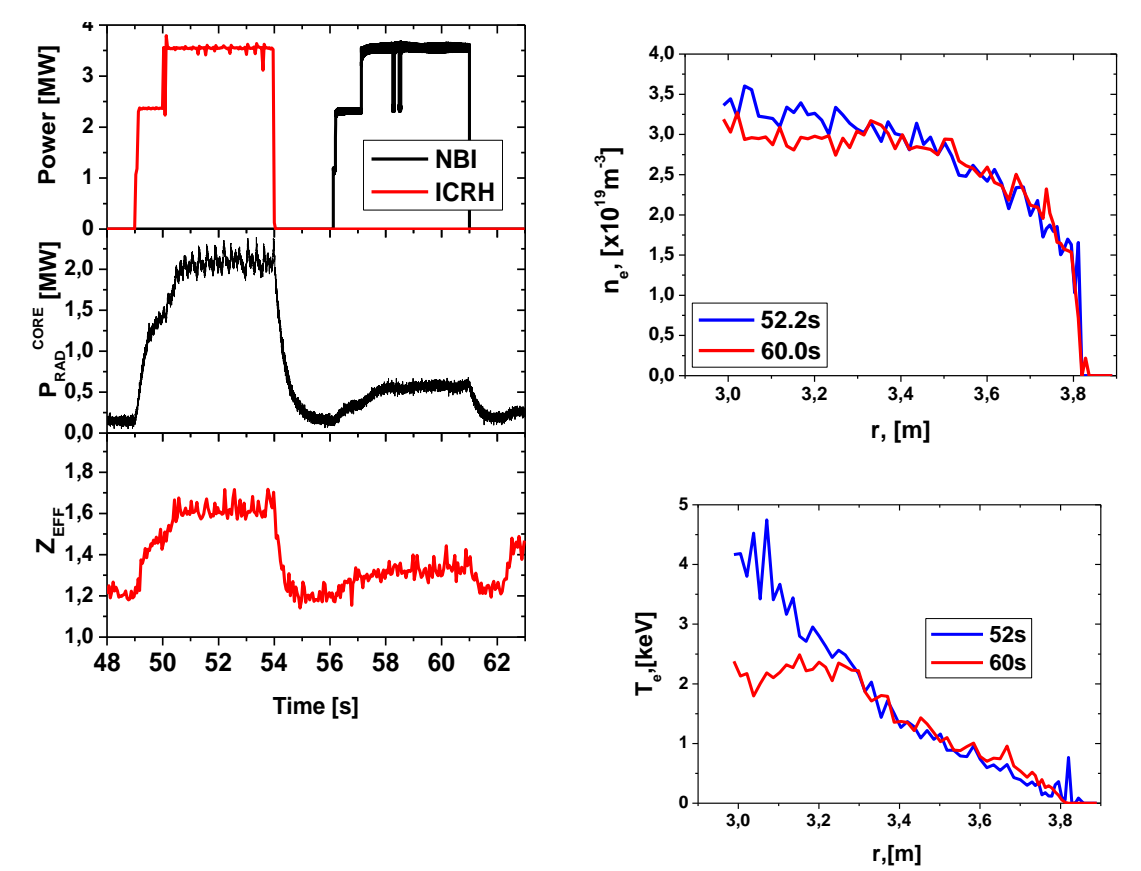


Fig. 7. JET shot #81856. Time traces of auxiliary heating power, radiative losses and line averaged effective charge

Fig. 8. Comparison of experimental profiles of electron density and temperature for ICRH (blue) and NBI (red) heating phases in discharge #81856

Fig. 8 compares experimental profiles of the electron temperature and density in both phases. Some difference in temperature is observed within 0.3 of normalized minor radius, which roughly corresponds to 10% of the volume and can not explain experimentally observed difference in total radiative loss. Thus, the plasma contamination during the ICRH phase can be caused either by an increased source of impurities or by changes in their transport.

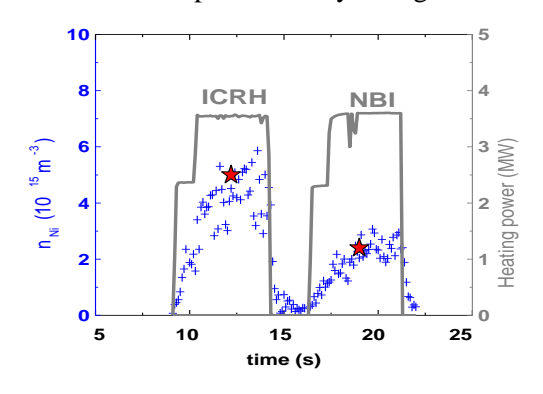


Fig. 9. <u>ETS input</u>: Total density of Ni in the discharge #81856 obtained with SPRED diagnostic (blue crosses) and assumed in ETS simulations (red stars)

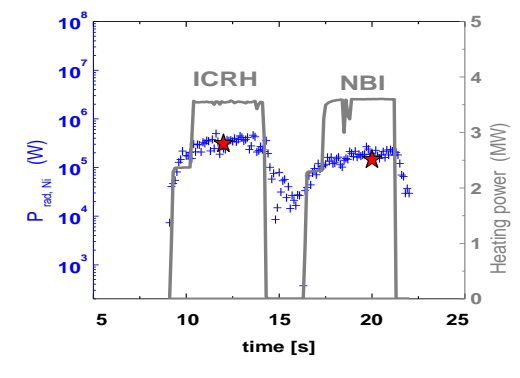


Fig. 10. <u>ETS output</u>: Benchmark of radiation (red stars) from Ni obtained with ETS to the one computed from experimental data using UTC code (blue crosses)

Spectroscopic measurements of Ni impurity along the vessel at midplane were obtained using the SPRED (survey poor resolution extended domain) spectrometer with the routinely used 450 gmm $^{-1}$ holographic grating. This registers the VUV spectra in the wavelength range 100–1100 Å. With the Be/W plasma facing components (PFC) the VUV spectrum was dominated by mid-Z metallic impurities like Ni and also contains intense W features. The determination of Ni impurity densities, based on the combination of absolutely calibrated VUV line transition intensity measurements with the Universal Transport Code (UTC) simulations is described in details in [2]. From the Ni density the radiated power due to Ni and its contribution to the bulk plasma radiated power ($P_{rad,bulk}$) was evaluated based on calculations of the Ni cooling factor presented in $^{[3]}$. The time trace of the total density of Ni obtained with SPRED for the shot #81856 is shown in Fig. 9. The Ni concentration is up to the factor of tree higher for the ICRH phase.

ETS simulations were perfored to reproduce experimental profiles of radiated power density and the value of line-averaged effective charge at selected times (ICRH phase, t₁=12.2 s; and NBI phase, t₂=19 s). Three impurity species (all ionization states of W, Ni and Be) have been simulated until the steady state impurity distribution is obtained. Initial profiles and boundary conditions for individual ionization states of impurity ions are obtained from coronal distribution using experimental n_e and T_e profiles and adjusting total concentration for each impurity. Total Ni concentration was taken from experiment, total W concentration was adjusted to reproduce radiative losses and Be concentration was adjusted to reproduce Z_{eff} . For the NBI phase the total boundary concentrations were selected to $n_W =$ $1.1 \times 10^{15} \text{m}^{-3}$, $n_{Be} = 1.0 \times 10^{17} \text{m}^{-3}$, $n_{Ni} = 2.4 \times 10^{15} \text{m}^{-3}$, and for the ICRH phase these values were increased to $n_W = 4.5 \times 10^{15} \text{m}^{-3}$, $n_{Be} = 2.2 \times 10^{17} \text{m}^{-3}$, $n_{Ni} = 5.0 \times 10^{15} \text{m}^{-3}$. The impurity diffusion coefficients have been computed with the L-mode particle Bohm-gyroBohm transport model [4] and assumed to be equal for all impurity ions. Since the electron temperature and density in the NBI and ICRH phases are similar, computed profiles of transport coefficients are nearly the same. Figure 9 compares the radiated power from Ni obtained in ETS simulation to the one computed directly from experimental data using UTC code.]. The time trace of the total density of Ni obtained with SPRED for the shot #81856 is shown in Fig. 10. The Ni concentration is up to the factor of tree higher for the ICRH phase.

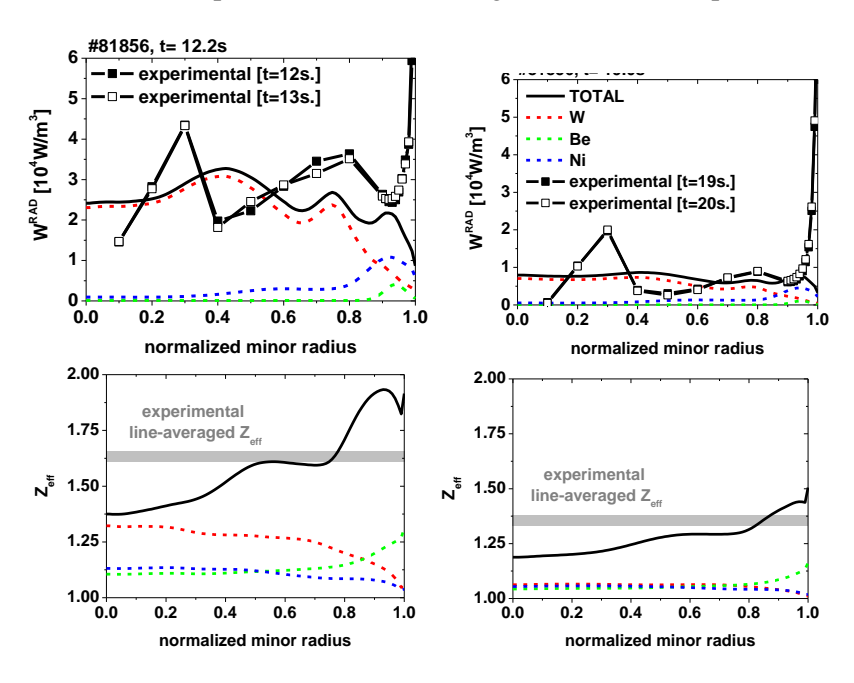


Fig. 11. Comparison of simulated steady state profiles of radiative power density and effective charge with experimentally measured ones: black curves – total profiles, red curves – W contribution to the total; blue curves – Ni contribution to the total; green curves – Be contribution to the total

Figure 11 compares the simulated steady state profiles of radiative power density, W^{RAD} , and effective charge with experimentally measured ones. A reasonable agreement for total radiative power density profile has been obtained for both heating phases. The core radiation is dominated by W during both, ICRH and NBI phases, with the largest contribution from W^{25} - W^{35} ionization states. The core radiation is dominated by Ni ions, whereas Be does not contribute much to the radiative losses. Instead, plasma effective charge is mostly due to light ions, eg. Be and Ni. On the contrary to the radiated power profile, flat or slightly peaked in the centre, the effective charge profile is hollow with the maximum at region closed to separatrix.

Conclusions

Impurity simulations performed for JET discharge 81856 are capable of reproducing the profiles of radiated power and effective charge in a close agreement with the experiment. They show that the increased radiation during the ICRH phase as compared to the NBI phase may be explained by an increased impurity source at the edge. The increase of the radiation is caused mostly by higher concentration of W in the plasma core, particularly by W²⁵-W³⁵ ionization states. Instead, plasma effective charge is mostly due to light ions, eg. Be and Ni. On the contrary to the radiated power profile, flat or slightly peaked in the centre, the effective charge profile is hollow with the maximum at the edge.

Collaboration

Association EURATOM – IPP Association EURATOM – CEA Association EURATOM – CCFE Association EURATOM – ENEA Association EURATOM – IST

Association EURATOM – TEKES

References

- [5] R. Zagorski, et al., Contrrib. Plasma Phys. Vol.52, No.5-6, 379-383(2012)
- [6] Czarnecka et al. Plasma Phys. Control. Fusion 53 (2011).
- [7] D. Post et al At. Data Nucl. Data Tables 20 (1977) 397
- [8] L. Garzotti, Proc. 39th EPS Conference on Plasma Physics 2012, P1.004.

Numerical analyses of impurity seeded plasma discharges in metallic tokamaks (JET, ASDEX-U) with the help of the code COREDIV

Roman Stankiewicz (roman.stankiewicz@ipplm.pl) Irena Ivanova-Stanik, Roman Zagórski Institute of Plasma Physics and Laser Microfusion

Abstract

The report presents the first physics applications of the COREDIV code [1] at JET tokamak discharges with ILW wall and tungsten divertor. The physical model used in the COREDIV code is based on a self-consistent coupling of 1D radial transport in the core to the 2D multifluid description [2] of the scrape-off layer (SOL). In the core, the 1D radial transport equations for bulk ions, for each ionization state of impurity ions and for the electron and ion temperature are solved. For auxiliary heating parabolic-like deposition profile is assumed and the energy losses are determined by bremsstrahlung, ionization and line radiation. In the SOL we use the 2D boundary layer code EPIT which is primarily based on Braginskii-like equations for the background plasma and on rate equations for each ionization state of each impurity species. The sputtering processes of tungsten at target plate by all ions are taken into account. The results are based on the existence of the self-regulating mechanism which couples the tungsten production at the target with the W radiation in the core.

Introduction

The code COREDIV has been used in simulation of JET discharges. The L-mode and H-mode discharges for ILW has been analyzed. The attempts have been made to adjust the parameters external to the code and not precisely determined by the diagnostic in order to obtain agreement between calculated and experimental data. In particular for L-mode the concentration of some impurities like carbon and oxygen are very important. In case of H mode the plasma density at seperatrix turned out to be important for correct determination total radiation in the core.

Simulation of L-mode JET discharges without impurity seeding.

We have selected three well diagnosed discharges heated by ICRF at a power level of $P_{ICRH} = 3$ MW and with central line average density $n_e = 1.65$, 2.3 and 2.8 x 10^{19} m⁻³, respectively.

Numerical simulation of these discharges with COREDIV is a real challenge due to:

- The simplified geometry of the SOL in COREDIV
- Strong coupling edge-core in the relevant temperature range
- The significant level of the Ohmic power (about one third of the total input power)
- Last but not least, uncertainties in the value of some experimental data.

For ILW the main source of Be is, indeed, located on the wall. A detailed description of the JET wall is therefore essential to derive quantitatively the Be fluxes, which, at the end, are responsible for W fluxes from the divertor plates in the relevant temperature range of these pulses (Te_plate < 50 eV). Indeed, W sputtering due to deuterium impact is negligible below $60 \div 70 \text{ eV}$. First, we have taken the experimental divertor Be fluxes as a COREDIV input, and then we have slightly adjusted their values to match the total radiated power.

Considering that for these pulses the Ohmic power ($P_{OH} = 1.3\text{-}1.4 \text{ MW}$) is about one third of the total input power ($P_{tot} \sim 4.4 \text{ MW}$) any change in the computed temperature leads to not negligible changes in P_{tot} , which leads to further changes in T_e profile, T_e _plate, W sputtering and so on. Again, due to the self-consistency of COREDIV, some care should be used when fixing the code parameters to simulate low input-power pulses with the ILW.

Bolometric data is a matter of concern for these ICRF heated pulses since a localised radiation is seen in the plasma core in front of one of the radiofrequency (RF) antennas. This is possibly due to some interaction of the RF electric fields with the beryllium antenna's limiters which may cause significant release of beryllium. Therefore, in order to avoid overestimation of the radiated power, the horizontal channels of the bolometric system pointing at the RF antenna are not taken into account in the process of de-convolution. This, leads to some increase in the level of uncertainty of the experimental data.

In Fig.1a, Fig.1b and Fig.1c the experimental and simulated density and temperature profiles in the plasma core are shown for the three discharges considered. The density profiles have been numerically derived by setting the electron density at the separatrix $n_{es} = 7.2$, 4.5 and 2.9 x 10^{18} m⁻³ for the high, medium and low density discharges, respectively. These values are a bit lower than the two values available from the Li-beam diagnostic (8.5 and 4 x 10^{18} m⁻³ for the high and low density discharge, respectively), but lead to more comparable simulated-experimental profiles in the core as well as to more consistent densities and temperature at the strike point, see below. The experimental-simulated density profiles match generally well, while some discrepancy is seen in the temperature profile. This is a consequence of the linear dependence in COREDIV between particle diffusivity and heat conductivity coefficients, implying reconstructed steep edge temperature profiles when steep edge density profiles have to be numerically reconstructed. However, the influence of the numerical over estimation of the temperature profile has a moderate impact on the radiation patterns since Be radiates mostly in the SOL and W mostly for *Te* in excess of about 2 keV.

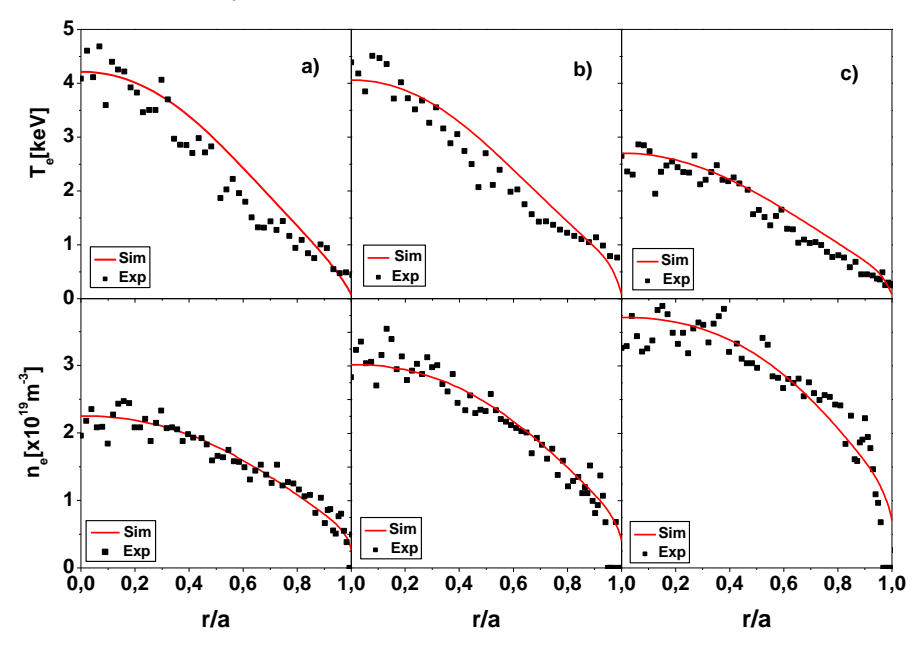
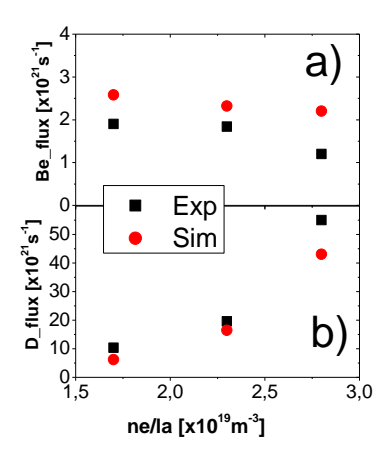


Fig. 1. Electron temperatute (top) and density (bottom) profiles from HRTS diagnostic and COREDIV simulations as function of the normalized minor radius.

From left to right: shot 80896, shot 80889, shot 80893 at t = 59.5 s.

In the of Fig. 2(a) the simulated and experimental D fluxes are shown for the three discharges considered and in the Fig.2(b) the experimental and the COREDIV input Be fluxes. While the simulated-experimental D fluxes match well, the COREDIV input Be fluxes, although within the uncertainties of measurements, are systematically higher than the experimental ones. Setting lower input Be fluxes in COREDIV (please, recall that Be fluxes are an input parameter) to match the experimental ones, would lead to too low power radiated in the plasma core by W, see Fig 2. On the other hand, Be fluxes higher in COREDIV input than in experiment (while the simulated power radiated matches well with the experimental one) are consistent with the presence in the real discharge of no negligible amount of other light impurities as C and O, which normally lead to further release of W from the divertor. In fact, in the present COREDIV simulations, only C is considered and the C flux is set to be at very low level: only about 10 % the of Be flux.



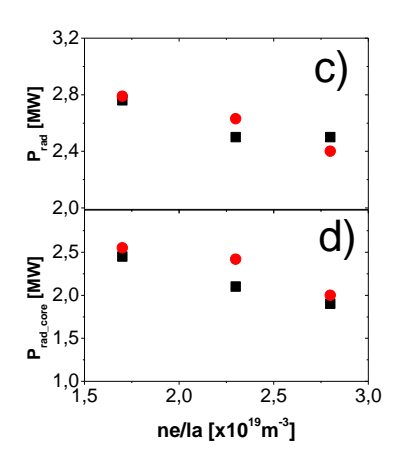
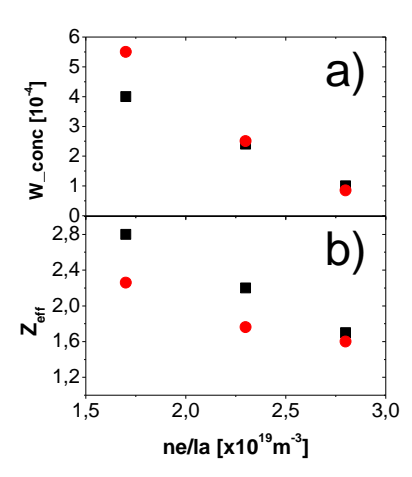


Fig. 2. Experimental and simulated D fluxes (b) and experimental and COREDIV input Be fluxes (a), total radiated power (c) and power radiated inside the separatrix (d) for the three discharges considered, labeled according to their line average density, n_e/l_a



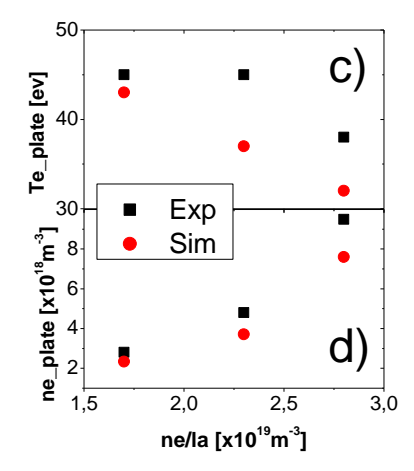


Fig. 3. Experimental and simulated W concentration (a), simulated $Z_{eff}(b)$, electron temperature (c) and density (d) measured at the outer strike point and simulated with COREDIV for the three discharges considered, labeled according to their line average density, n_e/l_a

The substantial agreement of simulated-experimental power radiated is correlated with the very good match between simulated and experimental W concentration in the core, see Fig.3(a). (It is worth noticing that for these discharges the COREDIV calculated W self-sputtering is a significant fraction of the total W sputtering). Indeed, in the relevant range of temperature, only W ions are responsible for the power radiated in the plasma core. It has to be pointed out that the observed decrease of P_{rad} with increasing density is not a general trend of the ILW plasmas, but apply only to these ICRF heated discharges and it is possibly correlated to specific-radiofrequency effects, see below.

Measurements of the absolute W fluxes are not available so far, but the ratios of the intensities (in a.u.) of the WI line at $\lambda = 400.9$ nm for the three pulses considered are quite compatible with the ratios of the COREDIV calculated W fluxes, which are in the range of a few 10^{19} particles/s.

Some problems arise, however, by the comparison of the simulated with the experimental Z_{eff} , see Fig.3(b). Although the experimental Z_{eff} has been derived from the horizontal chord of the bremsstrahlung diagnostic which generally leads in JET to lower Z_{eff} values than that from the vertical one, the simulated Z_{eff} is significantly lower than the experimental one for the two pulses at lower density. In the present contest only higher input fluxes of Be and/or of other light impurities would cause the increase of Z_{eff} in COREDIV, but this would also lead to the increase in the W sputtering and, consequently, in the power radiated. At present, we do not have an explanation for this anomaly, which, however, on a speculative basis and partly in agreement with bolometric observations, would be

consistent with radiofrequency-specific effects. Indeed, the coupling of radiofrequency-power with the plasma is generally rather weak at low electron density and this normally leads to interactions of the electric fields with the antennas' limiters, causing release of Be. This Be flux enters directly the plasma core affecting significantly Z_{eff} , but only marginally the power radiated. On the other hand it should be pointed out that Be transport might be different depending on the position where Be is released from (different screening, for example) while for these three pulses the same impurity transport is assumed in COREDIV.

The experimental electron temperature at the strike point, T_{e} _plate, measured with probes, is higher on the outer divertor than on the inner one, while the electron density, n_{e} _plate, is lower on the outer divertor. In Fig. 3(c-d) the experimental T_{e} _plate and n_{e} _plate measured at the outer divertor are shown together with COREDIV results. It is difficult to compare COREDIV results with experimental measurements on one of the two divertor legs, and this comparison has to be considered more from a qualitative point of view than quantitatively. However, the data in Fig. 3 (c,d) show that we are dealing with similar values and trends, thus contributing to the overall consistency among edge parameters.

Preliminary results on simulation with COREDIV to H-mode discharge (JET#82032

The experimental data for the JET shot 82031-33 is present in Table 1.

Parameters	Jet #82031	Jet #82032	Jet #82033	
Z _{effH}	1.61	1.62	1.59	
$< n_e > [m^{-3}]$	6.21×10^{19}	6.67×10^{19}	6.43×10^{19}	
B [Tesla]	2.18	2.18	2.18	
$I_p[MA]$	1.98	1.98	1.98	
P _{total_NBI} [MW]	10.8	10.8	10.83	
P _{rad} [MW]	4.46	5.65	4.28	
H ₉₈	0.76	0.74	0.80	
T [s]	0.255	0.26	0.28	
Gas puff D ₂ [part/s]	$2.0x10^{22}$	2.14×10^{22}	3.08×10^{22}	
Gas puff N ₂ [part/s]	1.11×10^{22}	1.71×10^{22}	1.67×10^{22}	
Time [s]	56.00	56.00	56.00	

Table 1. Experimental data for the JET shot 82031-33

We have very similar n_e , T_e , Z_{eff} but different radiation power in core. In order to understand the possible reason for this discrepancy we have studied the dependence of the solution on some parameters external to the codes and not precisely determined by the diagnostics.

• Influence of the plasma density on the separatrix

The electron density at the separatrix (n_{es}) is taken in COREDIV as a free parameter to match, when available, with the experimental data. Due to the self-consistency of COREDIV, even a small change in n_{es} may lead to change in the density profile in the core as well as in the SOL, resulting also in changes in n_{e} _plate and, consequently, in T_{e} _plate. This may lead, and does indeed lead for these pulses, to significant change in W sputtering and W concentration and radiation losses in the plasma core. Therefore the choice of n_{es} should be made carefully, step by step, and is time consuming. For these pulses, the edge Thomson scattering diagnostic was not operational, while from the Li-beam diagnostic the edge density profile could be measured only for two (out of three) discharges.

We have presented the results for three different value of the plasma density on the separatrix (see Table 2.). With increase the electron density on the separatrix decrease of the total and core radiation is observed. This is the effect of the low temperature at the plate, small sputtering, and small tungsten concentration. The

value of the plasma density on the separatrix have very weak influence of the Z_{eff.}

Electron den. on seperatix [10 ¹⁹ m ⁻³]	W [10 ⁻⁵]	Z _{eff}	$T_{eplate} \\ [eV]$	$\begin{array}{c} n_{eplate} \\ [10^{20} \text{m}^{\text{-3}}] \end{array}$	P _{total} ^{rad} [MW]	P _{core} rad [MW]	P _{plate} [MW]
$n_{es} = 2.0$	3.51	1.332	4.6	1.47	7.3	5.3	3.1
$n_{es} = 2.5$	2.46	1.370	3.6	2.03	6.6	4.0	3.5
$n_{es} = 3.0$	1.67	1.355	2.7	2.63	6.0	3.3	3.9

• Influence of the radial transport in SOL

The radial transport in SOL is input parameters. By COREDIV simulation total radiation is higher than experimental value. We have been tested the influence of radial transport in SOL. Previous simulation with help of COREDIV for ASDEX, leads to very good correlation with experimental data. We use relation:

$$JET_{rad transp} = K_{dif_rad} x ASDEX_{diff_rad}$$

The results of simulation is present in Fig. 4. Increase of the radial transport leads to decrease of the concentration on tungsten and in consequence decrease of the radiation in core and total radiation.. To determine the radial transport in SOL we need experimental data for tungsten flux.

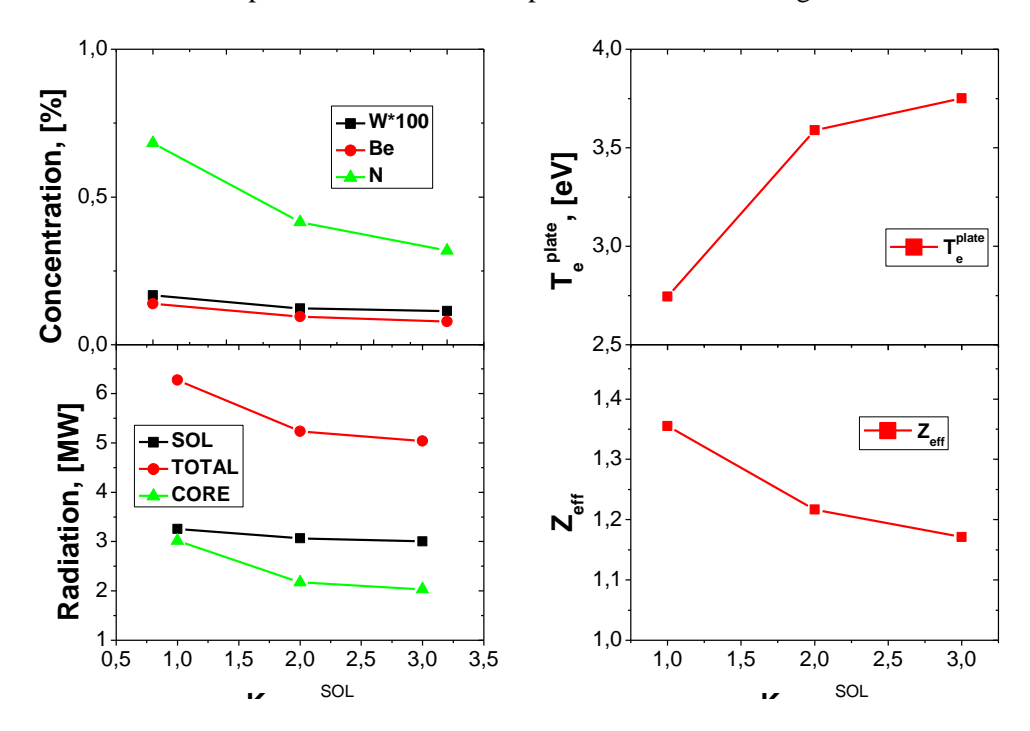


Fig. 4. The tungsten concentration, radiation, the electon temperature to plate, Zeff by COREDIV simulations for different coefficient on the radial transport in SOL

Conclusions

In contrast to previous COREDIV simulations with carbon divertor plates in which the action of the ELMs can be averaged in time without loss of generality, in the case of W plate the role of ELMs might be essential in determining the global W release. That is the reason we started the simulation of JET plasmas with the ILW by choosing pulses at low input power, ELMy free.

On the one hand the simulation of low power ICRF heated JET pulses allow the use of the standard COREDIV version without ELMs, but on the other hand ICRH pulses show a number of radiofrequency-specific effects (as the release of impurities from the antennas' limiters and/or from other surfaces) which can not be simulated with COREDIV due to the slab geometry of the SOL. However, with the relevant exception of Z_{eff} , the overall comparison simulation-experiment is rather satisfactorily, both in the core and in the SOL. To this point it has to be stressed that the Be fluxes on the divertor target are not calculated self-consistently with the plasma parameters, but are given as input in COREDIV, partly according to the experimental Be fluxes and partly to the level of the power radiated.

In conclusion, the results above reported show that, in spite of the limitations related to the slab geometry of the SOL of COREDIV and of those related to the self-consistent simulation of complex and strongly inter-dependent systems like JET plasmas with the ILW, the most relevant critical issues have been solved, leading to the accomplishment of the first step towards the integrated numerical modelling of JET plasmas with the ILW.

Collaboration

Association EURATOM – FZJ Association EURATOM – Belgian State Association EURATOM – CCFE

References

R.Stankiewicz, R. Zagórski, Czechoslovak J.of Phys. 52 Suppl.D (2002) 32 S.I.Braginski, Rev.PlasmaPhys., 1(1965) 205

Novel Divertor Magnetic Configurations: Assessment of physics basis

Roman Zagórski (roman.zagorski@ipplm.pl) Irena Ivanova-Stanik Institute of Plasma Physics and Laser Microfusion

Abstract

This report concerns the activities carried out in the framework of the EFDA Task WP12-PEX-02-T03-01/IPPLM (Novel Divertor Magnetic Configurations: Assessment of physics basis) in the period May 2012-January 2013. Comparison between the snowflake and the conventional divertor has be carried out with the 2D edge code TECXY in the case of the FAST project. The code takes into account all the plasma physics effects occurring in the scrape off layer but simplifies the overall neutral dynamics, considering a simple geometry for the divertor plates and an analytical model for the neutrals recycling. This more manageable and rapid tool allows carrying out a parametric analysis on the code boundary conditions, namely the input flux of particle and energy, that can derive from changing the main plasma and its link with the SOL. Similar simulations will be carried out for DEMO configuration after obtaining proper magnetic configuration for different DEMO divertor concepts.

The results of this task have been already presented at the PSI and SOFT conferences in 2012 and published in the JNM (see [2,3]).

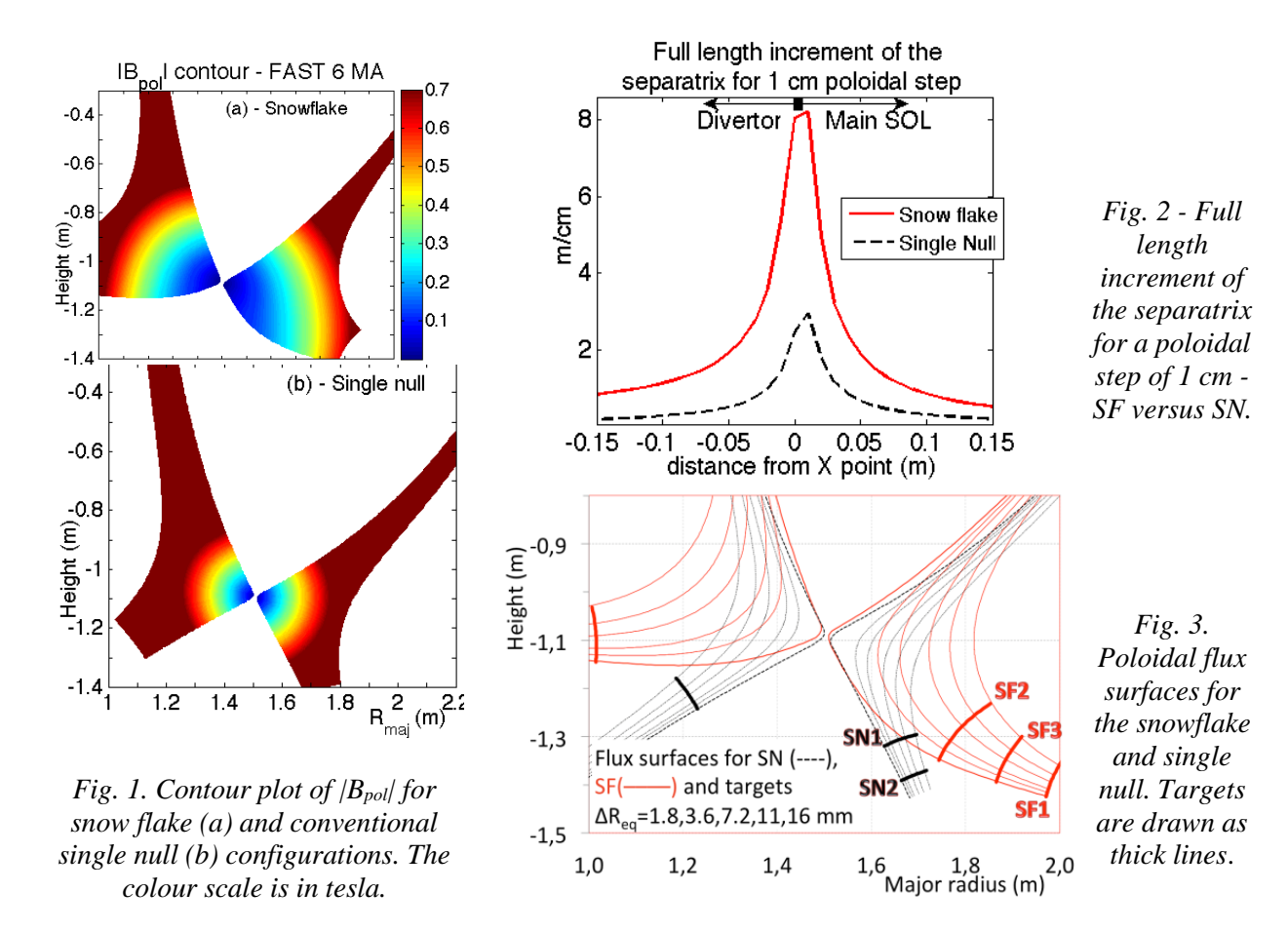
Introduction

A new divertor magnetic configuration, called snow flake (SF), has been recently suggested as a way to mitigate the power load on the divertor targets of a fusion tokamak device [1]. As compared with the conventional single null (SN) the first order null of the poloidal magnetic field B_{pol} in a SN is replaced by a degenerate double pole, i.e. with two nulls merging in one X point. Consequently B_{pol} maintains close to 0 over a wider region around this point where the poloidal flux surfaces external to the separatrix become more distant to each other and the magnetic field lines run more parallel to the toroidal direction. Two main effects directly derive: 1) the larger flux expansion smears the power flux over a wider area; 2) the longer path to be travelled by particle and energy gives them time to diffuse outwards on a longer distance, further spreading the power flow. This second effect can be further enhanced by a slower particle motion just in the region around the X point, due to the lower temperature usually found there. This longer dwell time in a colder region could also increase the volume power losses by radiation and by collisions with neutrals, if their density is non-negligible there.

A programme has been recently launched in the frame of the FAST and DEMO projects to study numerically these new divertor regimes in order to identify their main features and highlight the differences with SN. The first step has been to explore the parameter space with the simple and manageable TECXY 2D edge code for the FAST tokamkak, for which the corresponding divertor configurations have been already designed [2-4]. The TECXY code takes into account all the plasma physics effects occurring but simplifies the overall neutral dynamics with an analytical model for recycling and considers the divertor target plates perpendicular to the flux lines, see [5] for more details. Nevertheless, TECXY is able to identify the most striking differences between the two configurations.

Magnetic topology of the snowflake in FAST

The magnetic topology originating the poloidal spread of the power flow is shown in Fig. 1, as the $|B_{pol}|$ contour map of SF in a) and of SN in b). The much wider poloidal region surrounding the X-point with low $|B_{pol}|$ value is clearly visible for SF. Here the almost toroidal alignment of the field lines makes them longer up to 2.5 times. To detail further this point, in Fig. 2 are compared the increment to the total length of the magnetic line for unit poloidal step (=1 cm) along the separatrix, and in Fig. 3 the shape of the flux surfaces. Here are also shown the various positions of the target plates considered by TECXY as thick full lines.



For SN the reference outer target is that closer to the X point (SN1 in Fig. 3), unless otherwise specified, since its strike point position roughly corresponds to that envisaged by the present version of the SN divertor. The first SF target has been chosen with approximately the same poloidal cross-length of the SN reference and it is found at the farthest position from the X point (SF1 in Fig. 3). The second SF target (SF2) has been located at the closest position to the X point that appears still compatible with the real target positioning at present. The second SN target that has almost the same distance from the X point provides a direct comparison to this case. Finally, a third SF (SF3) target in the middle has also been fixed. For the internal target only one position is considered, due to the much less critical issues that are involved with internal targets.

The change in the peak power load, q_0 , implied by just the different magnetic topology can be quickly evaluated in the simple hypothesis that no dissipation takes place in the flow channel. The total parallel energy flux has to be preserved, i.e. $q_0w|_{SF}=q_0w|_{SN}$, with w=width of the relevant flux tube. Since this latter is proportional to the distance Δ between two adjacent flux surfaces and to the root square of time allowed to diffuse transversally, one has at first approximation $q_0\Delta\sqrt{|L|_c|_{SF}}=q_0\Delta\sqrt{|L|_c|_{SN}}$, being L_c the total magnetic connection length. By averaging over the first SOL layer in touch with the separatrix, the whole reduction factor $f_r=(\Delta\sqrt{|L|_c})_{SF}/(\Delta\sqrt{|L|_c})_{SN}$ is: $f_{r,OT}=1.3$, 2, 3.4 respectively for the farthest (SF1) middle (SF3) and nearest (SF2) outer targets (OT), and $f_{r,TT}\sim2.1$ for the inner target (IT). They

become: $f_{r,OT}\sim1.6$, 2.3, 3.7, and $f_{r,TT}\sim1.8$ correcting also for the different major radii. A magnetic tube 6 mm wide on the outboard equator has been considered, approximately equal to the scale length of the parallel power flow in TECXY, $\lambda_{q\parallel}$. The larger reductions found by TECXY indicate the presence of additional mitigating mechanisms developing with SF, as described below.

The prediction of the code TECXY

The TECXY runs so far carried out try to simulate for both SF and SN configurations the three main FAST scenarios, namely the standard H-mode, the advanced tokamak (AT) scenario and the extreme H-mode [2,3,5], which have respectively volume averaged plasma densities of <n_e>=2, 1.3 and 5×10²⁰ m⁻³. Accordingly, the code boundary conditions that define any specific case have been chosen as follows: i) the outboard mid plane separatrix density has been fixed to the three values, n_{e,s}=0.7, 0.5 and 1.8×10^{20} m⁻³, that should approach closely the most probable ones for the mentioned scenarios; ii) for each of them the input power into the SOL is set to P_{SOL}=20, while 30 MW are considered only for the extreme densities; iii) Recycling coefficient at plates fixed at R_c= 0.9985; iv) perpendicular particle and thermal diffusion coefficient, D_⊥=0.5 m²/s and χ_{\perp} =1 m²/s for both electrons and ions, as previously done [2,3]. These cases refer to the reference targets only, namely SF2 and SN1, see Fig. 3, for 5+5 total runs. Aside them the following other parameters have been considered order to investigate the sensitivity of the results to our assumptions, mainly target position, divertor volume, flux expansion, cross transport and recycling coefficients:

- 1) $\underline{P}_{SOL} = 20 \text{ MW for}$:
 - a) the other OTs (total 6 runs for SF + 3 for SN)
 - b) a fourth density case $n_{e,s}=0.6\times10^{20}$ m⁻³ for all targets (total 3 runs for SF + 2 for SN)
 - c) faster transport: $D_{\perp}=1.0 \text{ m}^2/\text{s}$, $\chi_{\perp}=2.0 \text{ m}^2/\text{s}$ with $n_{e,s}=0.7\times10^{20} \text{ m}^{-3}$ for all targets (total 3 runs for SF + 2 for SN).
- 2) $\underline{P_{SOL}=30 \, MW}$ for two lower recycling coefficients, $R_c=0.997$ and =0.9835, for the three $n_{e,s}$ values, OTs reference only (the closest to X point) (total 6 runs for SF + 6 for SN).

In conclusion a total of 23 different situations for SF and 18 for SN was produced that has allowed us to understand the leading mechanisms and factors for an efficient mitigation.

The chosen P_{SOL} values simulate the medium and rather low core radiation losses that can be achieved with different impurities concentration and/or atomic number. $P_{SOL}=30$ MW can be achieved with the maximum additional power, $P_{add}=40$ MW, for low (25%) losses, while $P_{SOL}=20$ MW corresponds to medium losses (50%) for $P_{add}=40$ MW, and to typical losses (~30%) in the standard H-mode with $P_{add}=30$ MW. Lower values of P_{SOL} that could result for instance from injection of additional impurities, are of not great interest at this stage.

The value of the recycling coefficient corresponds to an input particles flow into the SOL from the core, $\Gamma_\perp = 1.5 \times 10^{21} \, \mathrm{s}^{-1}$ in the standard H-mode SN configuration, that is consistent with the values of previous simulations with the EDGE2D code [7]. Lower values only have been considered for the sensitivity analysis since the high recycling is viewed as the main responsible for the large mitigation of the power load with SF. The corresponding increment of Γ_\perp is quite large, being a factor ~2 and ~10 respectively. The apparently scarce effect of the R_c change on mitigation has given us confidence that we are not in a peculiar and therefore 'unstable' position and that the results are fully reliable within the approximations and limits of the modelling. This however is still not enough for a full quantitative trust to the TECXY results. Indeed the number and density of neutrals that mostly determine the mitigation mechanism, as below discussed, could still be locally altered when a more accurate treatment of neutrals, the actual divertor geometry including the private region, and the local sources and sinks, are taken into account.

Firstly we wanted to compare the overall volume power losses of the SF with SN in order to identify possible general features driving these changes. As expected, the losses are significantly higher for the SF configuration. The much longer time spent by the particles in the regions close to the X point is fundamental, provided the neutral density found there is sufficient to rise significantly the total number of interactions, as inferred from the next figure, Fig. 4, a) and b). In 4a) the global volume losses are plotted versus the average neutral density in the divertor volume, which is the only macroscopic quantity able to give a clear and meaningful trend to the data points, by grouping them tightly along two well distinct and separate curves, one for all SF cases and one for all SN cases. The divertor volumes farther

than the section pertinent to "nearest" OT induce then negligible effects. The leading role is played by the volume close to the X point, where a travelling particle spends the largest part of its time. Trend lines different for each OT would instead result by considering the total neutrals number, disregarding the divertor volume. Consistently, SF has larger losses due to the longer connection lengths. The b) part of Fig. 4 quantifies this indication: a unique well-defined curve is obtained by multiplying the neutral density for the average dwell time $<\tau_{dw}>$ spent within the divertor volumes. For an easier comparison with the previous figure this is done by scaling only the SF abscissas by the ratio $f_n = <\tau_{dw,SF}>/<\tau_{dw,SN}>$, which is evaluated as follows. The connection lengths are evaluated by averaging over a magnetic tube wide $2\lambda_{q\parallel}$ on the outboard equator ($\lambda_{q\parallel}\sim6$ mm for SF) that gives $<L_{c,SF}>/<L_{c,SN}>=2.48$. The ratio between the mean particle speeds is assumed to be well represented by that between the ion sound velocities $c_s = T^{1/2}/m_i$ ($T = T_e + T_i$, electron+ion temperature, and $m_i = 100$ mass) at the target plates, averaged over both OT an IT. The almost constancy of this ratio, whose meaning is still to be investigated makes almost constantthe f_n value, $f_n \sim 4.7$.

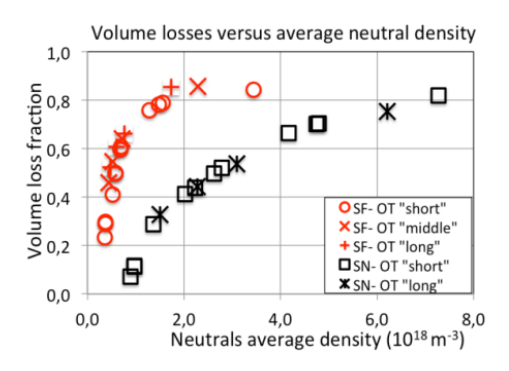
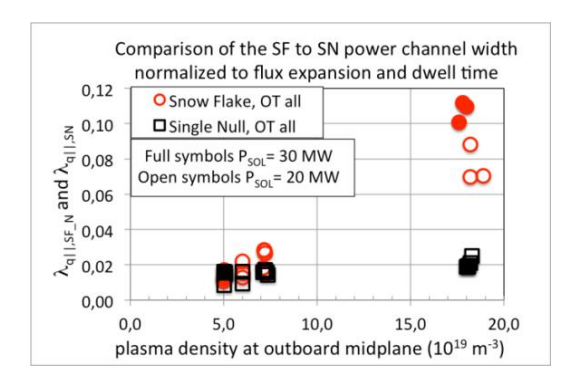


Fig. 4a. Comparison of the global volume losses (radiation+charge exchange) for SF and SN as a function of the average neutrals density

Fig. 4b. Same data as previous plot but with the SF abscissa corrected for the dwell time ratio with SN

We also observe that the volume losses apparently saturate to 80% for neutral densities that appear manageable also from the point of view of the plasma performances. The peak values at the plate are about 10 times the average values for SF reported in Fig. 4a, i.e. somewhat less than $n_{e,s}$. They are consistent with a previous study of the conventional SN with the code EDGE2D [7] for the not-too-close configurations of the divertor.

The mechanism responsible for the large global effects is even more pronounced on the peak power load close to the strike point since just there the difference between the SF an SN magnetic topology has its maximum. Moreover a lower power flux generally further favours the attainment of detachment. Prior to illustrate the most striking change in the target profiles of the main SOL plasma quantities we want to show the magnitude of this added peculiar reduction for all the cases considered. The plot of Fig. 5 shows the variation of $\lambda_{q\parallel}$ on the OTs versus $n_{e,s}$ for all configurations of both SN and SF. For this latter, $\lambda_{q\parallel}$ has been reduced by a factor that accounts for the geometrical effect, i.e. by the flux expansion ratio and by $\sqrt{\tau}_{dw}$ since the distance diffusively covered in a time τ is $\infty \sqrt{\tau}$. The SF additional mitigating effects are small for $n_{e,s}$ =0.5×10²⁰ m⁻³ (AT scenario), begin to increase for $n_{e,s}$ =0.7×10²⁰ m⁻³ (standard H mode scenario), and become very large for the extreme H-mode with $n_{e,s}$ =1.8×10²⁰ m⁻³. Further these extra effect appear to be exalted at higher power.



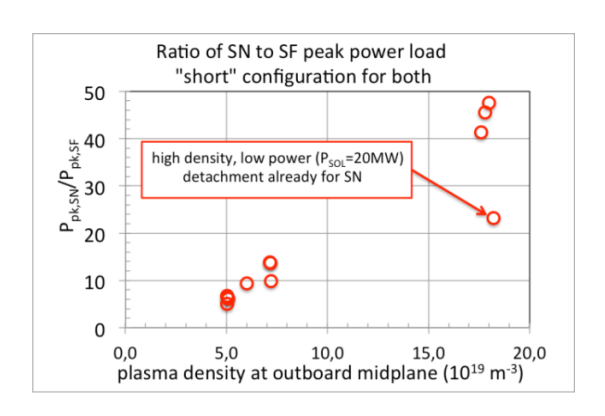


Fig. 5 Comparison between SF and SN $\lambda_{q||}$ values (power flow). For SF the values are corrected for the ratio to SN of flux expansion and of $\sqrt{\tau}$ dw to get rid of topological effects

Fig. 6. Mitigation factor for the peak heat load with SF as a function of the density at separatrix.

We stress however that the mitigation of the peak load is anyway very significant also for these low densities, and larger than the above-mentioned geometrical effects. Even with no flux expansion, as for the SF "far" OT (line SF1 in Fig. 3) the mitigation is always >2 against the expected factor 1.6.

We further note that the correction applied to the SF channel width for comparison with SN is not purely topological, since the temperature decreases with the length of the lines for the reasons mentioned above, depressing in turn the average velocity along them.

`To give an idea of the mitigation potentiality of the SF, Fig. 6 presents the ratio of the SF to SN calculated peak loads on the OTs "near" configurations (SF2 and SN1 in Fig. 3) that should best approximate the target actual positions, as said. The minimum mitigation is for the low density and high power case and is a factor \sim 5 for of which \sim 1.2 is due to the volume losses, 2.5 to the expansion and the residual \sim 1.7 partly to the longer time available for diffusing perpendicularly and partly to the additional processes above discussed. The highest value is for the high density and power cases and is \sim 45, averaging over the three different R_c cases. The contribution of the volume losses and of the flux expansion are still \sim 1.4 and 2.5 respectively for all, while that of the dwell time is \sim 2.4. The residual factor \sim 5 is due to the efficient redistribution of the power in the high density regime, particularly in the flux tubes adjacent to the separatrix as discussed above, that favours detachment from the target. The mitigation factor drops again for the point indicated with an arrow simply because the reference SN case is already a semi-detached case due to the lower power (P_{SOL} = 20 MW)

The next figures compare the actual plasma parameters in front of the targets when changing configuration. For the sake of brevity only the "near" option of OTs is considered for both SF and SN. The profiles for the power load, the plasma density and the electron temperature are plotted for the standard H-mode, the AT scenario and the extreme H-Mode respectively in Fig. 7, Fig. 8 and Fig. 9. For a better visual comparison, the power load on the SN target has been divided in all figures by a factor indicated in the relevant plot. The main features emerging from these pictures, in addition to what has been already commented, is the very strong kick-off towards detachment by SF that is achieved except than in the AT case. The very high density that is anyway built up, $n_{e,OT,SF}>3\times10^{20}~m^{-3}$, drops T_e from 100 to ~25 eV. Consequently, this would heavily depress the sputtering rate of impurities from the target surface that strongly depends on the sheath voltage drop, ~3 T_e . Complete detachment seems attainable in the very high density extreme H-mode where the plate temperatures are in the range of 2 eV and density in the range of $6\times10^{20}~m^{-3}$.

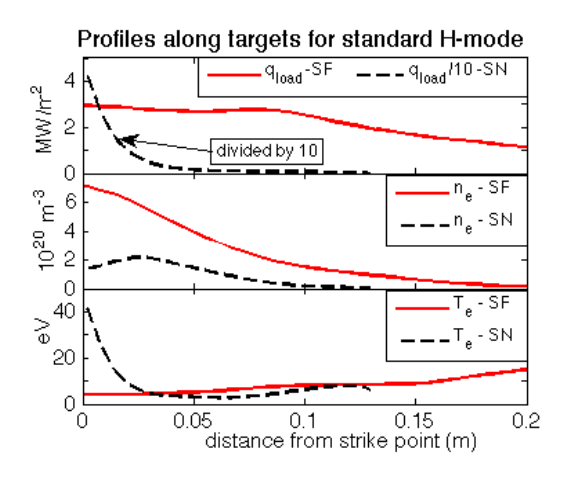


Fig. 7. Comparison SF/SN of the profiles along the target of (from top to bottom): power load, density, electron temperature. Standard H mode case with $P_{SOL}=20$ MW and $n_{es}=0.7\times10^{20}$ m⁻³

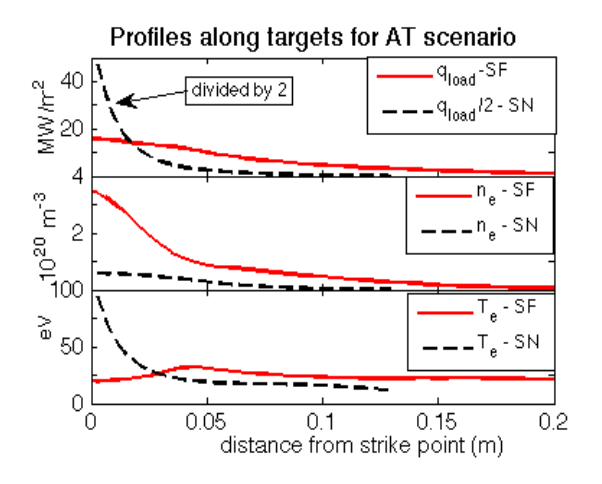


Fig. 8. Comparison SF/SN of the profiles along the target of (from top to bottom): power load, density, electron temperature. AT scenario case with $P_{SOL}=30$ MW and $n_{es}=0.5\times10^{20}$ m⁻³

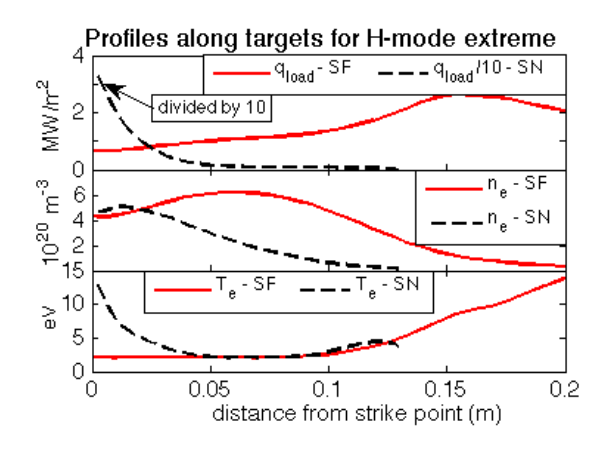


Fig. 9. Comparison SF/SN of the profiles along the target of (from top to bottom): power load, density, electron temperature. Extreme H mode case with $P_{SOL}=30$ MW and $n_{es}=1.8\times10^{20}$ m⁻³

Table I Summary of the power balance for the reference cases of Fig. 7, Fig. 8, Fig. 9

	Standard H mode	
	P _{SOL} =20 MW	
MW	SF	SN
$\mathbf{P}_{\mathrm{rad}}$	4.6	4.1
Pother	7.5	6.3
P _{load,tot}	7.9	9.6
P _{load,OT}	5.6	7.1
P _{load,IT}	2.3	2.5

AT scenario		
$P_{SOL}=30 \text{ MW}$		
SF	SN	
2.4	1.8	
6.4	1.7	
21.2	26.5	
14.5	16.3	
6.7	10.2	

Extreme H mode		
$P_{SOL}=30 \text{ MW}$		
SF	SN	
8.5	8.3	
15.2	12.8	
6.3	8.9	
4.6	6.5	
1.7	2.4	

The dramatic drop of the power load opens the possibility for FAST to operate even in the AT scenario without the help of radiating impurities, otherwise necessary to limit the release of tungsten from the plates and an excessive plasma pollution. Scenarios at even less density and higher current seem now no more ruled out. From the engineering point of view all the new loads reported in the figures appear manageable, by keeping them below the safety limits of 15 MW/m²with a moderate tilting of the plates. A strike angle of 20° , which implies no operational concern, will drop the peak by a factor ~ 0.34 , i.e. down to 12 MW/m² for the AT case.

Finally, to complement the information from the previous three figures the power balance terms are synoptically summarized in the table below. The radiated power, the other non-radiative losses, the total power load and the load on OT and IT are given for each case.

Conclusions

The status that may be found in the new snow flake configuration of the FAST divertor has been explored with the simple and flexible 2D edge code TECXY[2,3].

The parameter space explored with the present study has allowed to identifying the reason for strong extra mitigation that adds on top of the topological effects. It is mostly the longer time spent by the travelling particles in the divertor because of the much longer magnetic lines (see Fig. 1). The consequent cooling and hence slowing down also triggers two positive feedbacks: more dwell time is available for interacting with the neutral and for diffusing radially. This mechanism not only produces volume effects, but it is the fundament also of the very large peak load reduction, since it is particularly effective for the magnetic lines adjacent to the separatrix. Nevertheless a minimum neutrals density is required to raise these effects to a significant level. Indeed, for the low density AT scenario, the mitigation is dictated mostly by the topological effects.

With the present investigation we have also checked that one of the most weak point of our modelling, namely the neutral dynamics, is not so critical. Indeed varying the recycling coefficient to the point of changing the particle flux entering the SOL by a factor 10, no significant variation is obtained in the results. Nevertheless, these very appealing properties of the SF configuration need to be confirmed by a more accurate modelling of the plasma edge that takes into account the actual divertor geometry, including the very important private region, the divertor pumping and the real neutral dynamics.

Finally, it should be stressed that the results obtained for FAST configuration, if confirmed also in the case of DEMO project as well as by more detailed simulations, would indicate a possible way to the solution of the power exhaust problem in fusion reactor.

Collaboration

Association EURATOM – ENEA

References

- [1] M. V. Umansky et al., Nucl. Fus. V. 49 (2009) 075005
- [2] V. Pericoli Ridolfini, et al., Comparative study of a conventional and snowflake divertor for the FAST (Fusion Advanced Studies Torus) tokamak, http://dx.doi.org/10.1016/j.jnucmat.2013.01.083
- [3] V. PericoliRidolfini, et al., Preliminary 2D code simulation of the snowflake divertor configuration in the FAST tokamak, presented at the SOFT Conference, Sept. 2012.
- [4] G. Calabrò, F. Crisanti et al. Nucl. Fusion V. 49 (May 2009) 055002
- [5] R. Zagórski, H. Gerhauser, PhysicaScripta, V. 70, Part 2/3, (2004) 173
- [6] G. Maddaluno et al. Nucl. Fus. V. 49No 9 (Sept. 2009) 095011
- [7] V. Pericoli Ridolfini et al., Fus. Eng. Des. V. 86, N. 9-11, p. 1757-1761, (Oct. 2011).

2.2 Fusion Plasma diagnostics

Development of soft X-ray triple GEM gas detector for energy resolved soft X-ray plasma diagnostics

Maryna Chernyshova (maryna.chernyshova@ipplm.pl), Tomasz Czarski, Katarzyna Jakubowska, Jacek Rzadkiewicz, Lesław Karpiński, Marek Scholz Institute of Plasma Physics and Laser Microfusion

Wojciech Dominik, Henryk Czyrkowski, Ryszard Dąbrowsi, Krzysztof Kierzkowski, Zbigniew Salapa, Warsaw University, Faculty of Physics, Institute of Experimental Physics,

Krzysztof Poźniak, Grzegorz Kasprowicz, Wojciech Zabolotny Warsaw University of Technology, Institute of Electronic Systems

Abstract

For the purpose of detecting X-ray lines intensities from the energy resolved diagnostics two detectors based on Triple GEM amplification followed by the strip readout electrode were developed in order to measure intensities of soft X-ray radiation diffracted by the crystal suitable for the specific soft X-ray energy range. High-resolution X-ray diagnostics for MCF devices is expected to monitor the plasma radiation emitted by W46+ and Ni26+ ions at 7.8 keV and 2.4 keV photon energies, respectively.

Introduction

The impurity concentrations, ion temperature, and the toroidal rotation velocity are key parameters which must be monitored at a high level of accuracy for all the operating phases (H, He, D or D/T) and for different operating scenarios (Ohmic, L-mode, H-mode, hybrid, steady state) of the ITER-oriented JET research programme. The high-resolution x-ray spectroscopy is a powerful tool for diagnosing the properties of tokamak plasmas. The Bragg crystal x-ray spectroscopy has become well-established technique for diagnosing these plasma parameters by high-resolution measurements of the impurity X-ray lines. The characteristic X-ray radiation emitted by highly ionized metal impurities provides accurate information on the crucial plasma parameters such as impurity concentrations, ion temperature, and the toroidal rotation velocity [1,2].

The high-resolution X-ray crystal spectrometer (KX1) at JET is expected to measure the impurity concentrations, ion temperature, and the toroidal rotation velocity from Doppler width and shift of Ni $^{26+}$ at 1.59 Å. In order to measure the tungsten impurity concentration in the new ITER-like JET configuration, the upgraded spectrometer will operate with an additional (1011) quartz crystal (2d=6.68 Å) mounted in June 2009 and sharing the same 266 mm diameter beamline. The quartz crystal will be used for the reflection of low energy X-ray photons emitted by W^{46+} at 2.4 keV. Thus two detectors were developed directing at Ni and W impurities high time resolution line measurements at 7.8 and 2.4 keV, respectively.

The characteristic X-ray lines are measured by new generation energy-resolved micropattern gas detectors with 1-D position reconstruction capability. The analogue signal processing electronics should allow on-line energy measurement and position reconstruction with the precision better than the strip pitch. The monitoring system should allow the measurements of the plasma evolution in time-slices corresponding to 10 ms exposures.

Design and construction

In the prototype phase of the project it was demonstrated that the T-GEM detection structure sketched in Fig. 1 provides a good charge gain for the Ar+CO₂ gas mixture [3].

The common experience confirms that the rate capability of single GEM detector operated at charge gain ~ 100 exceeds 3×10^6 Hz/mm² when exposed to x-ray flux with Ar+CO₂ gas filling [4].

When the GEM foils are configured in the cascade operation mode one should achieve similar performance at the moderate charge load on the single GEM electrode. The T-GEM structure allows one to reach total gas gain exceeding 10⁴ with extremely low discharge probability due to the charge gain sharing between the GEMs.

The structure of the detectors was designed and tested by two prototypes with 128 channels and is as follows:

- Cascade of 3 GEM foils (Fig. 1) with the gap of 2 mm in each detector, respectively,
- Conversion gap of 15 mm,
- Readout plane with 0.8 mm strip pitch (256 strips in each detector),
- Induction gap width of 2.5 mm,
- Mylar window 12 μm (for higher energy) and 5 μm (for lower energy) with thin Aluminum layer (\sim 0.2 μm) on the inner surface.
- Final detector windows are supported by two slabs of 0.8 mm in diameter installed on the outer side of the window.

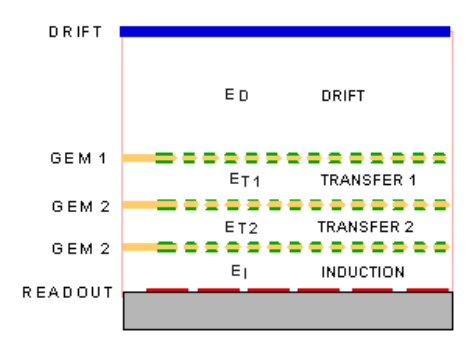


Fig. 1. Schematic view of the T-GEM detector. E_D , E_{T1} , E_{T2} and E_I are the drift, transfer and induction fields, respectively.

In this geometry the strip detector can be kept on ground potential. The high voltage of negative polarity increases gradually reaching maximal value of the potential applied to the window. Thus, seven individual channels of high voltage can be employed. Whole detector is supplied from dedicated T-GEM Power Supply Unit (PSU) which is customised version of commercially available product . The PSU is remotely and locally managed combination of 7 channel High Voltage units (HVU) and 2 channel Low Voltage units (LVU). The HVU consists of 7 independently controlled power stages, each delivering up to $1.5~\rm kV$ at $500~\mu A$. The voltage and current of each stage is independently regulated and limited.

Gas mixture and window materials were optimised for two energy regions in order to find the best gas mixture and the detector window material to obtain the maximum efficiency for detection of 2.4 keV (W⁴⁶⁺) and 7.8 keV (Ni²⁶⁺) photons. Conversion efficiency for detector filled with Ne+CO₂, Ar+CO₂ and Ar+CF₄ for 1.5 cm gas layer with different ratio of used gas with included 6 μ m and 12 μ m of Mylar metallized by 0.2 μ m of Aluminium foil was calculated (see Fig. 2 for Ar/CO₂(30%)). On the one hand, the gas mixture and detector window used in GEM detector should provide the highest absorption and the highest transmission, respectively, and be beneficial from economic point of view on the other one. The window of the detector serves also as a cathode in GEM detector system and for this purpose material of window is a metallized foil. This is especially important in case of 2.4 keV photons, because they could be easily absorbed even in thin metallized foils.

The best conversion efficiency of 2.4 keV photons is ensured by Ar+CF₄ mixture on the level of 59%, 57% and 52% for the detector window of 6 μm My and gas mixtures in ratio 60:40, 70:30, 80:20, respectively. The best conversion efficiency (23-24% in ratio 80:20) of 7.8 keV x-ray photons is ensured by Ar+CF₄ and Ar+CO₂ mixtures. In case of the detector window consisted of Mylar 12 μm and 0.2 μm of Al the conversion efficiency is lower for about 8%-10% than for the window with 6 μm of Mylar and 0.2 μm of Al. Costs of the Ar+CF₄ gas mixtures are almost two times less than for the Ne+CO₂ and Ne+CF₄ ones.

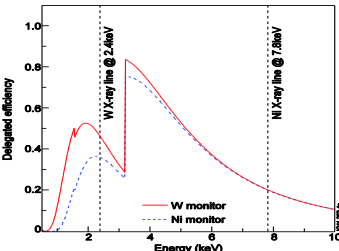


Fig. 2. Calculated photon detection efficiencies for Ar/CO_2 (30%) working gas mixture as a function of photon energy for Ni and W monitor X-ray detectors with 12 μ m and 5 μ m Mylar windows, respectively.

Finally, as a working gas the $ArCO_2$ (70:30) gas mixture with 15 mm thickness of gas-mixture layer has been chosen. In this case detection efficiency above 40% for 2.4 keV and around 20% for 7.8 keV may be achieved.

Detector processing electronics features

Number of channels 256 for each detector

Sampling rate 100..130MHz

ADC resolution 8 bits
ADC ENOB 7..9 bits
AFE SNR Min. 40dB

Total digital throughput and data processing capability Min. 330Gbit/s (Total data rate at the ADC outputs)

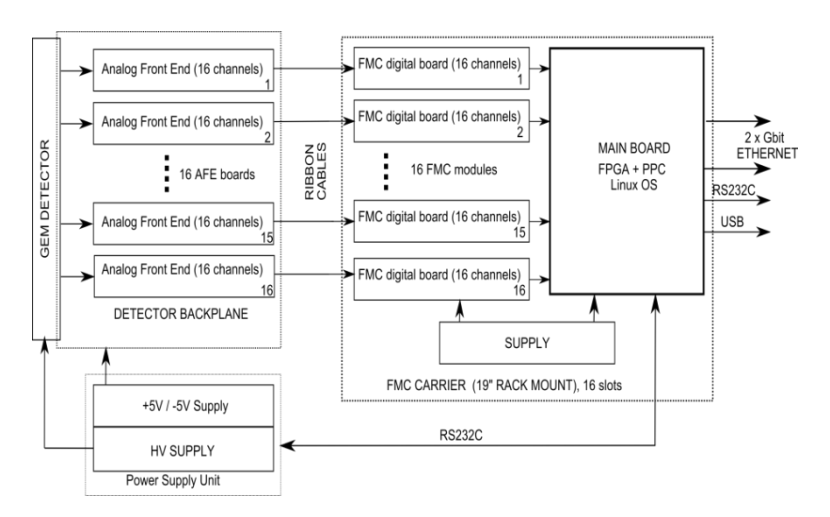
Histogram resolution 512 bins Histogram refresh rate: Min. 50/s Expected detector signal 100fC

HV supply 7 channels, Max. 1.5kV each @500uA

LV supply +/- 5V, 12A

Control interface Dual Gigabit Ethernet, dual RS232C, USB

Calibration Yes, 256 channels, test charge adjustable 0-150 fC



Each detector electronics (see block diagram) consists of several blocks:

- Detector strip board with backplane,
- Amplifiers and differential cable drivers board 16 Analogue Front End boards (AFE),
- 16 FMC digital boards,
- The carrier module with 16 FMC slots,
- High and low voltage power supply unit (PSU).

The detector strip board is equipped with 256 strips connected to dense Panasonic connectors which transfer signals to the backplane board. This board distributes detector signals to the AFE boards. It is attached to 3U Europa type crate where 16 AFE modules are plugged. The crate will be mounted to the detector assembly. Each AFE module consists of 16 charge amplifiers followed by differential cable drivers equipped with MD5 connector. The cable driver converts single-ended signal from amplifier to differential one. The charge amplifiers convert current signals from the strips and also shape the output voltage signal. High speed low noise current feedback amplifier will be used. Analogue bandwidth is limited to 15 MHz. Each channel is equipped with dedicated calibration and protection circuit. The calibration circuit allows injecting the known charge selectively to any combination of the AFE board inputs. Selection of calibrated channel and charge value is managed by the FMC board. This enables the rapid diagnostics and calibration of the whole detector. Expected charge from the detector is 100 fC (it corresponds to 10 ns current pulse with 10 uA amplitude). Maximum output signal from AFE is 1V.

Experimental results

The preliminary test of the experimental setup was performed using laboratory X-ray sources for the energy measurement capability and position reconstruction precision (in one dimension) based on the center of gravity approach. The signals from the AFE board of 16-channels were converted from analog to digital signal, transferred to FPGA module and later on to PC. The data reconstruction and data analysis allowed the cluster charge measurement of individual events, the measurement of a cluster size in terms of the number of activated strips, the measurement of the shape of the cluster distribution and, thus, the position reconstruction in one dimension.

The detected current signal had two components: the induced current due to change of the anode induced charge and the discharge current due to withdraw of the space charge. Total change of induced charge was zero; consequently only the space charge as a resultant value was determined by the current signal integration. Total triggered time period was 400 ns (40 signal samples). The part of the space charge collected by a strip was estimated as the integral of the anode current within internal time window of 200 ns (20 samples). Figure 3 presents comparison of the current signals of 8-bit resolution (1000 events) of the data acquired with oscilloscope (left) and the current signals of 10-bit resolution (1000 events) acquired with FPGA module (right).

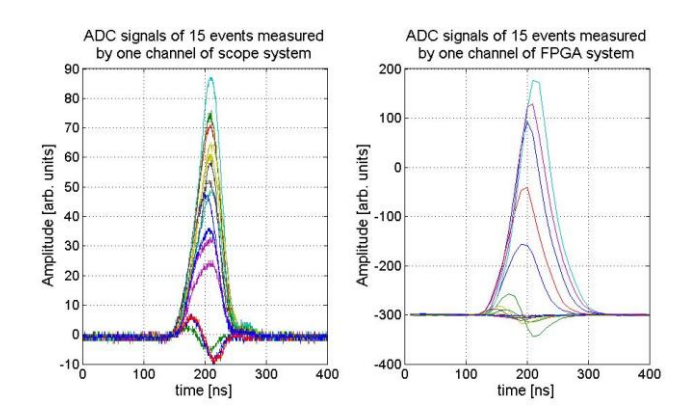


Fig. 3. The anode current signals for 1000 events measured with ⁵⁵Fe radiation source on one of the oscilloscope channel's (left) and the anode current signals for 1000 events measured on one channel using FPGA module (presented data correspond to two different measurements)

The time resolution of the measurements performed with oscilloscope and FPGA module was more than one order of magnitude different. It was equal to 2.5 GHz and 0.1 GHz for oscilloscope and FPGA module respectively. As one can observe in Fig. 3 the anode current signal acquired with setup employed with FPGA module preserves shape that was achieved in measurements with oscilloscope.

The T-GEM detectors with $20x10~cm^2$ detection area were tested to study energy and space resolution and the Ar/CO_2 (30%) gain as a function of applied voltages (GEMs, induction, drift and transfer voltages). Tests were mainly performed by means of the 55 Fe x-ray source and 2-10 kV X-ray generator (1-100 uA). Taking into account the importance of position precision determination for the Bragg crystal x-ray spectroscopy some tests were conducted for the purpose of its estimation.

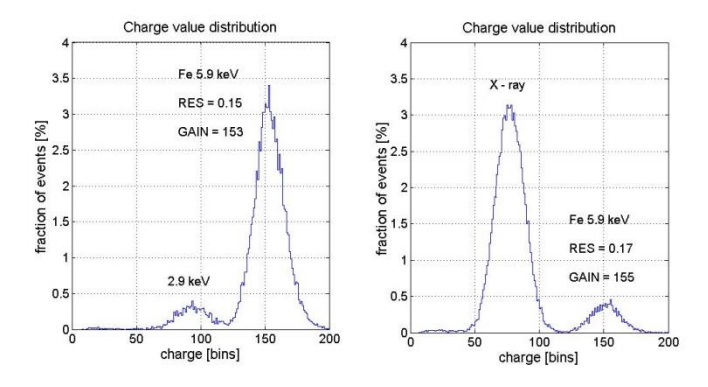


Fig. 4. Charge distribution for ⁵⁵Fe source (left) and combined measurement with X-ray and ⁵⁵Fe source. The total GEM voltage for prototype detector II ($U_I = 1200V$, $U_D = 1200V$, $U_{TI,T2} = 700V$). GEM voltage $HV_{G2} - HV_{G1} = HV_{G3} - HV_{G2} = 20V$

At this aim the X-ray generator was used at the working voltage of 2.5 kV and filament current of 100 uA. The measurements with X-ray generator and 55 Fe source has proven that the detector is operating stably for different photon fluxes along the strips (Fig. 4). The charge position distribution was analyzed with X-ray tube source (2.5 kV, 100 uA) (Fig. 5). The surface of the prototype detector window was irradiated by X-ray bundle through the collimator (diameter of 0.7 mm). Two measurements with the same voltage settings were performed (HV(1:7) = [1200, 360, 700, 360, 700, 360, 1000] [V]) for two different collimator positions. The measurement has proven the local detector position resolution to be better than 1 strip (0.8 mm). It insures that the detectors should match the operational requirements of the high-resolution X-ray diagnostics.

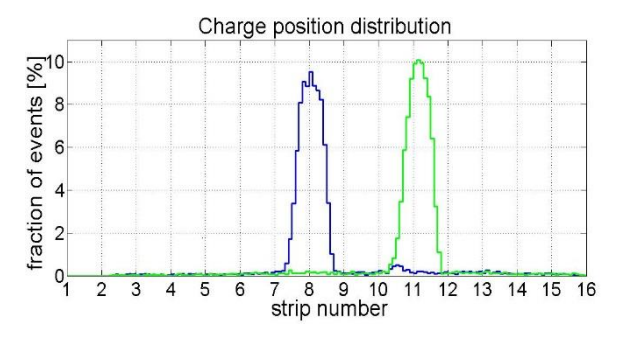


Fig. 5. Charge position distribution for selected source position. Source: X-ray tube (2.5 kV, 100 uA) with the 0.7 mm diameter collimator

For the purpose of accurate estimating X-ray lines intensities from the energy resolved diagnostics the calibration procedure was developed and preliminary tests were performed in order to minimize the inaccuracy related to the detector chamber and electronics irregularity.

Conclusions

For both, low- at 2.4 keV (W⁴⁶⁺) and high-energy at 7.8 keV photon energy (Ni²⁶⁺) diagnostic channels two T-GEM detectors with 206x92 mm² detection area and 256 strip channels each have been constructed. Two materials are considered as final detector windows, namely Mylar 5 μ m + Al 0.2 μ m for W monitoring and Mylar 12 μ m + Al 0.2 μ m for Ni monitoring. The final detector windows is supported by two slabs (0.8 mm in diameter) installed on the outer side of the window. The expected detector efficiencies are 45% at 2.4 keV (W monitoring channel) and 20% at 7.8 keV (Ni monitoring channel), respectively.

In the framework of this task it was possible to obtain the high space resolution (better than 0.8 mm) and time resolution ($\Delta t \sim 10$ ms) for both detectors. That is significantly better than the performances of previous KX1 detector ($\Delta x \sim 1.27$ mm, $\Delta t \geq 20$ ms). The same is true in the case of energy resolution. It was shown that both detectors can safely work with a reasonably good energy resolution, $\Delta E \sim 20\%$.

Collaboration

Association EURATOM - CCFE, Culham, United Kingdom

References

- 1. K-D Zastrow, H W Morsi, M Danielsson, M G von Hellermann, E Källne, R König, W Mandl and H P Summers, J Appl Phys 70, 6732 (1991)
- 2. K. W. Hill et al., Rev. Sci. Instrum. 79, 10E320 (2008)
- 3. J. Rzadkiewicz et al. Report on the construction and performances of prototype GEM Detectors for KX1 JET Diagnostics (2010).
- 4. S. Bachmann et al, Nucl. Instr. and Meth. A 443, 464 (1999).

Development of the soft X-ray spectrometry systems for the stellarator W7-X

Monika Kubkowska (monika.kubkowska@pplm.pl), Agata Czarnecka, Waldemar Figacz, Sławomir Jabłoński, Jacek Kaczmarczyk, Leszek Ryć Institute of Plasma Physics and Laser Microfusion

Abstract

Two spectroscopic systems: pulse height analysis (PHA) and multi-foil system are currently under design for Wendelstein 7-X stellarator for long pulse operation. The proposed PHA diagnostic is intended to provide the spectral energy distribution with energy resolution not worse than 180 eV along a central line of sight. The system consisting of 3 single Silicon Drift Detectors (SDDs) operated with different filters will be installed on the horizontal port AEK50 on W7-X. Each detector will record an X-ray spectrum in three different energy ranges from 400 eV to 20 keV. In MFS system the recorded spectrum is determined by measurement of the total X-ray emission (as the effect from interaction of many quanta) in different ranges of energy, which are determined by the type and thickness of the filters and the thickness of the detectors (usually the ranges overlap). The MFS method is characterised by lower, in comparison with the PHA system, spectral resolution.

Introduction

The investigation of the X-ray emission from fusion plasmas has become a standard diagnostic tool used on many different fusion experiments [1]. The measurements of X-ray intensities by using Si-detectors, which are sensitive to the total radiation above a threshold energy determined by thin absorber foils in front of the diodes, yield an excellent spatial and temporal resolution. The determination of the X-ray energy spectrum using PHA systems requires sufficiently long acquisition times resulting in a poor temporal resolution. This method is particularly suited for long pulse operation envisaged for W7–X.

The combination of spectral data obtained along a single line of sight with broadband radial X-ray intensity profiles will provide a haracterization of the impurity radiation in the plasma core. The measurements yield impurity survey spectra in the X-ray region above $0.5~\rm keV$ allowing to identify the line radiation from all relevant impurities (with exception of elements lighter than nitrogen) and to determine their concentration in the hot plasma core. The slope of the hydrogen and low-Z continuum radiation is used to determine the central electron temperature. The intensity of the continuum radiation along with additional spectroscopic data allows to assess $Z_{\rm eff}$ values in the plasma center.

Computer simulations of soft X-ray emission from a tokamak plasma played important role in designing of each diagnostic systems. As a tool for checking the performance of the PHA and MFS spectrometry systems and optimizing filters and detectors, a special numerical code, named RayX [2] has been developed. Number of simulations have been done and the results allowed to determined the position of the diagnostics components.

The super conducting stellarator W7-X will run pulse of up to 30 min duration with full heating power. Electron Cyclotron Resonance Heating (ECRH) is the main heating method for steady-state operation of the Wendelstein 7-X stellarator in the reactor relevant plasma parameters. In the first phase of working a heating power of 8-10 MW is planed to use. A wide spectrum of requirements has to be considered during the design and realization of the new X-ray diagnostics. Since ECRH auxiliary heating will be applied in W7-X, different heating scenarios, characterised by widely different electron temperature and density profiles have been taken into account [3].

Described two spectroscopic systems, PHA and MFS are being designed by IPPLM for measurement of soft X-ray emission from W7-X stellarator, which construction has been finished in 2012. It is worth noting that at the beginning of 2012 a new Agreement on Cooperation between IPPLM and IPP Greifswald has been signed for 3 next years.

Pulse height analysis soft X-ray diagnostics for stellarator W7-X

In designing the PHA system on W7-X a special developed numerical code, RayX, was used. The code allowed to investigate the influence of a geometrical configuration of the diagnostic systems on the spectra intensity and shape. It also calculates the radiation from plasmas with the use of different pinhole sizes, types of detectors, filters' material and thickness, as well as to simulate emission from different discharges characterised by widely varied electron temperature and density profiles. The results of simulations allowed to develop optimal diagnostic systems and design a mechanical setup.

In 2012 manufacture drawings of PHA system have been prepared and presented IPP in Greifswald (Fig.1). After their acceptation a public tender for manufacture of PHA vacuum chamber has been announced. Time of deliver the system is estimated to April 2013.

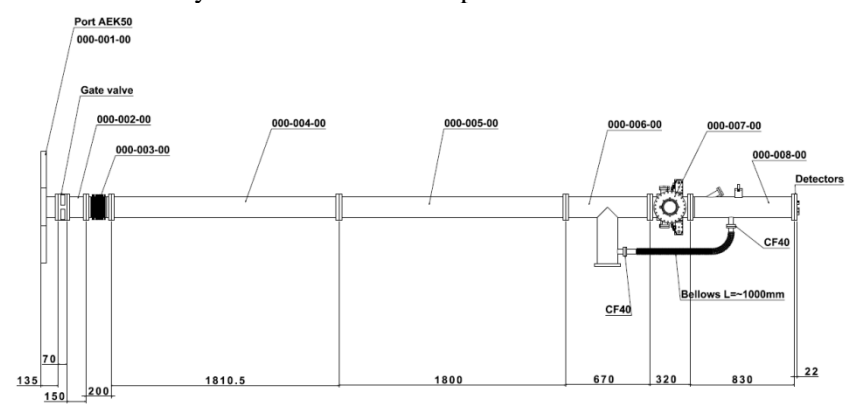


Fig. 1. General design of the PHA diagnostics system for W7-X.

In 2012 a prototype of the filter control mechanism by a wobble stick using a small (fast) and large pneumatic cylinder as actuator has been made and tested in the laboratory, what is presented in Fig.2. The wobble stick movement is limited by a brace. This design handles the sucking force of the vacuum on the mechanical feedthrough (bellow). The positioning is a two-stage: fast adjustable is made by a small cylinder and a big cylinder is used for the large (about 20 mm) movement. The precision of the adjustment will be 0.1 mm. A two way pressure valve (supply and exhaust of pressurized air; 3 to 5 bar) controls with a feedback reading the 3 filter positions. There will be also a possibility to have a closed position and if necessary cut the radiation.

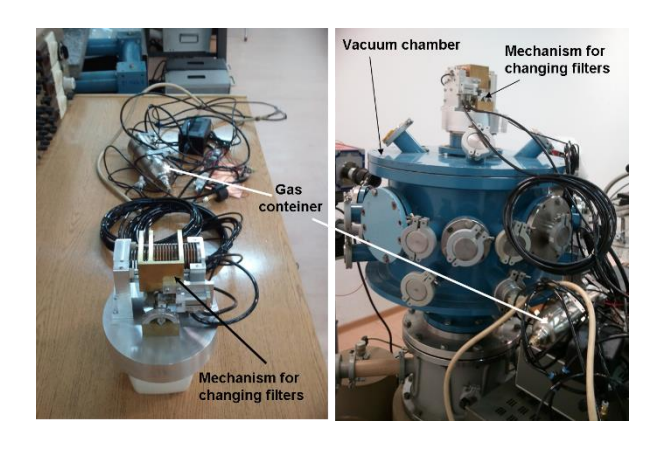


Fig.2. Details of the mechanism of changing filters (left) and testing stand with the vacuum chamber (right).

The PHA system on W7-X will consists of three energy channels. First one will be equipped with SD3 detector containing polymer window and aluminum light protection, to cover energy range between 250eV and 20keV. Second and third channel will be equipped with standard SDD detector with $8\mu m$ of Be window, however in the third channel additional thick filter will be used. This will allow to record spectra in the range of 1-20 keV and 7-20keV, respectively. All detectors will be accompanied by an individual control of pinholes size and 3 additional replaceable filters for adjusting the energy range in each system, as it was described above.

In 2012 a DN160CF detectors flange with multipin connectors has been delivered (Fig.3 left). Also a detector cooling system for PHA system has been manufactured at IPPLM workshop, what is presented in fig.3 (right).

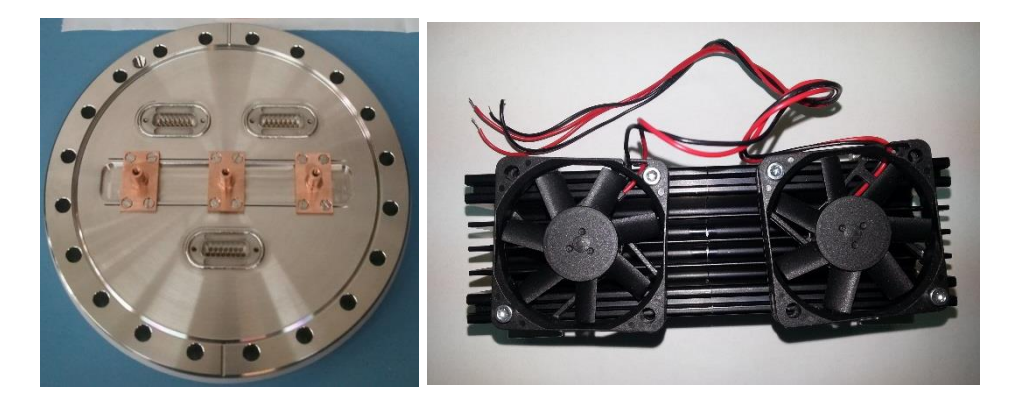


Fig. 3. Detectors flange for PHA system on W7-X with special multipin connectors (left) with .

Multi-foil soft X-ray spectroscopy diagnostics for stellarator W7-X

The MFS system will be realized on port AEN20 as a part of the so-called flexible SX camera system on the AEM10-AEN10-AEO10 port combination.

This diagnostic will consist of 8 detector arrays (for 5 detectors each) using different 8 filterfoils, current amplifiers and a memorising system. Tests carried out on different types of detectors showed that FLM type detectors with 380 μ m of active layer, surface 5×5 mm and 10 pF of capacity, produced by Institute of Electron Technology in Warsaw are the best candidates for this diagnostic. The detectors have been mounted on Alumina with a capacitor and resistor integrated to the board (SMD-technology). As the ranges of sensitivity of individual energy channels overlap, a special mathematical procedure is applied to recover the real X-ray spectrum from the experimental data. An analysis of a dark current and noise of the considered detectors showed that acceptable level of the detected current should be higher than 100 nA.

In 2012 detector arrays have been bought (fig.4) and tested. Manufacture drawings of MFS system have been prepared and sent to IPP Greifswald for general design review.



Fig. 4. Detector arrays for MFS diagnostics system for W7-X.

In the system there will be 8 energy channels with 8 different beryllium filters. It was established that at the entrance to the vacuum chamber there will be $10~\mu m$ of beryllium foil and additionally every array will have their own filter:

- 1 st channel without filter
- 2 nd channel 25 μm of beryllium foil
- 3 rd channel 50 μm of beryllium foil
- 4 th channel 100 μm of beryllium foil
- 5 th channel 250 μm of beryllium foil
- 6 th channel 500 μm of beryllium foil
- 7 th channel $1000 \mu m = 1 mm$ of beryllium foil
- 8 th channel 2000 μ m = 2 mm of beryllium foil.

In MFS system, a similar as in PHA diagnostic, mechanism with wobble stick will be used but in this case it will play a role of shutter.

Conclusions

At the beginning of 2012 a new Agreement on Cooperation between IPPLM and IPP Greifswald has been signed for 3 next years. In 2012 manufacture drawings with all details of proposed PHA and MFS systems have been performed and present IPP Greifswald. The DN160CF detectors flange with multipin connectors for PHA system has been delivered. The detector cooling system for PHA diagnostics has been manufactured at IPPLM workshop.

In 2012 detector arrays have been bought and tested for MFS diagnostics. Also thicknesses of beryllium filters have been chosen.

For both diagnostics a mechanism with wobble stick, which will be used for changing filters or/and cut the radiation from plasma, has been made and tested in laboratory.

Collaboration

Association EURATOM - Max-Planck Institute of Plasma Physics, Greifswald

References

- [1] A. Weller, S. Mohr, C. Junghans, Review of Scientific Instruments 75, 3962 (2004)
- [2] S. Jablonski, A. Czarnecka, W. Figacz, M. Kubkowska, J. Kaczmarczyk, L. Ryc, J. Wolowski, 1-D plasma X-ray radiation code as a first step for developing the fusion diagnostics, 39th EPS Conference 2012, Stockholm, Sweden
- [3] A. Czarnecka, M. Kubkowska, W. Figacz, S. Jabłonski, J. Kaczmarczyk, J. Wołowski, C. Biedermann, R. Burhenn, R.König, A. Weller, Concept of pulse height analysis system (PHA) for Wendelstein 7-X, P1.052, 38th EPS Conference on Plasma Physics (2011)

The activation measurements in support of the JET neutron calibration

Barbara Bieńkowska (barbara.bienkowska@ipplm.pl) Sławomir Jednoróg, Rafał Prokopowicz, Marek Scholz, Adam Szydłowski Institute of Plasma Physics and Laser Microfusion

Abstract

The neutron diagnostics need to be calibrated very carefully, because they are essential to proper determine fusion power and estimate dose rate from activated structure materials. The response function of each neutron detector depends on neutron energy spectrum and, accordingly, on source characteristics and surroundings. In case of JET calibration, the spontaneously-fissile californium point source will be used instead of D-shape deuterium plasma source of 2.5 MeV neutrons. Therefore, neutron transport calculations should strongly support the calibration.

Introduction

In order to provide proper neutron spectrum the numerical simulations will be performed by means of the MCNP transport code based on the Monte Carlo method. It takes into account the real position, shape, energy spectrum of the calibration source and influences of its environment, such as the IERT-like wall, MASCOT Robot, etc. The neutron activation method will be used as a benchmark for the numerical calculations. The reactions induced in purpose-prepared activation samples by the neutrons from calibration source enable to compare the results of the simulations with the results obtained using the activation system (KN2). The MCNP model verified during such procedure can be used to calibrate other neutron diagnostics.

The measurements

The multi-element activation measurements shall be performed during JET neutron calibration. The measurements carried out by means of the KN2 system utilizing purpose-prepared activation samples enable to record a number of nuclear reactions induced by the neutrons coming from calibration source. Modern, pre-calibrated HPGe gamma-spectrometer belongs to IPPLM will be used to estimate activity of irradiated samples. The experimental data collected in such way allow determination of the activation coefficients for recorded reactions. The coefficients will be then compared with the MCNP results.

Verification of the MCNP model of inner torus and calibration of the KN2 enable to improve the accuracy of neutron calculations and measurements at JET. Calibrated KN2 system can be used to cross-calibrate the KN1 (neutron monitor), KN3 (neutron camera), etc.

The neutronics issues relevant to licensing process need to be performed on ITER as well. The experiences acquired during JET neutron calibration will be useful for preparing such action on ITER.

Testing irradiations

As a preparation to the measurements on JET the suitable activation materials have been selected and the activation samples have been prepared. The following materials have been selected for neutron activation measurements during JET calibration by means of Cf-252 source: In, Au, Mn, W, Ta, Sc, Fe, Ni, Al. The activation samples consisting of above mentioned materials have been prepared in KN2-standard size (18 mm in diameter).

Test irradiation on PF-1000 with neutron fluence similar to calibration conditions has been performed. According to the MCNP simulations the neutron energy spectrum from PF-1000 device have been shaped by moderating medium in order to be similar to the spectrum expected in JET 3U irradiation end during calibration by means of Cf-252 source. Prepared activation samples have been irradiated in the neutron field shaped in such way. The neutron fluence, however, was about 6 times less than expected during 3-hours irradiation by means of Cf-252 source in 30 cm-distance from 3U irradiation end. Besides of that, most of expected radiative capture reactions have been recorded, unlike threshold reactions, which mostly have not been recorded due to difference in fast neutrons spectrum coming from d-d reaction and Cf-252 source.

General perspectives

The activation measurements during JET neutron calibration shall be carried-out during calibration of the JET neutron diagnostics in March/April 2013. The experimental results shall be elaborated and compared with the calculation data.

Collaboration

Association EURATOM – CCFE, Culham, United Kingdom Association EURATOM – JSI, Lubljana, Slovenia Association EURATOM – LEI, Vilnius, Lithuania

2.3 Emerging technologies

Detection of the chemical components of ITER relevant (co)deposits by the LIBS investigation of calibrated samples in various irradiation conditions

Paweł Gąsior (pawel.gasior@ipplm.pl)
Agata Czarnecka, Waldemar Figacz, Ewa Kowalska-Strzęciwilk, Monika Kubkowska
Institute of Plasma Physics and Laser Microfusion

Abstract

Methods for measuring the fuel retention and characterization of the wall deposition in ITER and other future thermonuclear devices have high priority in EFDA programme. Several laser techniques, like LIBS (Laser Induced Breakdown Spectroscopy), LIDS (Laser Induced Desorption Spectroscopy) or LIAS (Laser Induced Ablation Spectroscopy) are considered as a candidates for tritium measurements as well as erosion and deposition of reactor wall materials. Presented work was performed under EFDA WP11-ETS-DTM-01-05-02 task in frame of Dust and tritium Management. Applied in measurements LIBS method is good for characterization of chemical composition of ablated materials. Laser experiments were performed with the use of ITER-like samples –with DLC and mixed of W:Al:C layer with Deuterium content. As a substrate, tungsten was used.

Introduction

The idea of the research program performed at the Institute of Plasma Physics and Laser Microfusion was to test reliability of the LIBS (Laser Induced Breakdown Spectroscopy) method in the detection of the chemical components of ITER relevant (co)deposits by the LIBS investigation of calibrated samples in various irradiation conditions and comparison of obtained spectral line intensities.

The samples with DLC (Diamond-like Carbon) and W:Al:C layers were investigated in vacuum as well as in ambient atmosphere conditions. Two types of laser have been used which allowed for observation of the behaviour of the spectral lines in different fluence/power density regimes. Two types of the observation of the laser induced plasma were tested – a parallel to the target and close to co-axial with the laser beam

In data analysis the slope method has been used as well as a method based on relative ratios of the observed lines [1-2].

Experiments in ambient atmosphere

The experimental set-up is shown in Fig. 1. As the irradiation source a Q-switched Nd:YAG laser, Quantel Brio was used. The laser delivered 4 ns pulses of energy up to 70 mJ at fundamental harmonic. The pulses were focused with a lens of the focal length of 10 cm. The distance between the lens and the target was 9.6 cm. Laser induced plasma was observed by a collimator connected to ESA4000 spectrometer with Echelle optics via quartz fibre, spectral range from 200 to 780 mn, linear dispersion per pixel (24 μ m) of 0.005 nm (200 nm), 0.010 (400 nm), 0.019 (780 nm) and resolution per pixel ($\lambda/\Delta\lambda$) of 40000.

A significant disadvantage of the spectrometer was its incapability of observation of the deuterium line due to the geometry of the dispersive grating (gaps in spectra).

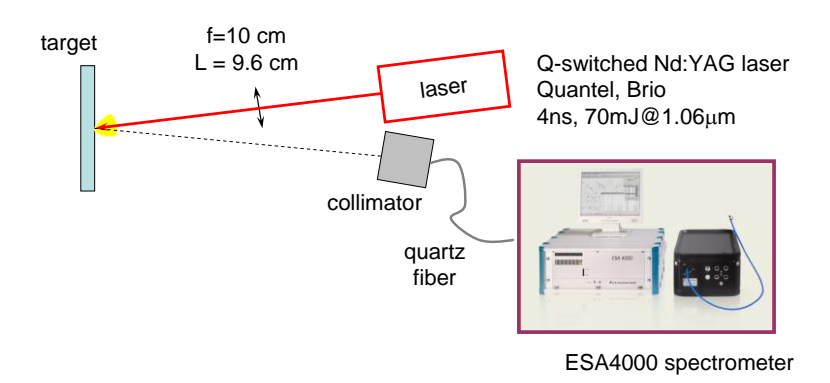


Fig. 1. Experimental set-up for the measurements in ambient atmosphere.

The experiments were conducted for three values of the power density which was defined by the adjustment of the energy of the laser pulse. The parameters in these three regimes of operation were as follows:

- 1. Laser fluence: 2.5 J/cm², Power density: 0.6 GW/cm²
- 2. Laser fluence: 14.5 J/cm², Power density: 3.6 GW/cm²
- 3. Laser fluence: 25.8 J/cm², Power density: 6.5 GW/cm².

The spot diameter for these cases was about 0.5mm.

For each single power density two series with different time delays of the signal acquisition were conducted, with delays of 0.1 and 1 ns. Acquisition time for each laser shot was 2 μ s.

To investigate the dynamics of the crater formation process, in the consecutive irradiation, subsequent spots were irradiated by the number of shots increased by ten, i.e. after delivering 10 pulses in first spot, the target was moved and in the next spot 20 pulses were delivered, then it was moved again and 30 pulses were delivered, etc. This was done for stratygrafic measurements. For applied fluences in experiments in air conditions, spectra consist mainly of atomic Carbon line and atomic tungsten line (from tungsten substrate). The experiments with various delays indicated that with shorter delay (100 ns) the amplitudes of the lines are significantly higher, but their broadening also becomes higher together with the noisy background. This feature can be well seen in figure 2 in which a single carbon line (CI 247.86 nm) (a) and neighboring carbon and tungsten lines (WI 247.78 nm) (b) are depicted. In case of b) it can be noticed that for shorter delay time the lines are not so well separated as in case of the longer delay.

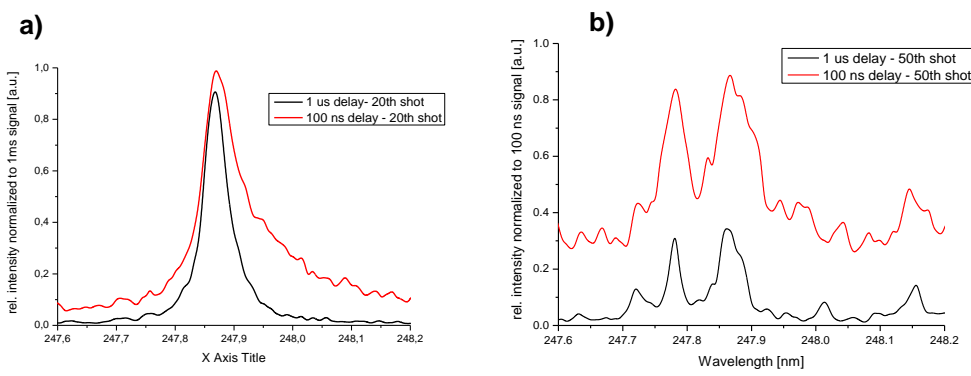


Fig. 2. Spectral lines of carbon (a) and carbon and tungsten (b) observed for different delays of observation after a laser shot.

The main part of the experiment was on comparison of the removal of the DLC layers from polished and unpolished samples. The comparison of spectra obtained during the removal process for these samples with the use of three values of power density is presented in Fig. 3 where the evolution of the 247.856 nm CI line is shown.

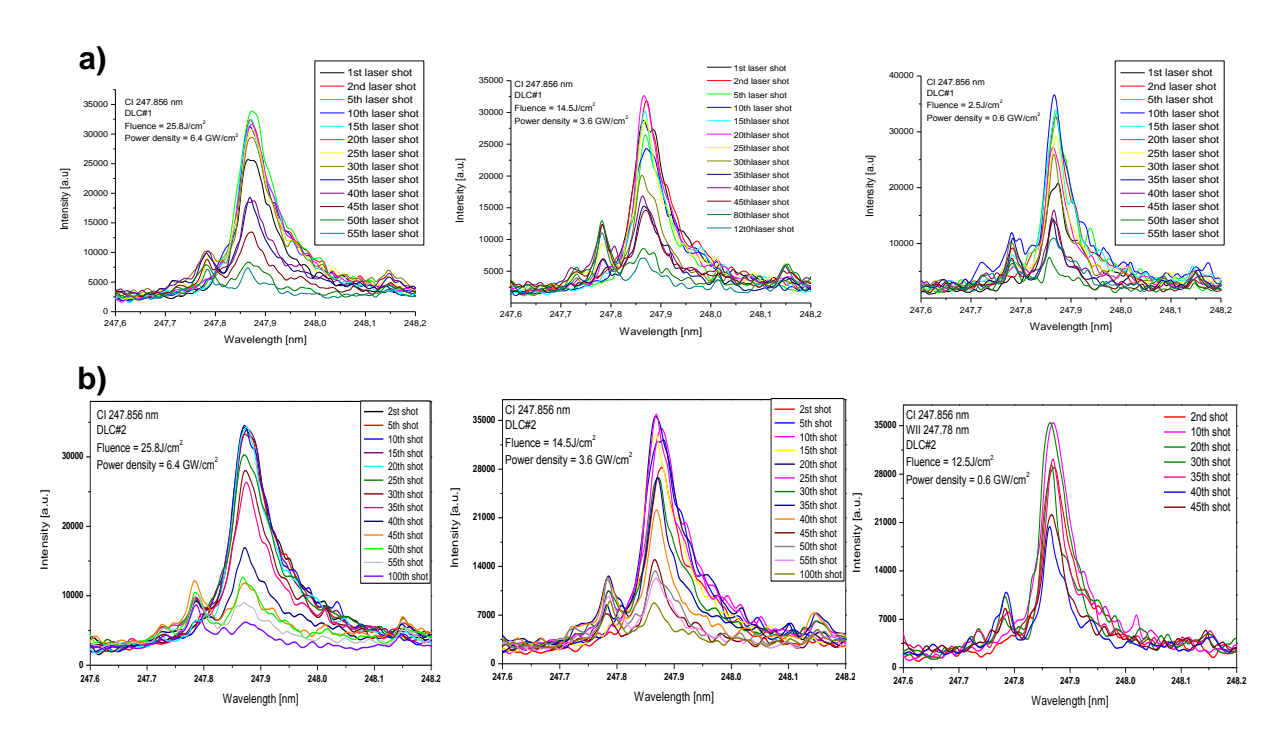


Fig. 3. Evolution of Tungsten and Carbon lines for the removal of an unpolished (a) and polished (b) DLC layer with the use of various intensity of layer pulse (the values of power density are specified on each plot).

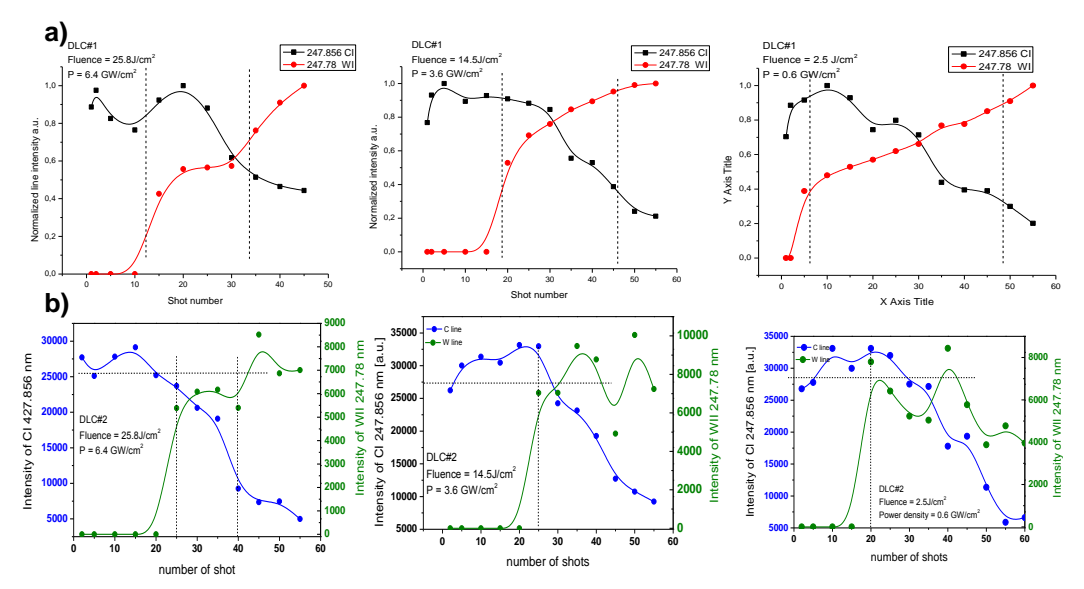


Fig. 4. Depth profile of unpolished (a) and polished (b) DLC layer removed with the use of various intensity of layer pulse (the values of power density are specified on each plot).

The removal comes faster with higher power density especially when comparing the highest and the lowest fluence. For the fluences 25.8 J/cm² and 14.5 J/cm² the difference is not so obvious but still it can be seen that for the higher value the carbon line practically disappears after 100 shots while for the lower value it is very low, but still present, in particular Fig. 6b shows that it is almost independent on power density however; the introduction of tungsten lines resulted from interaction of the laser beam with the tungsten substrate is relatively quick also for lower fluences. It can be even better seen after preparation of 'depth profiles' which are shown in Fig. 4.

The reason of relatively quick uncovering of the substrate even for the pulses with the lower laser fluence may be in the spatial profile of the laser beam which is Gaussian and even for small pulses can bring a high power density in the center of the beam.

Another apparent feature of the polished layer is that it is more difficult to be removed than the unpolished one, which may be explained by its better reflectivity especially in the early phase of the removal. The experiments shown that complete removal of polished layers was possible only in case of the application of the highest possible power density, while for the unpolished layer it was also possible with the use of the medium power density.

For the results obtained for these samples the slope method has been applied and the integrals obtained for the removal of the layers was compared with the integral obtained for bulk materials. Such a comparison is shown in Fig. 5.

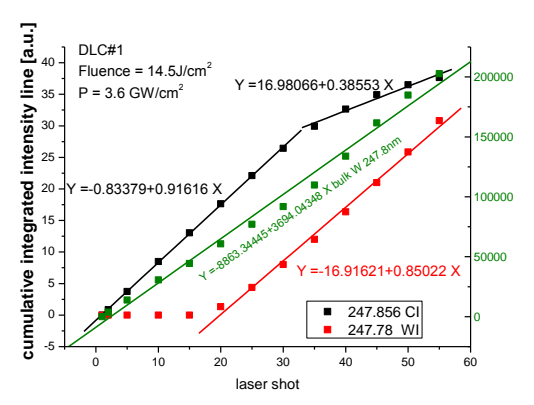


Fig. 5. Illustration of application of the slope method for the DLC sample

A profilometry map obtained for the spot after delivering 100 shots with the highest fluence is presented in Fig. 6. The crater has $5 \mu m$ depth which confirms the removal.

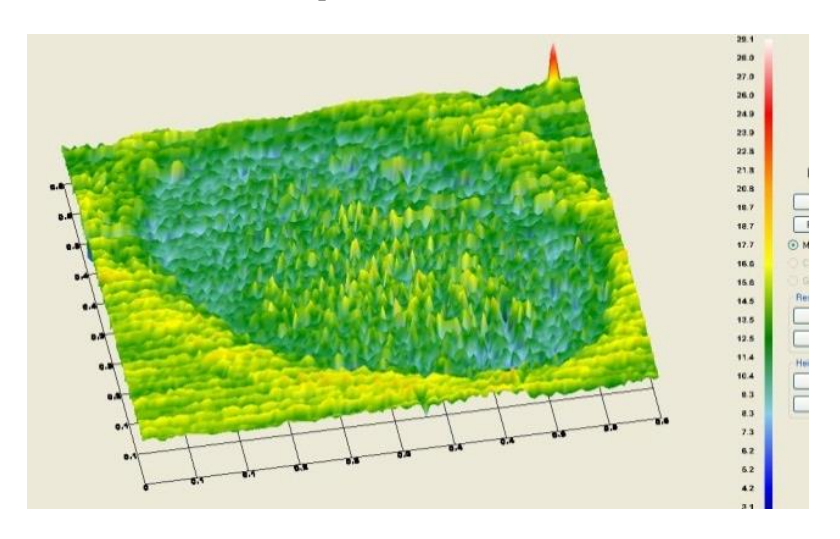


Fig. 6. Profilometry map of the crater after 100 laser shots

The LIBS procedure in ambient atmosphere was also performed for the W:Al:C samples with Deuterium content #1. As it was previously mentioned, the spectrometer did not allow for the record of the deuterium line, but the lines of the metallic components were very well seen as it is presented in Fig. 7. As it can be seen the intensity of the lines drops in subsequent shots. It can be associated with the decreasing removal rate when the 'hot' centre of the beam reaches the substrate, and most of the material is removed from the boundary area of the beam, where the power is lower and consecutively, the amounts of light emitted by smaller amounts of plasma are lower.

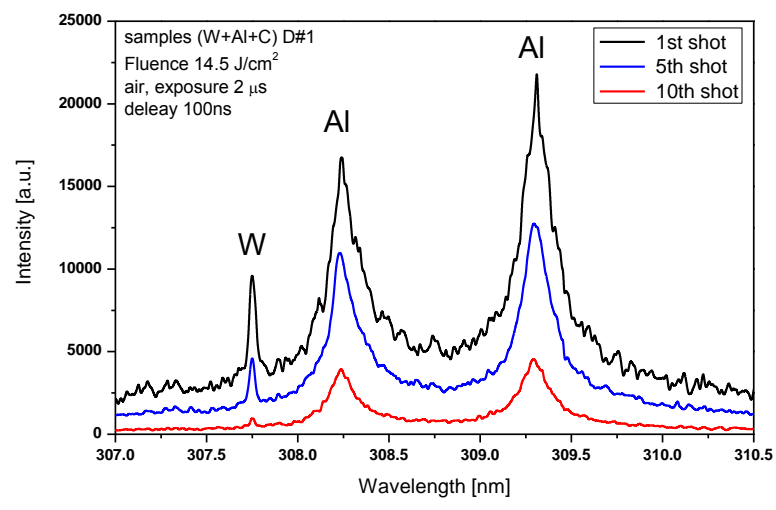


Fig. 7. Evolution of the lines of metallic components during the removal of W:Al:C layer

Another interesting feature revealed in this experiment was relative insensitivity of the method on the laser fluence. The results of the measurements of aluminum lines for three different power densities are shown in Fig. 8. The application of the slope method applied for the results obtained for a W:Al:C sample is shown in Fig. 9.

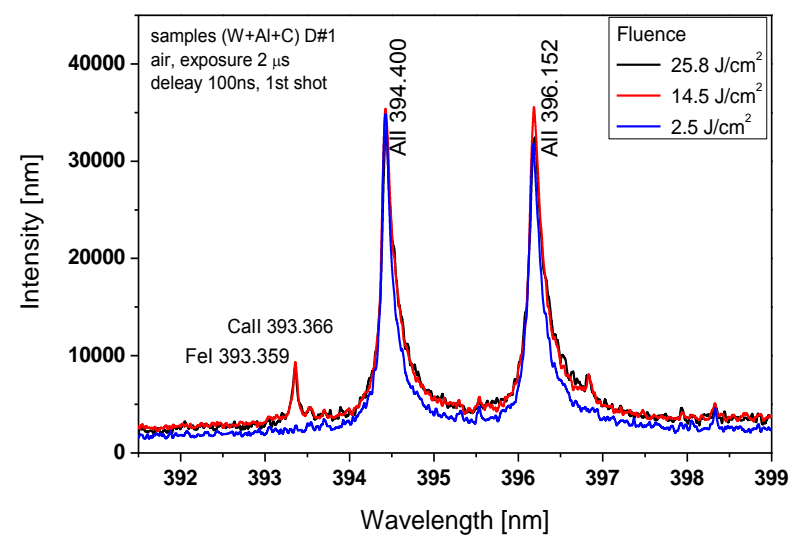


Fig. 8. Fingerprints of aluminum for three different pulse energies

For the lines of tungsten and carbon, the results obtained for the layers were consistent (the intensity of the lines obtained while irradiating the bulk were higher than those obtained when the layer was under investigation: the intensity of lines from the bulk W or Al or c should be higher than those from the layer, the idea of the slope method is to use the ratio of the slope of the deposit and the bulk as the relative fraction of content in the layer), but as it can be seen in the figure, for Al, the slope was higher in the case of the layer than in the case of the bulk. It suggested, that the neutral lines were subjected to strong reabsorption and it is rather advised to use ionic lines. Unfortunately these lines were not observed for the applied conditions with a S/N ratio which would allow for valid calculations. This shows that the neutral lines are not suitable. To apply the slop method we must compare the W and C slopes of the layer with those of the bulk.

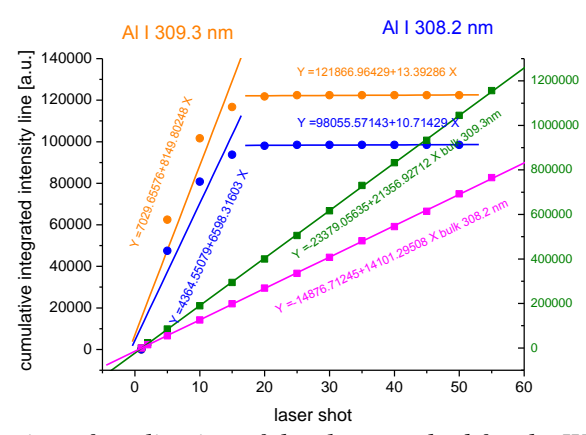


Fig. 9. Illustration of application of the slope method for the W:Al:C sample

Experiments in vacuum with parallel observation

The experimental set-up is shown in figure 10. As the irradiation source the EKSPLA Nd:YAG laser was used which delivered 3.5 ns pulses of up to 0.5 J at 1.06 μ m fundamental wavelength. The pulses were focused with a lens of the focal length of 80 cm. The distance between the lens and the target was 74 and 65 cm.

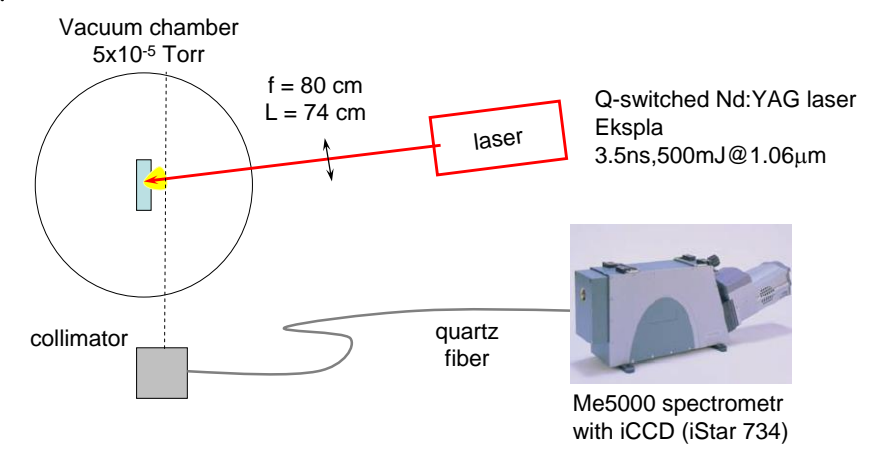


Fig. 10. Experimental set-up for the measurements in vacuum with parallel observation.

The experiments were conducted for two values of power density which was defined by the focusing lens position. The parameters in these three regimes of operation were as follows:

- 1. Laser fluence: 28. 3 J/cm², Power density: 8 GW/cm²
- 2. Laser fluence: 63.6 J/cm², Power density: 18.2 GW/cm²

Both fluence and power density refer to the beam parameters and does not take the reflection or the scattering from the target surface.

For each single power density two series with different time delays were conducted, with delays of 50 and 150 ns. Acquisition time for each laser shot was 2 μ s.

The spectra were collected for single laser shots and for accumulations of 4 shots for some experimental series. For the optical signal observation a collimator was used which was connected to the Mechelle5000 spectrometer with iCCD camera (iStar). The measured wavelength range was from 200 to 975 nm with no gaps with spectral resolution ($\lambda/\Delta\lambda$) 4000, dispersion of $\lambda/231.2$ [nm/mm] ($\lambda/16400$ nm/pixel) and wavelength accuracy < \pm 0.05 nm. The collimator was installed by the window, which allowed for the observation of plasma of the diameter of ~3 mm, 2-3 mm in front of the irradiated target. The window and the collimator position was adjusted to observe the plasma in direction parallel to the target.

For the DLC samples, removal in vacuum with the pulses of higher energy had a more rapid character than that performed in the ambient atmosphere. Evolution of registered spectral lines and depth profiles obtained for DLC sample are presented in Fig. 11. In comparison with the previous experiment it took less laser pulses to remove the layer and the process yet after ~20 pulses were similarly as complete as after 100 in the previous scheme.

With regard on the deuterium contents in both types of samples the deuterium line has been seen in a first few shots. As it can be seen in Fig. 12, the deuterium line lasted for a bit longer time in the DLC #1 sample, but in DLC #2 it had a bit higher amplitude, especially if it was referred to the intensity of the concomitant carbon sample.

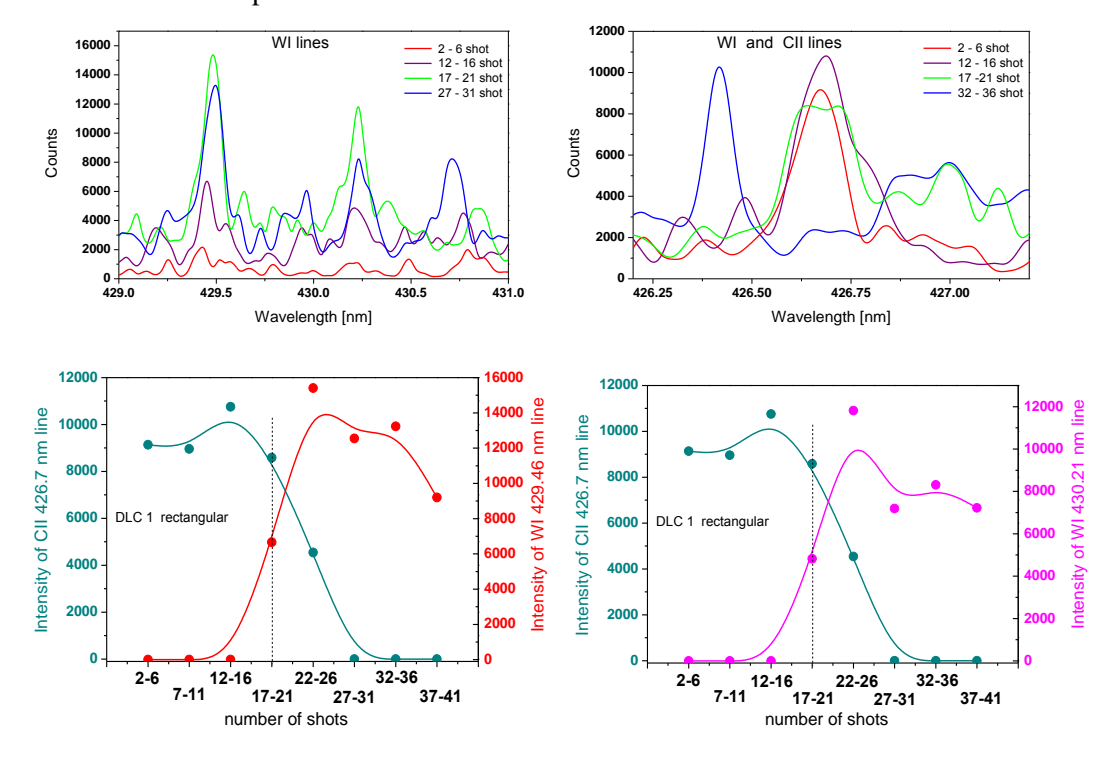


Fig. 11. Evolution of spectra lines during the removal and chemical contents depth profiles based on LIBS

As the measured amplitudes of the deuterium lines were low and the real amounts of deuterium is not sure in both calibration samples, it was impossible to quantify the results into real value; however; the results suggest that the amounts of deuterium or at least its depth profile differs in respect of the sample.

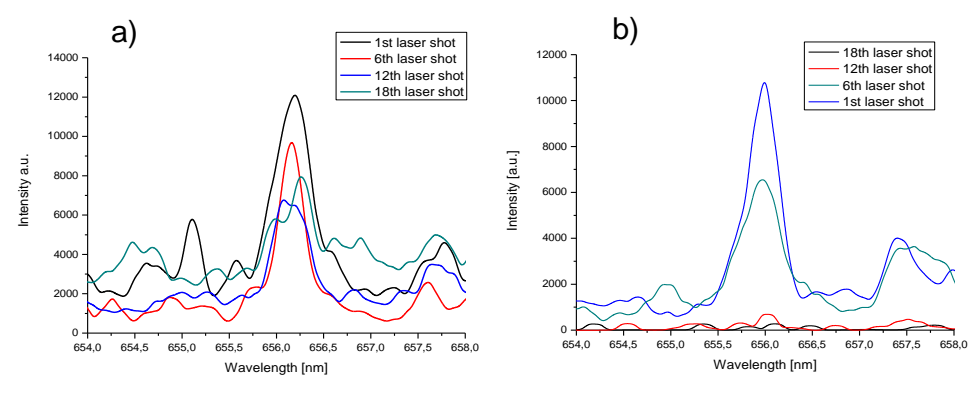


Fig. 12. Comparison of the evolution of Deuterium lines (D α 656.2nm) in DLC#1 (a) and DLC#2 (b) samples

The investigation of the W:Al:C samples was mainly focused on detection of deuterium lines and detection of differences of their amplitudes and behaviour between samples signed as W:Al:C #D1 and W:Al:C #D3. The W, Al and C components of both types of samples gave rather repeatable signals in the optical spectra, which example is shown in Fig. 13.

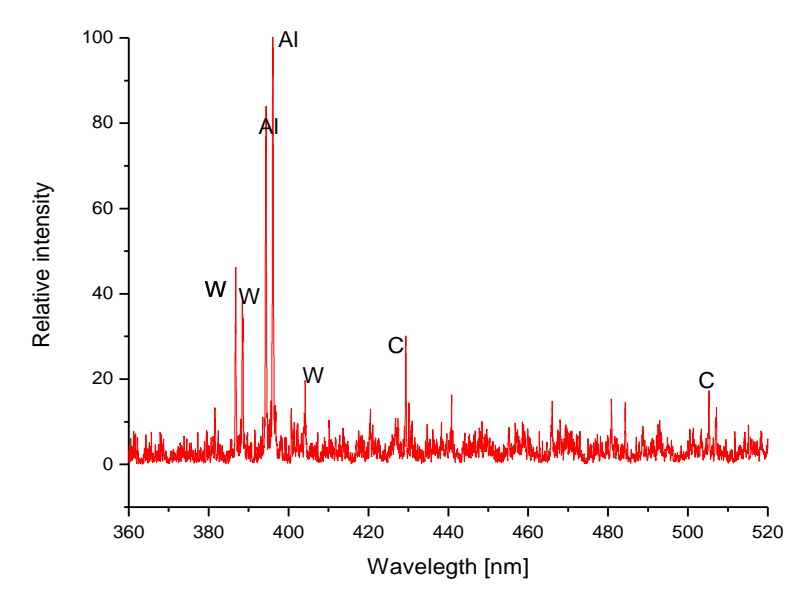


Fig. 13. A sample spectrum taken for a W:Al:C sample

Typical fluctuations of the observed lines were in range of ~25-30 %. These fluctuations for observed aluminum lines for arbitrarily chosen laser pulses are presented in Fig. 14.

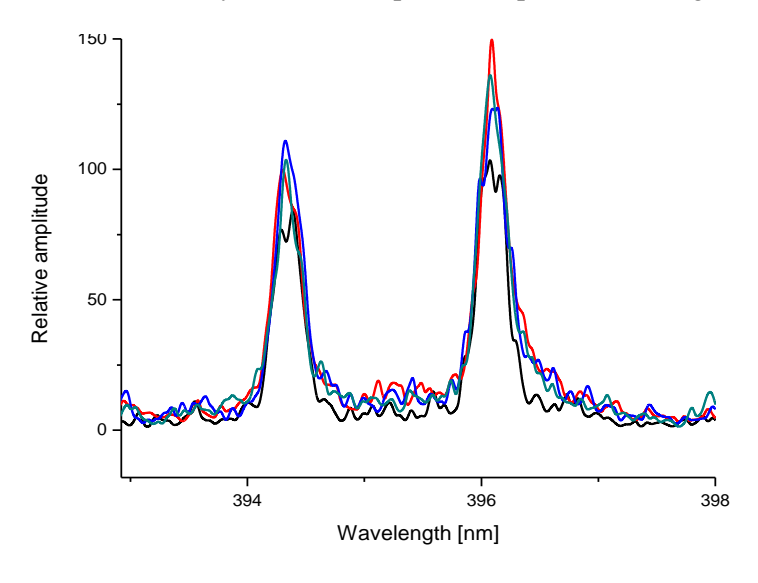


Fig. 14. Shot-to-shot fluctuations of Al lines in a W:Al:C #D1 sample

Investigation of the deuterium contents indicated that there is obvious difference in optical signals for the samples. However the amplitude of the deuterium line in the W:Al:C #D1 sample is higher for the first laser pulse, it rapidly disappears in next shots, while for the W:Al:C #D3 sample the amplitude is lower, but the line is still detectable for at least 3 laser pulses. The spectra observed for these samples are presented in Fig. 15. The low levels of the signals cannot exclude the possibility that they are the result only of the presence of small amounts of water on the surface.

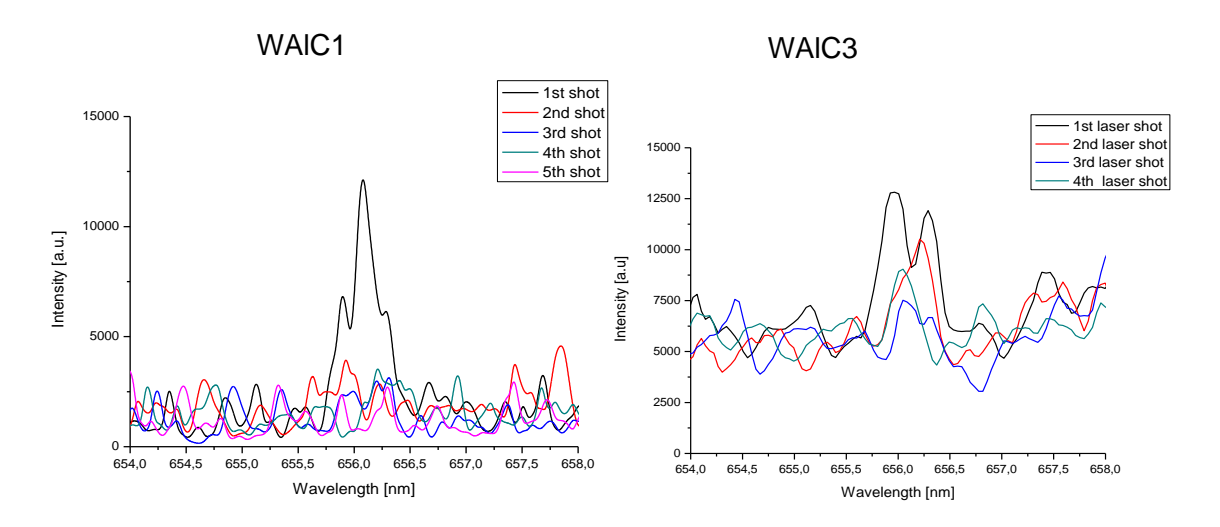


Fig. 15. Comparison of behavior of deuterium line in W:Al:C_1(left) and W:Al:C_3 sample (right)

Despites the differences in the observed deuterium lines are firm, the comparison of these lines with other lines in the spectra (i.e. W, Al and C lines) suggest that in the provided sample the deuterium contents is very low, which significantly hampers quantitative analysis.

Experiments in vacuum with close to co-axial observation

The experimental set-up is shown in Fig. 16. The parameters of the laser system, the spectrometer and the irradiation parameters were the same as those for parallel observation. In the case of this experiment the collimator was installed in a port which was a 'mirror reflection' of the port which was used for the laser beam delivery. Assuming the axial symmetry of the plasma, the angle of observation was then the same as the angle of incidence of the laser beam.

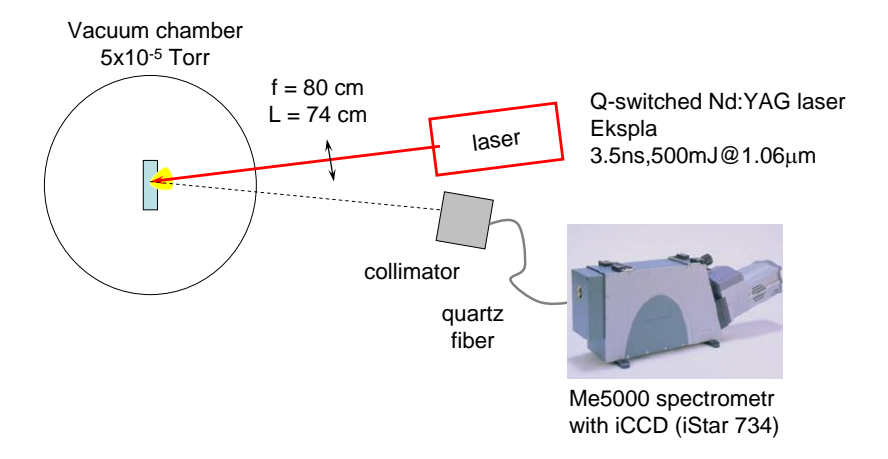


Fig. 16. Experimental set-up for close to co-axial observation.

In the experiments, the spectra for single laser shots were collected for 10 starting pulses in each experimental series, and for the subsequent pulses, accumulations of five shots were acquired.

In this part of experiment W:Al:C samples have been investigated in order to perform slope analysis. All data have been subjected to absolute calibration and then, based on the intensity of ionic lines, the depth profiles have been derived. The intensity of the tungsten line has been used for normalization of carbon and aluminum ionic lines. The results of the depth profile calculation and its close-up to first 10 shots are presented in Fig. 17. Note that for first 10 shots spectra from single shots were taken, and for further shot the measurements were done as accumulation for 5 shots and for the purpose of further calculation, the average values were used.

As it can be seen in the figures, after 10 shots which remove the most of the layer, Aluminum and Carbon lines drop quickly while the intensity of the Tungsten line increases. After application the slope method to the obtained data the results were as those presented in Fig. 17.

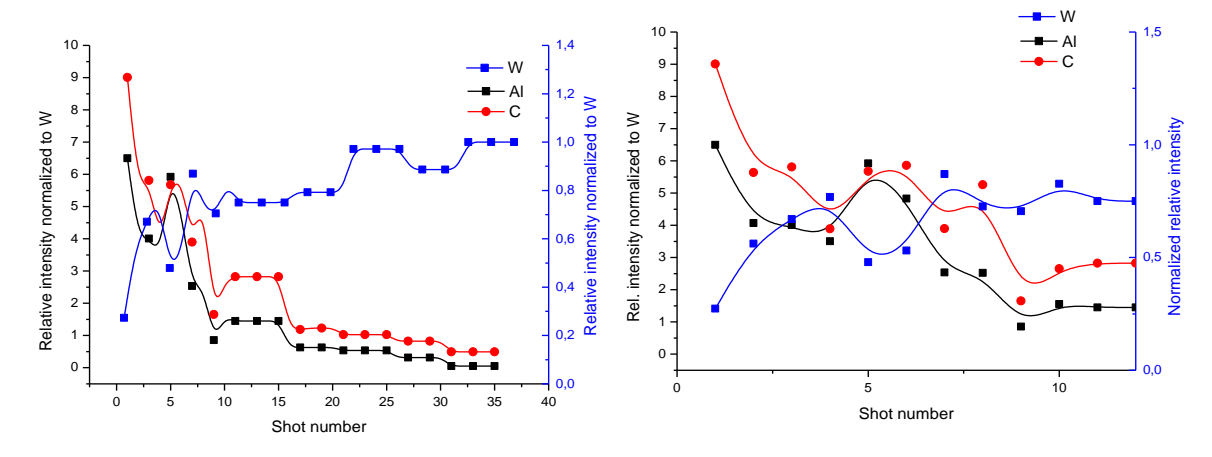


Fig. 17. Depth profile of the W:Al:C #D1 sample (left) and its close-up to first 10 shots

As it can be seen in the figure 18 the curves corresponding to the intensity of the spectral lines corresponding to the chemical components of the sample (W II 373.7 nm, Al III 448.0 nm, CII 426.7 nm, CIII 466.4 nm) were divided into to parts: first one which included first ten shots corresponded to the part of process in which the laser pulses interacted mostly with the layer and the second one which included last 15 shots corresponded to the interaction of the pulses mostly with the substrate and small remains of the layer. The middle part of the process where it was expected that the central region of beam interacts with the uncovered surface but a significant remaining area of the beam interacts still with the layer, was excluded from this analysis.

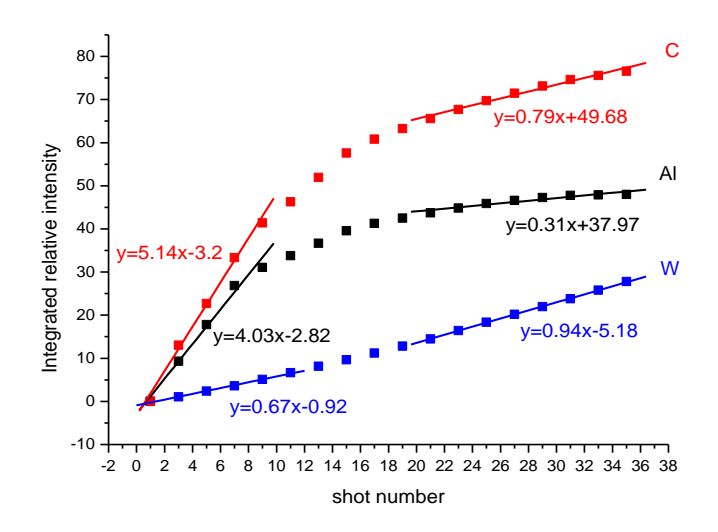


Fig. 18. Integrated intensity of W, Al and C lines and their linear fits

Based on this results the chemical contents of the sample was assessed as: 52% C, 41 % Al, 7% W. It is worth mentioning that the slopes of the components well correspond to the composition of the layer given by the manufacturer. For the derivation the following lines have been used: (W II 373.7 nm, Al III 448.0 nm, CII 426.7 nm, CIII 466.4 nm). In the calculation the integral value of the lines corresponding to the elements were divided by the sum of the integrals. For the estimation of the carbon contents both CII and CIII lines were used. The results of analysis of samples W:Al:C #D1 and W:Al:C #D3 gave very similar results.

Concerning analysis of deuterium line, in this part of the experiment the results were the same as in the experiment with the parallel observation. Deuterium was present only in the first shot for the W:Al:C #D1 sample and small deuterium peaks were observed for first 3-4 shots at the W:Al:C #D3 sample. The measurements suggested that deuterium content was significantly lower than 10 % with rather poor accuracy. This estimation was based on a poor amplitude of deuterium line in comparison to other lines and also to the amplitude of deuterium line which was previously measured in deuterium-rich deposits, eg. from the TEXTOR limiter.

Fast Fourier Transfor (FFT) based model to interpret the measurements under vibrations by identifying the mechanical vibrations from the erosion measurements

The study on the development of the signal processing algorithms for analysis of the speckle interferometry for the next-step fusion devices in vibrational environments led to conclusion that the operation of removal of the harmonic components of vibration can be implemented by means of application of a digital FIR (Finite Impulse Response). In the FIR filter the output signal is calculated with the use of N subsequent samples of the signal where N is the order of the filter. The parameters $b_1 - b_N$ are the coefficients of the filter which may be adjusted in the way to outfilter or pass a needed frequency band from the signal. A FIR filter can be developed by means of the FFT (Fast Fourier Transform) transform blocks in the way which is shown in Fig. 19.

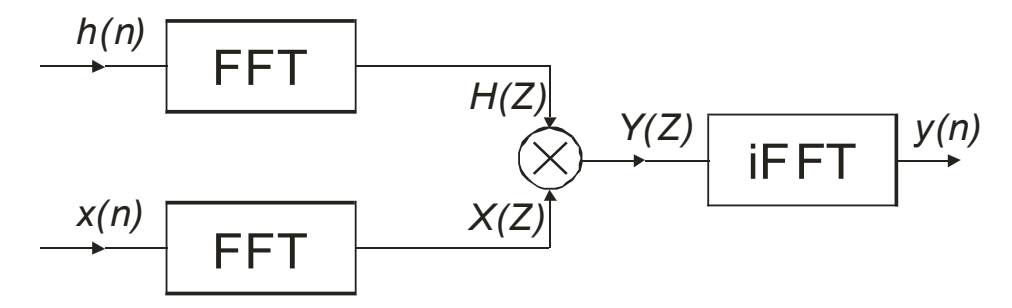


Fig. 19. FFT-based on FIR filter

Thanks to the application of FFT algorithms the efficiency of calculation of the discrete convolution is better which makes the filter operation faster.

Another type of filter which can be implemented for this task is a IIR (Infinite Impulse Response) filter which in contrary to the FIR filter includes a feedback loop. This type of filter facilitates faster operation but also is less stable which may lead to generating oscillations.

The last method which has been taken into account was the LMS (Least Mean Square) filter based on adaptive signal processing. A basic scheme for this algorithm is shown in Fig.. 20.

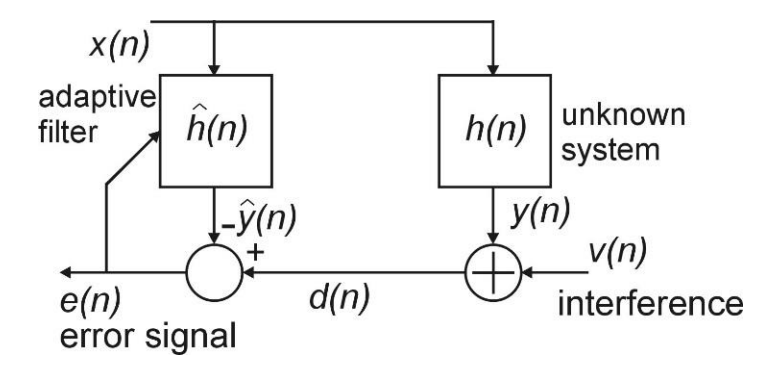


Fig. 20. Basic scheme for the LMS adaptive filter

Conclusion

The experiments performed at the IPPLM showed the relevancy of the LIBS method for measuring chemical contents of mixes composed of Aluminum, Tungsten and Carbon as well as for detection of small amounts of deuterium in these mixes. It has been shown that the analysis gives consistent results in vacuum as well as in the ambient atmosphere.

The chemical content of W, Al and C in the W:Al:C sample was assessed with relatively good accuracy, however, it needs to be mentioned that for really reliable analysis more samples with more diverse composition should be investigated.

The trouble with the method originated with difficulty of reliable analysis of deuterium contents – the provided samples contained too small amounts of deuterium and in too shallow layers to be precisely analyzed. The measured deuterium lines had amplitudes incomparably lower than those which were recorded eg. in analysis of TEXTOR or AUG co-deposits in very similar experiments. Analysis which was performed with the use of low energy, well-focused laser pulses shown that such pulses are relevant for LIBS measurements and have an advantage of inflicting lower damage to the target with still reliable information on the chemical composition of a top layer.

In the field of development of algorithms for signal processing for speckle interferometry in vibration conditions, a few interesting algorithms have been studied and proposed. Parts of the code for LMS have been developed.

Collaboration

Association EURATOM – FZJ Juelich Association EURATOM – ENEA Frascati Association EURATOM – TEKES Association EURATOM – FOM_Rijnhuizen

References

- [1] A. Malaquias et al., 20th PSI Aachen, Journal of Nuclear Materials, 2013, in press
- [2] S. Almaviva, L. Caneve, F. Colao, R. Fantoni, G. Maddaluno, J. Nucl. Mater. 421,73 (2012).

Extending knowledgebase on fuel release (and retention) of Be-containing mixed materials

Paweł Gąsior (pawel.gasior@ipplm.pl)
Agata Czarnecka, Monika Kubkowska,
Ewa Kowalska-Strzęciwilk
Institute of Plasma Physics and Laser Microfusion
Łukasz Ciupiński, Elżbieta Fortuna-Zaleśna,
Warsaw University of Technology

Abstract

Although beryllium is an element which is crucial for construction of plasma facing components the laboratory experiments with this material are strongly limited by safety regulations and due to this, the need for finding an analogue for beryllium has emerged. As the analogue material aluminium has been proposed but the similarities and differences between these materials have not been precisely studied. The goal of the research in the framework of this task was comparison of physical and chemical properties of aluminium and beryllium. The investigation was especially oriented on comparison of behaviour of the elements in conditions of pulsed laser interactions.

It has been found that thermal properties differ relatively smaller than if comparing with other elements and in view of other laser experiments, crater formation is rather similar. Also it has been found that it is possible to investigate both materials with the LIBS technique.

Introduction

In many laboratory experiments on investigation of plasma-wall interactions there is a need of excluding beryllium due to safety regulations. On the other hand beryllium is one of crucial elements which is present in mixed materials and should be included into research. Due to these reasons it is advised to find an element which would be allowed by safety regulations and which has similar physical and chemical properties as beryllium. As such a material aluminum has been proposed. The goal of the study which is the subject of this task was to find similarities and differences between physical and chemical properties of aluminum and beryllium.

Task achievements

Literature comparative study has been conducted. While the database on laser ablation of aluminum is relatively broad, for beryllium it is not well established and it mostly concerns some research on interaction with high energy laser pulses for NIF.

Physical and chemical properties of Al and Be have been compared. The stress was put mainly to thermal properties as they are crucial in terms of discussion on the ablation. Although thermal conductivity of both materials is relatively close (18.5 % larger for Al) also in comparison with other metals e.g. Mg, Fe, Cu, Ga, etc., the difference in the thermal diffusion is larger (~65% larger for Al). Also it should be noted that both elements tend to form different crystal structures – face-centered cubic for Al and hexagonal for Be. Due to this Be less obey the Lindemann law so the melting behaviour of the elements may significantly differ especially in view of another obvious difference - the melting temperature of the elements.

The behavior of a surface subjected to a high heat load (in our case a high intensity laser beam) which leads to material ablation/spallation in terms of both products released during the process and post-process surface morphology depends also on its mechanic properties. Beryllium hardness and Young modulus are significantly higher for Be. Speed of sound is more than two times higher for beryllium which may also affect the ablation mechanism in different way in the investigated materials.

A glaring similarity in the chemical properties of both elements is in their capacity of oxide formation. On the other hand there is a difference in the hydrogen isotopes solubility in Aluminum and Beryllium and it is Beryllium in which hydrogen trapping is significantly stronger.

In some experiments with laser ablation of aluminum it was shown that intense laser pulses in range of a few ns pulse length and high power density of 10^9 - 10^{10} W/cm² can significantly damage the substrate, but pulses of lower power density (several 10^6 W/cm²) and ~100 ns length), which still can be used for fuel removal do not lead to the ablation of the material, however, longer exposition may lead to crack formations. These disadvantageous features may be avoided by optimization of the exposure time, which in the real-machine detritation would be adjusted by the scanning velocity.

Preliminary studies of laser interactions with beryllium targets which were aimed on LIBS analysis did not show striking differences in the crater formation in comparison to aluminum It allows to believe that laser treatment with similar pulses would not damage beryllium in a more severe way, thus, the layer properties should not deteriorate in terms of resistance to hydrogen isotopes trapping. On the other hand, based on the comparison of the chemical and physical properties described above, it is highly probable that optimized parameters of the laser beam for removal of fuel/deposits from aluminum and beryllium substrates can differ. nevertheless, it needs to be remarked that in Beryllium, due to stronger hydrogen trapping, the effects in the hydrogen isotopes retention may be increased by cracks and defects in comparison with aluminum.

While for ~100 ns, part of mJ pulses the threshold for removal of bulk aluminum was found at the IPPLM not to be lower than ~6 MW/cm², such a threshold has not been yet found for Beryllium. In the case of the higher power density laser pulses $(10^9-10^{10} \text{ W/cm}^2)$ the ablation of Beryllium will be dominating process in the similar way as it is for aluminum. The rates of removal may differ, but preliminary experiments with LIBS on beryllium do not indicate that the difference would be dramatic.

Conclusions

The conducted research allows to state that the aluminum is the closest proxy for beryllium in terms of research aimed on the investigation of materials for PFC in fusion reactors, but the straightforward interpretation of the results obtained for Al as if they were obtained for Be cannot be recommended. On the other hand, the experiments on the aluminum may give o good view of general behavior of beryllium subjected to the same experimental conditions.

In near futures there are experiments on laser ablation of Beryllium planned in a couple of labs and these new experiments will definitely decide the question.

Collaboration

Association EURATOM - TEKES

References

- 1. A. Hassanein, D.A. Ehst, Journal of Nuclear Materials 212-215 (1994) 1272-1277
- 2. Ph. Mertens, TF-D Meeting, Oct. 22nd, 2003, Contributions to the spectroscopic identification of sources: hydrogen isotopes and beryllium at the edge
- 3. Leon J. Radziemski, David A. Cremers, Thomas R. Loree, Spectrochimica Acta Part B: Atomic Spectroscopy, Volume 38, Issues 1–2, 1983, Pages 349–355
- 4. Leon J. Radziemski , Thomas R. Loree , David A. Cremers , Nelson M. Hoffman, Anal. Chem., 1983, 55 (8), pp 1246–1252
- 5. Damian C. Swift, Thomas E. Tierney, Sheng-Nian Luo, Dennis L. Paisley, George A. Kyrala et al., Phys. Plasmas 12, 056308 (2005)
- 6. P. Gasior, M. Bieda, M. Kubkowska, R. Neu, J. Wolowski, ASDEX Upgrade Team, Fusion Engineering and Design, Volume 86, Issues 6–8, October 2011, Pages 1239-1242,

Assessment of Fuel Removal Methods and Dust Generation – dust collection in aerogels

Ewa Kowalska-Strzęciwilk (ewa.kowalska-strzeciwilk@ipplm.pl)
Agata Czarnecka,
Waldemar Figacz, Paweł Gąsior, Monika Kubkowska
Institute of Plasma Physics and Laser Microfusion

Abstract

In a tokamak device fuel-containing dust can be produced during the process of the fuel removal procedures of wall materials co-deposits as well as in transient events when abnormal thermal loads are deposited at the wall. Even some dust is produced during normal operation of the device. Laser cleaning techniques have shown a very good efficiency in cleaning thick co-deposits.

In order to facilitate the dust cleaning procedures and to assess the possible impact of the fuel containing dust on plasma operation it could be very useful to investigate the deuterium contents of the dust in respect to its grain size and velocity at which it was rejected.

To complete this research TEXTOR sample with thick (40-60 μ m) a-C:D co-deposit were irradiated by 3.5 ns, 0.5 J Nd:YAG laser pulses. The release of dust was observed by the fast CCD camera with the shortest integration time of 10 μ s and the particles were collected by aerogel catchers installed at various distances from the target. The experiments were conducted in vacuum and in O2 atmosphere at different pressures.

The recorded CCD images allowed to estimate the velocity of the large dust particles at 100 m/s which was preliminarily confirmed by the investigation of the aerogels by collaborative laboratory – Alfen Lab in Swedend.

Introduction

Dust generation in the interaction of plasma-facing components (especially those covered with deposits) with pulsed laser beams is not only a phenomenon associated with laser ablative fuel removal but also can simulate the effects of transient heat loads on the wall of thermonuclear reactors. Due to this it is valuable to investigate of the dust parameters (grain size, initial velocity) influence on their fuel content. Another issue is the dependence of the dust parameters on the power density of the laser beam power density.

To investigate this areas the research on this task included CCD observation of the dust generation process and collection of the dust particles in aerogel catchers provide by VR.

Experimental Set-up

Photos of the experimental Set-up and the installation of the target and the aerogel dust collector inside of the vacuum chamber are shown in figure 1 a and b.

As the target the ALT-II TEXTOR limiter sample covered with a thick codeposit was used. In subsequent experimental series the aerogel collectors were installed at distance from a part of centimeter (0.2 cm) to 1.5 cm from the irradiated area.

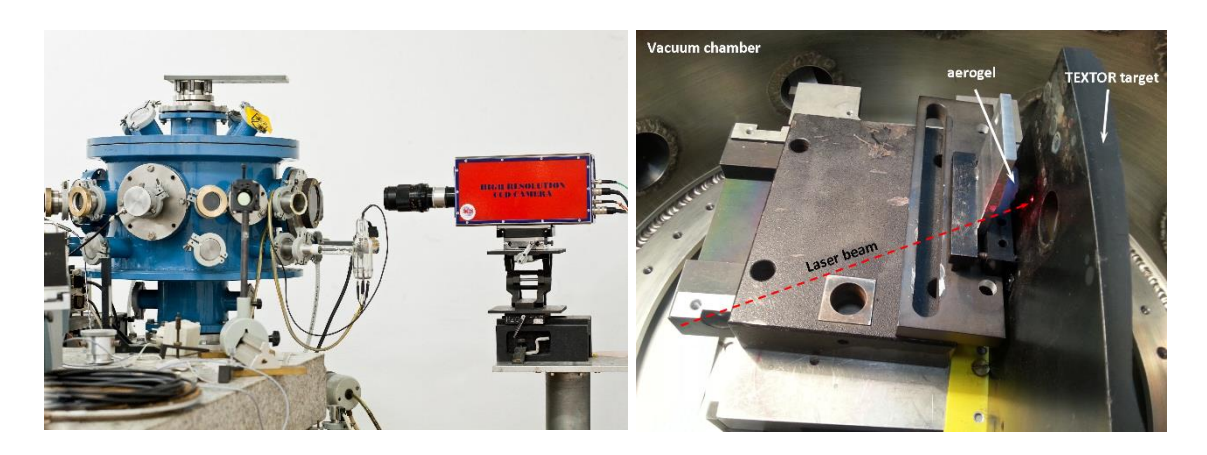


Fig. 1. Photos of experimental set-up (left) and target and aerogel installation in the vacuum chamber (right)

The sample was irradiated with 5 to 10 laser shots in vacuum (5×10^{-5} mbar) or in oxygen atmosphere (10 and 100 Pa). The frame of the CCD observation was varied from 10 μ s to 1 ms. After the experimental series at the IPPLM the aerogel collectors with accumulated dust were sent for further analysis to VR in Sweden.

Results

CCD observation of the dust particles confirmed that they reach the aerogel surface from which they can be reflected, but on the other hand the most often are absorbed. Sample images obtained for various experimental conditions are presented in figure 2.

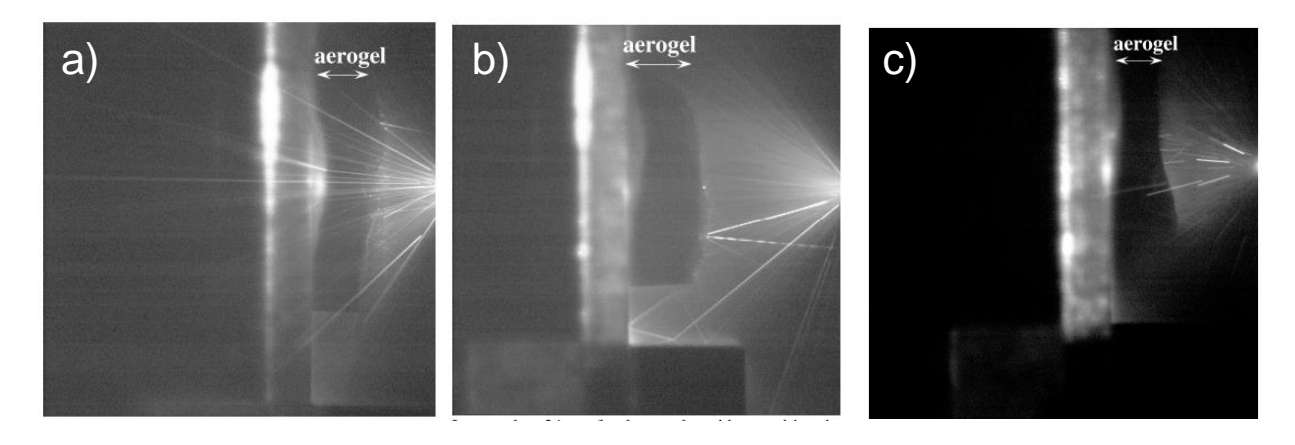


Fig. 2. Image taken by the CCD camera for 41.5 μ s delay, 100 us acquisition time in vacuum (a), 34.5 μ s delay, 1 mss acquisition time in vacuum (b), 114 μ s delay, 100 μ s acquisition time in 100 Pa O₂ atmosphere

Basing on the length of the tracks the velocity of dust particles was assessed at 100 m/s in vacuum and at 10-50 m/s in O_2 atmospheres depending on pressure. These results were confirmed by preliminary investigation at VR.

The scope of the further investigation at the VR which are the main part of the task will be in analysis of the collected dust particles by MBA.

Conclusions

The experiments confirmed that CCD observation of the laser produced dust particles is a usable technique and allows for assessment of basic parameters of the dust. It has been also showed that aerogel dust collectors are a possible device for dust diagnostics as good collectors for post-mortem analysis.

Collaboration

Association EURATOM - VR

References

[1] W.M. Shu, Y. Kawakubo, M.F. Nishi, Appl. Phys. A76 (2003) 421

[2] H. Bergsåker, B. Emmoth, P. Petersson et al., J. Nucl. Mat., 362, 215 (2007)

2.4 JET and ASDEX UG activities

Participation to the JET experimental campaigns C29(8) – C30

The IPPLM team (monika.kubkowska@ipplm.pl, marian.paduch@ipplm.pl)
Institute of Plasma Physics and Laser Microfusion

Abstract

The main tasks realized during the Campaigns on JET were oriented on measurements of the x-ray radiation emitted by Ni²⁶⁺ and W⁴⁸⁺ ions using KX1 spectrometer and spectroscopic measurements of Ni, W impurity during ICRH heating using the VUV spectrometer. In the frame of Fusion Technology the neutron activation measurements were performed as a benchmark against numerical calculations for neutron diagnostics calibration at JET, and the measurements and calculation of neutron streaming through JET Torus hall were accomplished. Moreover, the numerical calculation with COREDIV code for JET ILW discharges was done.

Introduction

The achievements of IPPLM tasks during the last experimental campaign at JET (C30 campaign at summer 2012) were related to the installation of two GEM detectors into the ending port window of the KX1 x-ray diagnostic. The upgraded KX1 system proved capable of providing data with a high spectral (comparable to the natural linewidth) and time resolution ($\Delta t \sim 10$ ms). The information yielded by KX1 will reveal the spread of tungsten throughout the core of the plasma.

In addition, using the VUV spectrometer the influence of the plasma shape, the ICRH antenna phasing, and the minority cyclotron resonance position on the Ni content was investigated and the contribution of Ni to $P_{\text{rad,bulk}}$ was evaluated. It was observed that the main radiation came from W, Ni it was also contributing to $P_{\text{rad,bulk}}$ up to a 20 % during ICRH, depending on the plasma conditions.

Also, a new set of multi-element samples were prepared for cross-calibration of other neutron diagnostics against KN2. The samples activity after 3-hours irradiation by $4x10^9$ -yield Cf-source, located 30 cm below irradiation end (located in upper position in Octant 3) has been predicted. The evaluation of the activity was done for 18 mm in diameter and 1 mm thick samples. The set of samples will be very usefull for future in situ calibration of neutron diagnostics on JET using a Cf source. Additionally, a study within JET FT-12-5.45 aiming at validating the calculation of neutron streaming through ducts and of the dose rates outside of the JET hall was performed with TLD technology.

Preliminary measurements of the x-ray spectra registered by KX1 diagnostic

The KX1 x-ray diagnostic has been upgraded at JET. Two diagnostic channels were prepared for Tungsten and Nickel impurity monitoring. By means of cylindrically curved (1011) quartz (2d=6.68 Å) and (220) Ge (2d=4.00 Å) crystals used in order to diffract the 7.8 keV and 3.8 keV photons, the diagnostic monitors the x-ray radiation emitted by Ni²⁶⁺ and W⁴⁸⁺, respectively. The KX1 spectrometer operates in so-called Johann geometry with a very large focal length. The Rowland circle radius was 2R=24.98+/-0.15m. The horizontal and vertical alignments of both crystals have been verified and synchronized with mechanical parameters of the spectrometer. Two new GEM (Gas Electron Multiplier) x-ray detectors have been installed into the ending port window of KX1 diagnostic. Additionally, at the W diagnostic channel a He buffer has been installed in order to optimise the x-ray transmission in 2.4 keV. After its successful installation, test measurements were performed at the Ni diagnostic channel. It was demonstrated that the KX1 diagnostic is able to provide data with a high spectral (comparable to the natural linewidth) and time resolutions (Δt~10 ms). It has been shown that KX1 should resolve x-ray radiation originating from different reflection orders.

Ni behaviour in ICRF and NBI heated discharged

The Ni and W impurity release during ICRF and NBI operation with the ILW was investigated. Spectroscopic measurements were obtained using the VUV spectrometer. The L-, H-mode discharges and divertor/limiter configurations were examined. The influence of the plasma shape, the ICRH antenna phasing, and the minority cyclotron resonance position on the Ni content was investigated. The behavior of the Ni content in different scenarios was correlated with the bulk radiated power ($P_{rad,bulk}$). The contribution of Ni to $P_{rad,bulk}$ was evaluated.

The application of ICRF power results in higher Ni content in the plasma core compared with NBI heating, in both L- and low power H-mode discharges, in divertor and limiter configurations. Differences in plasma wall–interaction for the different plasma shape, antenna phasing, plasma-antenna distance, and the minority cyclotron resonance position constitute another factor influencing impurity release. For the same ICRH power level, -90° phasing gives a significant higher Ni concentration than in the case of dipole phasing. No obvious dependence is seen during ROG variation. The Ni content is less pronounced during the operation of antenna C and D than during A+B operation although the same total power level was coupled. This can be due to differences in antenna spectrum (for A and B only 2 over 4 straps are powered) that could results in higher high antenna near fields and higher surface of interaction (two antennas are used). The Ni content decreased with increasing line averaged edge plasma density, measured by interferometry, also increased with plasma triangularity. As larger Ni concentrations are measured with ICRH than with NBI heating, not surprisingly higher bulk radiated power (P_{rad,bulk}) is measured when using ICRH compared to NBI. It was observed that although with the new Be/W metal wall the main radiation came from W, Ni was also contributing significantly to Prad, bulk up to a 20 % level during ICRH, depending on the plasma conditions. For the same power level, central ICRH resulted in higher Ni concentration in the plasma core in comparison to off-axis ICRH. The higher central T_e and diamagnetic energy observed with on-axis heating, difference in transport or higher Ni

The neutron measurements as a benchmark against numerical calculations for neutron diagnostics at JET

The neutron diagnostics calibration at JET is a good opportunity to test the Monte Carlo (MCNP) neutron transport calculations. The well-defined calibration source allows verifying correctness of the MCNP model. As neutron detectors implemented in such model shall be the samples of materials with well-know neutron reaction cross-section. The activation measurements during neutron calibration should be, therefore, a benchmark against the MCNP calculations. The IPPLM Association team prepared above mentioned measurements.

To perform the activation measurements at JET the KN2 system shall be used. The irradiation end located in upper position in Octant 3 (3U) is useful especially due to location inside the vacuum vessel. Taking into account the neutron energy spectrum in 3U obtained by means of MCNP calculations the following reactions have been chosen to record the neutrons emitted by Cf-252 source: In-115 (n,g) In-116, U-238 (n,g) U-239, Au-197 (n,g) Au-198, Mn-55 (n,g) Mn-56, W-186 (n,g) W-187, In-115 (n,n') In-115m, In-113 (n,n') In-113m, Al-27 (n,p) Mg-27, Fe-56 (n,p) Mn-56, Ta-181 (n,g) Ta-182, Sc-45 (n,g) Sc-46, Ni-58 (n,p) Co-58, Al-27 (n,a) Na-24. The appropriate samples have been prepared.

The samples activity after 3-hours irradiation by $4x10^9$ -yield Cf-source, located 30 cm below 3U irradiation end has been predicted. The evaluation of the activity was done for 18 mm in diameter and 1 mm thick samples.

The JET KN2 pneumatic system was improved. Some modifications of electronics, mechanics and power supply parts has been performed. Pressure valves, pipes and other supported systems were checked. All of the systems – pneumatic, electronic and mechanical seem to work correctly.

The activation samples have been prepared, the HPGe spectrometer has been brought to JET. Irradiation of the samples by means of the KN2 system could not be performed due to the cryoplant system fault in April 2012 which was followed by plasma discharges with too low neutron-yield.

Thermoluminescence detectors (TLD) were used for dose measurements at JET within JET FT-12-5.45. Several hundreds of LiF detectors of various types, standard LiF:Mg,Ti and highly sensitive LiF:Mg,Cu,P were produced. LiF detectors consisting of natural lithium are sensitive to slow neutrons, their response to neutrons being enhanced by ⁶Li-enriched lithium or suppressed by using lithium consisting entirely of ⁷Li. Pairs ⁶LiF/⁷LiF detectors allow distinguishing between neutron/non-neutron components of radiation field. For detection of neutrons of higher energy there is a need of moderators. Cylindrical moderators (25 cm diameter and 25 cm height) have been produced from polyethylene (PE-300) rods. All TLDs, located in the centre of cylindrical moderators, were installed at eleven positions in the JET hall and the hall labyrinth in July 2012, and exposure took place during the last two week of experimental campaign. Measurements of the gamma dose and of the neutron fluence were obtained for all positions over a range of about five orders of magnitude variation. The experimental results are compared with calculations using MCNP code. The results confirm that the TLD technology can be usefully applied to measurements of neutron streaming through JET Torus Hall ducts. New detector positions, further in the labyrinth and ducts, will be investigated in the next measurement campaign.

Preliminary simulation results of JET ILW discharges with COREDIV code

The self-consistent simulations of the core and the SOL plasma using the COREDIV code for JET H-mode plasmas with nitrogen seeding (JET#82031-82033) have been performed. In addition, a JET high power discharge without impurity seeding has been analysed in order to clarify discrepancies in the W concentrations coming from the experimental measurements and simulations.

Calculations have been done for different levels of the beryllium fluxes in order to fit into measured Zeff values. It appears that the low Z impurity Be determines the measured Zeff, whereas the tungsten impurity is responsible for the radiation losses in the core. About 5 MW is radiated by tungsten in the core, whereas the edge radiation due to hydrogen and beryllium amounts to 2.7 MW, giving the total radiation as observed in the experiment (shot#82875). The calculated concentration of tungsten was 4e-5 and appeared to be about 10 times larger than experimental estimations. After more detailed analysis of the experimental data (bolometric reconstruction of the radiation profiles) it became apparent, that the tungsten radiation in the core is not uniform and strongly shifted to the outer midplane region. This position is not seen by the KT7 diagnostic which was used to calculate tungsten concentrations and therefore reported values of tungsten concentration were much smaller than in simulations.

The reasons for the tungsten accumulation at the outer midplane are not fully clear but one of possible explanations might be related to the centrifugal force effect. However, this idea requires still experimental confirmation and should be further investigated.

The dependence of the results of the modelling of JET discharges on the assumed transport coefficients profiles has been studied numerically as well. The transport coefficients profiles were taken from the standard Bohm-gyro Bohm model and from the COREDIV model. The numerical results have demonstrated that the global parameters of plasma remain close to each other for the two different transport models.

Conclusion

As a results of the involvement of IPPLM staff in the campaigns C29-C30 the four papers were published.

References:

- [1] "Impurity studies in ITER half-field ICRF heating scenarios in Hydrogen plasmas on JET", A. Czarnecka et al.. Presented at 10th Kudowa Summer School in June 2011.
- [2] "Impurity behaviour during ICRH and NBI operation with ITER-like wall at JET", A. Czarnecka et al.. Presented at 39th European Phys. Society Conf. on Plasma Phys. (EPS2012) in July 2012.

- [3] J. Rzadkiewicz, W. Dominik, M. Scholz, K-D. Zastrow M. Chernyshova, T. Czarski, H. Czyrkowski, R. Dabrowski, K. Jakubowska, L. Karpinski, G. Kasprowicz, K. Kierzkowski, K. Pozniak, Z. Salapa, W. Zabolotny, P. Blanchard, S. Tyrrell, and JET EFDA Contributors, *Novel design of triple GEM detectors for high-resolution X-ray diagnostics on JET*, 2nd International Conference Frontiers in Diagnostic Technologies, 28-30 November, Frascati, Italy, Poster P-2.33.
- [4] K. Jakubowska, J. Rzadkiewicz, W. Dominik, M. Scholz, K-D. Zastrow, M. Chernyshova, T. Czarski, L. Karpinski et al., "Development of a 1D Triple GEM X-ray detector for a high-resolution X-ray diagnostics at JET", 38th European Physical Society Conference on Plasma Physics, 27 June 01 July 2011, Strasbourg France, Participant Booklet, Poster P2.036.

High power ICRH operation with metallic plasma facing components

Agata Czarnecka (agata.czarnecka@ipplm.pl) Institute of Plasma Physics and Laser Microfusion

Abstract

Additional heating systems can be a source of impurities in fusion plasmas. Studying the behaviour of such impurities is important to understand and minimize their effects on tokamak plasma performance. The impurity release during Ion Cyclotron Resonance Heating (ICRF) operation was investigated in the full Tungsten (W) wall ASDEX Upgrade (AUG) tokamak. This contribution mainly focuses on documenting the W behaviour in the plasma. Long-term observation of W concentration in AUG plasma during ICRH showed reduction of the W content in the plasma with pulse number. Results of the experiments carried out on AUG aiming at the characterization of the effect of different gasses injection such as deuterium, neon and argon, on W release is presented. In all cases the increase of gas injection rate caused decrease in the W concentration. The experiments with the boron-coated ICRH antennas limiters confirmed the dominant role of the limiters as W sources and showed an improved operation with the W-wall. Additionally in ICRH discharges, the influence of the plasma shape was investigated. At higher plasma outermost position, when the plasma was closer to the antenna, the higher W concentration was observed.

Introduction

Tungsten is moving back into the focus of spectroscopy for fusion plasmas because it is planned to be used as a plasma facing components (PFC) in ITER [1] and a future fusion reactor. As sputtering at the surfaces with plasma contact cannot be avoided completely, tungsten will be an intrinsic impurity in these plasmas. During the Ion Cyclotron Resonance Heating (ICRH) operation in high-Z machines, such as the full tungsten (W) ASDEX Upgrade (AUG) the impurities released from the wall contributes to radiation losses from the central plasma. The high-Z impurities need to be controlled within tolerable limits, to ensure they do not significantly affect the performance of the plasma. This requires the mitigation of impurity generation at ICRH antennas, improving the understanding of RF sheaths both experimentally and theoretically. This includes testing new antenna concepts, improving coupling and acting on sheaths by appropriate edge plasma / neutral gas pressure modifications, e.g. by gas injection. Investigation of the reduction of central impurity concentration by RF heating. Experimental data from AUG allowed characterization of the processes occurring in the specific ICRF plasma wall interaction, which need to be understood in order to maximize ICRF power in ITER.

Experimental arrangement

AUG is a divertor tokamak with a full-tungsten first wall with $R_{\text{maj}} < 1.65$ m, $R_{\text{min}} < 0.5$ m, $B_T < 3.1$ T, $I_p < 1.6$ MA and pulse duration < 10 s. AUG has an ICRH system with four antennas, known as antenna a1, a2, a3, and a4. Each antenna comprises two straps which are normally configured with a with (0 p) strap phasing and the H minority scheme. During the experiments in 2011 antennas a1 and a3 located opposite to each other were paired to allow independent feeding of neighboring antennas, and, similarly, antennas a2 and a4. However for some of the experiments a1 and a2 formed antenna pair(s) to allow direct comparison between a3 (original) and a4 (broad limiter) [2]. During 2012 experimental campaign the side limiters of a1 and a2 antenna were coated by a 50 μ m thick layer of boron prior to the installation in the vessel. Fig. 1 is a top view of the tokamak showing the four ICRH antennas used during the 2012 experiments.

For the whole 2012 experimental campaign, both antennas a1 and a2 with the boron-coated limiters were connected as a pair within the 3dB hybrid connection scheme, whereas a3 and a4 were connected as the other pair. This allowed a discrete operation of the antennas with the boron-coated limiters and of the antennas with the W-coated limiters.

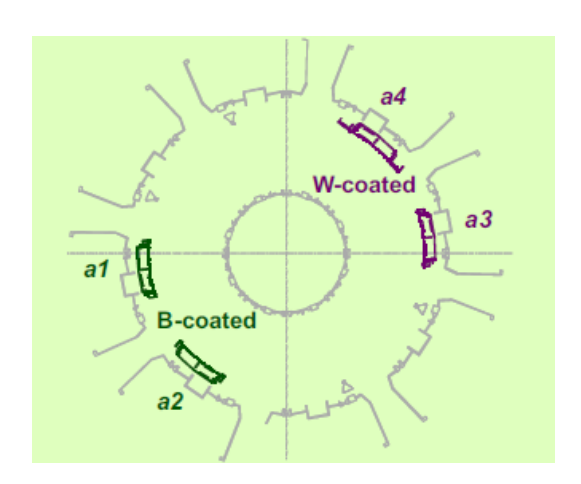


Fig. 1. Top view of AUG showing the location of the ICRH antennas [2]

Tungsten can only be diagnosed in AUG by passive spectroscopy in the vacuum ultraviolet (VUV) range. Analysis was performed base on the spectroscopic observations of W continuum and line radiation. Two quasi-continuos spectral features of tungsten are of main interest. One emission around $\lambda = 5$ nm originates from ionization stages Z = 28-35 existing around $T_e \sim 1.0$ keV. This emission is used routinely for tungsten concentration measurements. Another emission in the range $\lambda = 13\text{-}25$ nm is emitted by ionization stages $Z \leq 27$, which corresponds to electron temperature below 1.0 keV.

Experimental results

Averages of W concentration were calculated in time ranges with ICRF for all pulses during 2011 and 2012 experimental campaign in H-mode D-plasma. Long-term observation of W concentration in AUG plasma during ICRH showed the reduction of the W content in the plasma with pulse number for each campaign as is presented in Fig.2. Most of the pulses were with ICRH power 2 or 4 MW.

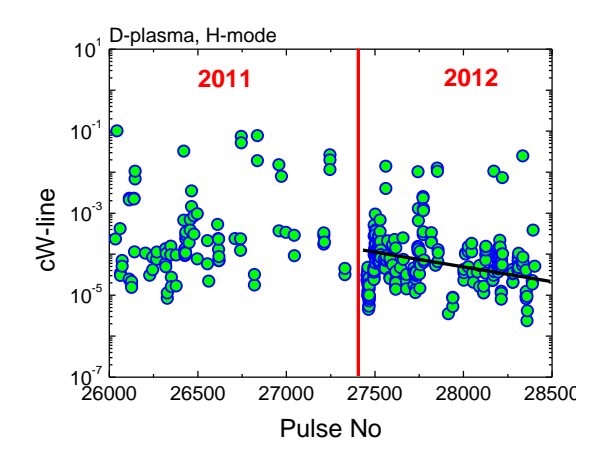


Fig. 2. Tungsten concentration in H-mode deuterium AUG plasma determined from the continuum radiation vs. pulse number in 2011 and 2012 experimental campaign.

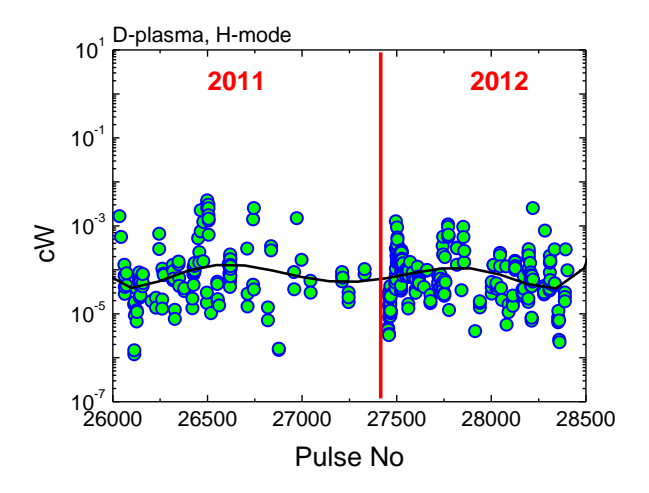


Fig. 3. Tungsten concentration in H-mode deuterium AUG plasma determined from the line radiation vs. pulse number in 2011 and 2012 experimental campaign

As a short-term solution for the reduction of impurity realise from the ICRH antennas, the boron-coated antenna side limiters have been tested in 2012. The influence of the boron and W coatings ICRF antenna limiters on W release during ICRF has been investigated. The antenna limiters play a dominant role as a W source during application of ICRF power. It was observed that the implementation of boron coatings on the ICRF antenna limiters reduced W release during ICRF.

The effect of gas injection on W release during ICRF has been investigated. The stress was put mainly on N_2 , D_2 , and Ar gas puff. The W content was reduced by injecting N_2 gas puff in the range 10^{21} - 10^{22} el/s, however at the low gas injection rate conditions (10^{18} - 10^{19} el/s), W concentration increased in the plasma (see Fig.4). In both cases the highest W concentration was observed during W-coated antenna operation. Reduction of central W impurity concentration with the D_2 and Ar gas injection with RF heating has been observed (see Fig.5 and 6). It was also observed that during D_2 injection, the W content was lower when boron-coated antenna was in use. For the constant D_2 injection rate and ICRF heating power, the W concentration decreased with the core electron density (see Fig.7).

Additionally in ICRF discharges, the influence of the plasma outermost position and main plasma shape by changes in upper and lower triangularity on the W content has been investigated. At higher plasma outermost position, when the plasma is closer to the antenna, the higher W concentration has been observed Results from ASDEX Upgrade showed that ICRF system leads to high W content in plasma due to W sources at the main wall components, in particular at antenna limiters.

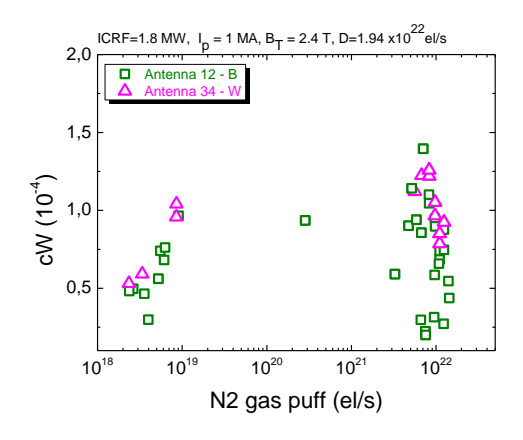


Fig. 4. Correlation between W concentration and N_2 gas injection rate in AUG during operation boronand tungsten- coated ICRH antennas

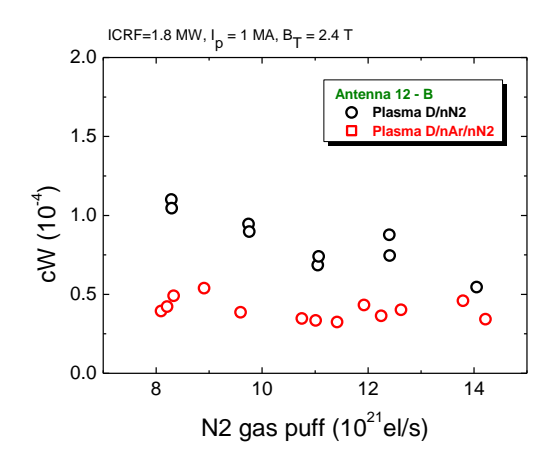


Fig. 5. W concentration vs. N₂ gas puff for D/nN2 and D/nAr/nN2 AUG plasma.

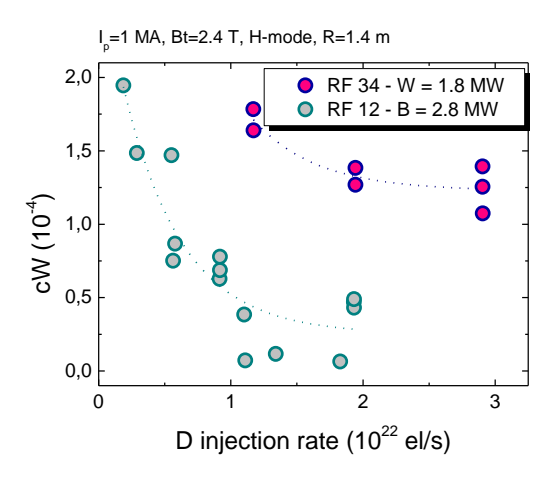


Fig. 6. Correlation between W concentration and deuterium gas injection rate for different antennas and ICRH power

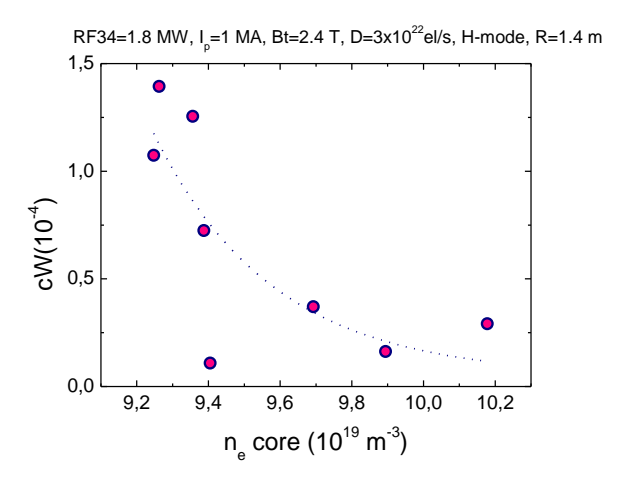


Fig. 7. Correlation between W concentration and core electron density for constant heating power and gas injection rate

Conclusions

The conducted research allows to state that operation of ICRF antennas in magnetic fusion experiments is often accompanied by enhanced plasma-surface interactions. The antenna limiters play a dominant role as a W source during application of ICRF power. The ICRF antennas in ASDEX Upgrade with boron-coated limiter have shown an improved operation with the W-wall. Spectroscopic measurements indicated lower rise of W concentration in the plasma with ICRF power. The effect of gas injection seems to have beneficial effect on the ICRF plasma performance. The influence of the location of the gas inlets and edge plasma modification on W sputtering during ICRF operation needs to be investigated. In near future, experiments are planned with completely new antenna design with the aim to minimize the antenna near fields for a reduction of the W sources.

Collaboration

Association EURATOM – Max-Planck-Institut für Plasmaphysik, Garching Association EURATOM – CEA

References

- 1. R. Aymar, P. Barabaschi and Y. Shimomura, Plasma Phys. Control. Fusion 44 (2002) 519
- 2. V. Bobkov et al. "ICRF Operation with Improved Antennas in a Full W-wall ASDEX Upgrade, Status and Developments", 24th IAEA Fusion Energy Conference, San Diego, USA, 8-13 October 2012, EX/P5-19

2.5 Inertial Fusion Energy "keep-in-touch" activity

Particle-in-Cell simulations of laser-driven ion acceleration for fast ignition of inertial fusion targets

Jan Badziak (jan.badziak@ipplm.pl), Sławomir Jabłoński, Piotr Rączka Institute of Plasma Physics and Laser Microfusion

Abstract

Particle-In-Cell simulations were performed to investigate the usefulness of the concept of the cavity-enhanced laser driven ion acceleration, which might be relevant for fast ion ignition. In this approach the foil target is enclosed in a cavity and the laser light reflected from the target is redirected back into the target through reflections at the inner cavity wall. A one-dimensional simulation indicates that for laser intensities of the order of 10^{21} W/cm² this approach may lead to at least doubling of the accelerated ion energies.

Introduction

The ion fast ignition is a promising method considered for the ignition of pre-compressed D+T inertial fusion targets. It is predicted to require a significantly smaller overall energy for compression and ignition of the fuel pellet as compared to the central hot spot ignition. It is also predicted to give higher fusion gain, which is a consequence of the fact that the fusion fuel is ignited at much higher density. On the other hand, the requirements for the ion beam to be used for fast ignition are very demanding, since it is necessary to deliver the energy of 10-20 kJ in the time interval of 10-20 ps to the fuel region of the size of 20-50 μ m.

The only acceleration mechanism that might hopefully lead to the beam with such parameters is laser-driven ion acceleration. However, a major challenge on the road to practical laser-driven ion fast ignition is the issue of the laser-to-ion energy conversion efficiency, which should be greater than 10%, since otherwise the energy of the igniting laser beam would have to exceed 100 kJ, which is considered to be technologically difficult to achieve in the near future.

Results

An original method to increase the laser-to-ion energy conversion efficiency was proposed by IPPLM laser plasma group. The main idea of this method is to enhance the initial pulse through reflections at the inner wall of the cavity. The method was dubbed Laser-Induced Cavity Pressure Acceleration (LICPA). It relies on the observation that at high laser intensities the beam reflected from the target is also quite high intensity. If we enclose the irradiated foil target inside a cavity, a significant part of the reflected laser energy – which otherwise would be lost – would be redirected towards the foil and converted into the ion energy. In other words, in the idea of the LICPA approach is to "recycle" the reflected laser energy.

The LICPA approach gave very good results in experiments on plasma acceleration at laser intensities of the order of 10^{16} W/cm² [1], so it was tempting to test this approach at much higher intensities, of the order of 10^{20} - 10^{21} W/cm², which are relevant for the fast ignition [1,2].

To this end a numeric simulation was performed of laser the interaction with a solid target enclosed in a cavity. At such high intensities and short durations of the laser pulse plasma is essentially collisionless. Dynamics of such plasma lends itself well to modelling using the Particle-in-Cell (PIC) method, in which the ion and electron distributions are discretized and approximated by the distribution of macroparticles interacting via electromagnetic fields. Because of high numerical complexity of the considered problem it was assumed initially that all plasma parameters depend on only one spatial variable (although all three components of plasma velocities are retained). The PIC code created for this

simulation takes fully into account the relativistic character of macroparticle dynamics and of the electromagnetic fields created by them. The simulation is set in the following way: a pulse of circularly polarized laser light with the wavelength 1.06 μ m, the temporal profile $I(t) = I_L \exp(-t^6/\tau^6)$, duration of 2 ps and intensity of 10^{21} - 10^{22} W/cm² is introduced into the cavity of the depth in the range of 40-160 μ m, where it interacts with a foil of few micrometer thickness, which for the purpose of the simulation is assumed to be a totaly ionized plasma with the ion number density 10^{23} cm⁻³. The radiation reflected from the target is redirected back into the target through the reflection at the inner cavity wall, where it was assumed that about 40% of the incident radiation is absorbed, independently of the beam intensity. A thorough investigation was performed for the carbon target [2], since carbon ion beams are a very serious candidate for the fast ion ignition.

In Fig. 1 we show the energy spectra of carbon ions accelerated according to the LICPA method, for various depths of the cavity, compared with the spectrum obtained without the cavity. The use of the LICPA mechanism results in a nearly doubling of the average ion energy in the beam, although the energy dispersion is also slightly bigger.

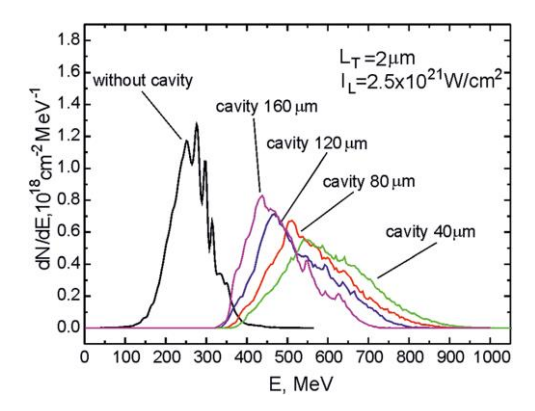


Fig. 1. Energy spectra of carbon ions accelerated according to the LICPA method with cavity depth varying from 160 μ m to 40 μ m, compared with the spectrum obtained in the absence cavity. The carbon foil was 2 μ m thick, the laser intensity was 2.5×10^{21} W/cm² and the acceleration length was 150μ m.

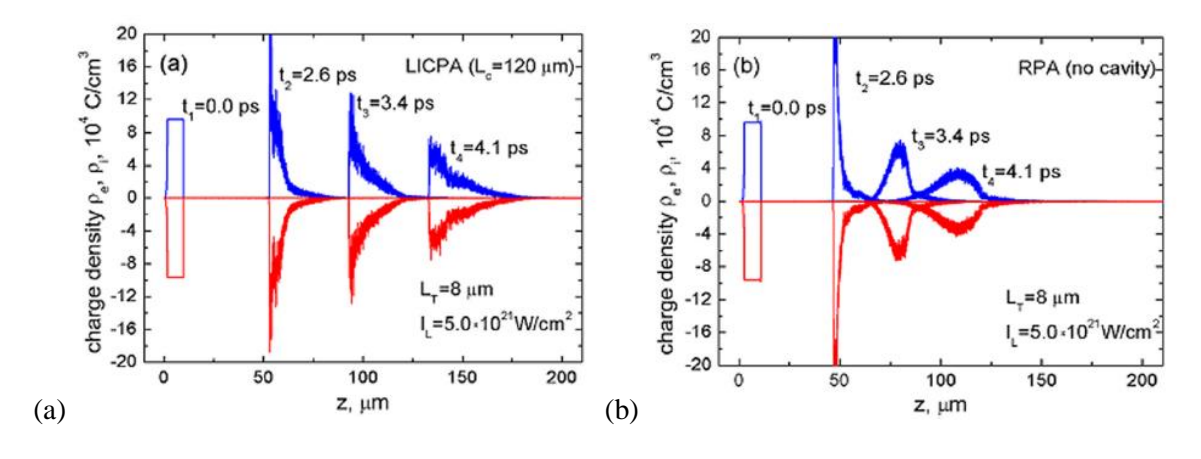


Fig. 2. Spatial distribution of the positive and negative charge for 8 μ m carbon foil irradiated by the laser beam of intensity 5×10^{21} W/cm²: a) in the LICPA approach with the cavity 120 μ m deep; b) in the absence of cavity.

The spatial distribution of the accelerated ions is shown in Fig. 2 in the case of 8 μ m carbon target irradiated by the beam of intensity 5×10^{21} W/cm². Differences between LICPA acceleration and direct acceleration are clearly visible, particularly after the acceleration time longer than duration of the initial laser pulse. At these times in the LICPA scheme plasma is still being accelerated by the pulse reflected at the inner cavity wall, despite the fact that the initial pulse had subsided. This results in a visibly higher density and higher velocity of the plasma bunch.

In the process of acceleration the plasma bunch retains high density, which suggests that its dynamics might be close to that of a "laser sail" (LS). The relativistic motion of a thin foil of density ρ and thickness d, driven by the laser beam of intensity I(t) in the rest frame of the laser, which undergoes a complete reflection in the rest frame of the foil, is described by a simple equation:

$$\frac{\gamma}{1-\beta} \frac{d\beta}{dw} = \frac{2I(\frac{w}{c})}{\rho dc^3}$$

where $\beta = v/c$, $\gamma = (1 - \beta^2)^{-1/2}$, and w = ct - x is the relativisitic retarded time. This equation may be solved also for the LICPA scenario. The energy transferred to the foil may be described by the formula [1,3]:

$$e^{(j+1)}(w) = e^{(j)}(w_j) + \frac{2}{\rho dc^3} \int_{w_j}^{w} I(w'/c) dw' + R_c \cdot \frac{e^{(j)}(w^{(j)}(w)) - e^{(j)}(w_{j-1}))}{(1 + e^{(j)}(w^{(j)}(w)))(1 + e^{(j)}((w_{j-1})))}$$

where w_j corresponds to the values of retarded time variable for which the beam is being reflected for the j-th time, and the coefficient R_c describes the energy reflection efficiency at the cavity wall. The speed of the foil may then be recovered from the formula

$$\beta^{(j)}(w) = \left[(1 + e^{(j)}(w))^2 - 1 \right] / \left[(1 + e^{(j)}(w))^2 + 1 \right],$$

It turns out that predictions of this generalized LS model are in surprisingly good agreement with the results of fully kinetic PIC simulations, both for the average ion energy per nucleon and for the average position of the plasma bunch. This is illustrated in Fig. 3, where the laser-to-ion energy conversion efficiency is shown as a function of the laser intensity. This good agreement between kinetic simulation and analytic model allows us to make quick estimates of the plasma bunch acceleration for a broad range of laser and target parameters. As we see, with the use of the LICPA cheme the laser energy conversion efficiency may be at least doubled in value.

Simulations were also performed for targets composed of H, Be and Al, with similar areal density as the carbon target. Results of these simulations are shown in Fig. 4. As we see, the average energy per nucleon and the laser-to-energy conversion efficiency show only a very weak dependence on the composition of the target.

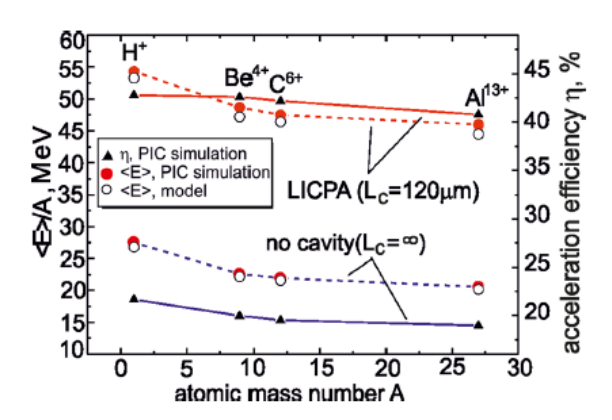


Fig. 4. Average ion energy per nucleon and laser-to-ion energy conversion efficienty, as a function of the atomic mass number of the target material, for areal target density 4×10^{-4} g/cm², duration of the pulse 2 ps and beam intensity 2.5×10^{21} W/cm². Open circles indicate results obtained from the generalized "laser sail" model.

Conclusions

Results of PIC simulations of the cavity-enhanced laser acceleration of ions (the LICPA mechanism) in one dimensional model are very encouraging. It would be of great interest to confront these results with the simulations carried out in two spatial dimension, which are however much more demanding from

INSTITUTE OF PLASMA PHYSICS AND LASER MICROFUSION

the numerical point of view. It seems also that it would be very interesting to perform an experiment on cavity-enhanced ion acceleration using a laser delivering intensities in the range of 10^{20} - 10^{21} W/cm² and the pulse energy of tens of joules.

References

- [1] J. Badziak, S. Jabłoński, T. Pisarczyk, P. Rączka, E. Krousky, R. Liska, M. Kucharik, T. Chodukowski, Z. Kalinowska, P. Parys, M. Rosiński, S. Borodziuk, J. Ullschmied, *Highly efficient accelerator of dense matter using laser-induced cavity pressure acceleration*, Phys. Plasmas 19, 053105 (2012).
- [2] J. Badziak, S. Jabłoński, P. Rączka, *Highly efficient generation of ultraintense high-energy ion beams using laser-induced cavity pressure acceleration*, Appl. Phys. Lett. 101, 084102 (2012).
- [3] P. Rączka and J. Badziak, A simple model for cavity-enhanced laser-driven ion acceleration from thin foil targets, arXiv: 1205.3670.

Collimated plasma jets generated from a target composed of foils with different atomic number

Tadeusz Pisarczyk (tadeusz.pisarczyk@ipplm.pl), Tomasz Chodukowski, Zofia. Kalinowska, Andrzej Kasperczuk, and Piotr Parys Institute of Plasma Physics and Laser Microfusion

Abstrac

A new method for creating collimated plasma jets moving in the direction of propagation of the laser beam is investigated. It is based on using a multi-layer target composed of thin metal foil and a thin plastic foil.

Introduction

Investigations performed at the PALS laser facility in Prague had shown promising results for a recently proposed method of generation of plasma jets by irradiation of massive planar targets with atomic number Z>29 (Cu) with a laser beam characterized by annular distribution of intensity. Combining massive targets of annular or multilayer structure, consisting of materials of both low and high atomic number, it proved possible to obtain a variety of plasma jets, which may be useful in a multitude of different applications.

In comparison with other methods of generation of collimated plasma jets – for example by irradiation of conical targets with multiple beams carrying large energy, which is possible only on the biggest laser systems – the advantage of the new method is its simplicity. However, the new method allows to create only jets moving in direction opposite to the laser beam incident on the target, which limits the range of possible applications.

A method to create plasma jets moving in the same direction as the incident laser beam would be more widely applicable, for example in investigations of the erosion of surfaces of various materials under the influence of strong plasma flows. Such investigations are necessary in order to assess the usefulness of various materials for future fusion reactors.

Results

The first attempts to create plasma jets moving in the direction of propagation of the laser beam involved Al, Ag and Ta foils with thickness in the range 0.5- $1.0~\mu m$. In order to generate an elongated plasma bunch with length bigger than its diameter it was necessary to irradiate the foil using the laser spot much bigger than the minimal attainable value.

The next step in the quest for plasma jets was to use composite multi-layer targets consisting of a thin metal foil (Cu) and a plastic foil (Fig. 1). The expectation was that radial expansion of metallic plasma would be constrained by the influence of light plastic plasma (CH), which was shown in previous experiments to achieve higher pressure, as discussed in [1].

For this scheme to succeed the metal foil had to be thin enough so as to evaporate under the influence of the laser pulse, which implied thickness in the range of 1 μ m for the Cu foil. The relation between pressures of the metal plasma and the plastic plasma could be controlled by varying the thickness of plastic (CH) layer: arrangements with 1, 2, 4 and 6 μ m plastic layers were examined.

In the experiments reported in this note the laser wavelength λ_1 =1315 nm was used (the first harmonic of the iodine laser) with the laser pulse energy approximately 500 J. The beam was focused down to R_L = 40-120 μ m. It should be noted, however, that due to thermal conduction the area of the foil being heated is much bigger, corresponding to $R_L \approx 600 \ \mu$ m.

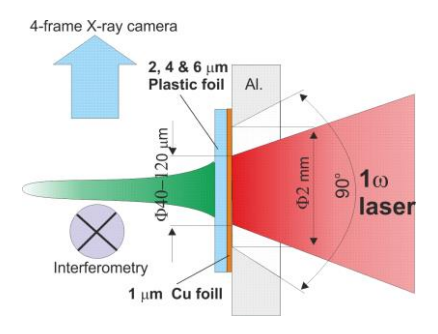


Fig. 1. A schematic illustration of generation of collimated plasma jets using composite targets consisting of a thin metal foil (Al or Cu) and a plastic foil

The interaction of the metal and plastic plasmas and the evolution of the created plasma jets was recorded using the 3-frame interferometry system utilising the second harmonic of the laser (658 nm). A sample of such interferograms is shown in Fig. 2.

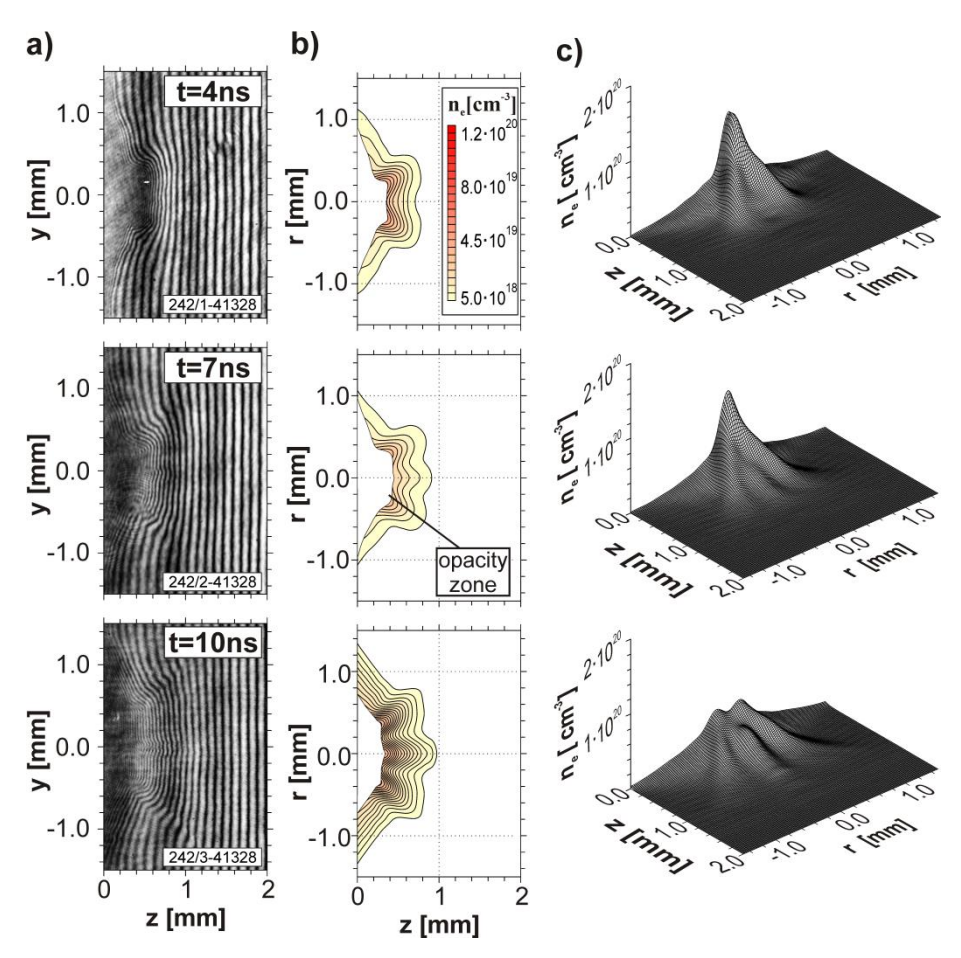


Fig. 2. Expansion of the composite plasma created by the 490 J laser pulse focused down to the spot of radius $R_L = 40 \mu m$, incident on a composite metal-plastic target: a) interferograms; b) isodensity curves; c) spatial profiles of electron concentration.

The most interesting result was obtained for a combination of 1 μ m Cu foil and 2 μ m plastic foil (Fig. 3). The sequence of electron density distributions obtained in this case at various times confirms the expectations concerning the influence of the higher pressure plastic plasma on the Cu plasma, which resulted in the formation of a collimated jet. For this target expansion of the Cu plasma in the initial period of plasma formation (t < 4 ns) was blocked by the higher pressure of the expanding plastic plasma. It is only in the second phase (t > 4 ns) that the radial expansion of the plastic plasma in centre, resulting

from higher temperature, reaches the level that allows for a window to be formed for the Cu plasma expansion. A channel is formed in the plastic plasma, which acts on the expanding Cu plasma as a nozzle. The stream of the metal plasma reaches the speed of 4×10^7 cm/s, with the electron number density reaching values of the order of 10^{18} - 10^{19} cm⁻³.

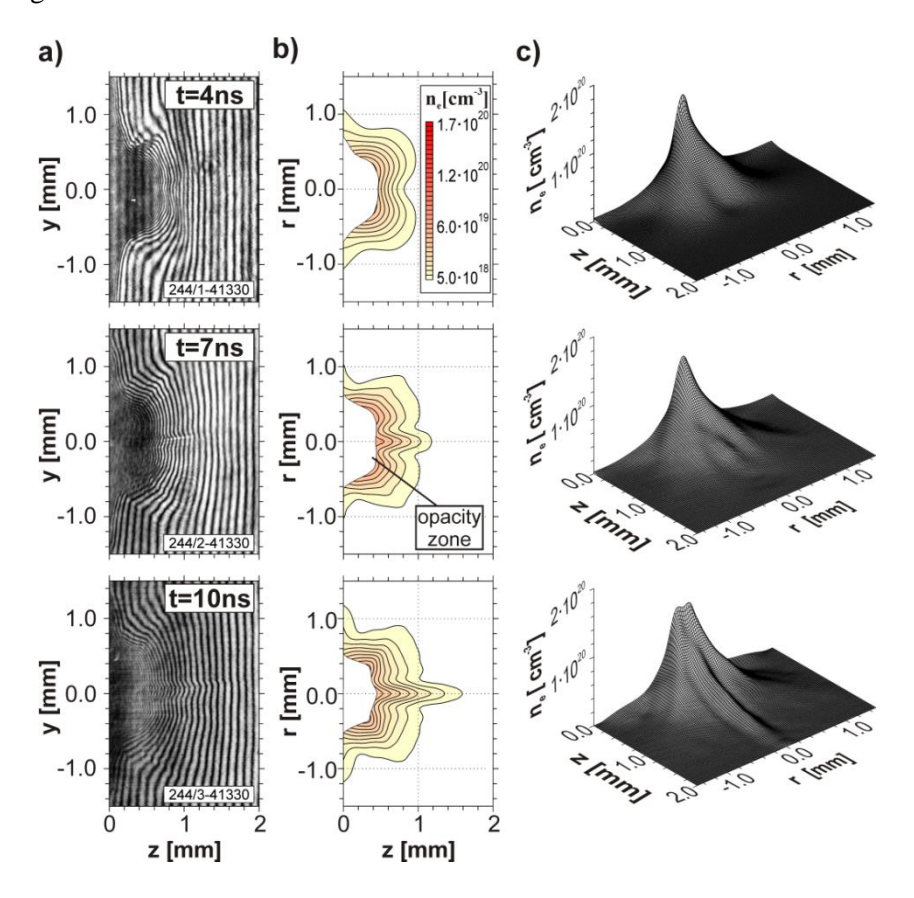


Fig. 3. Ejection of a collimated plasma jet under the influence of a laser beam with energy of 490 J, focussed down to $R_L = 40 \mu m$, irradiating a 1 μm thick Cu foil combined with 2 μm CH foil: a) interferograms; b) isodensity curves; c) spatial profiles of the electron concentration.

The process of formation of a collimated jet of metallic plasma is illustrated in Fig. 4.

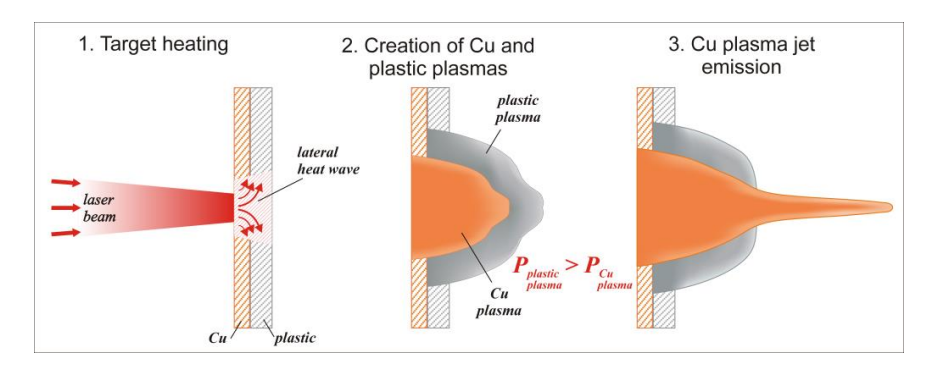


Fig. 4. Formation of a collimated jet of metallic plasma, moving in the direction of the incident laser beam, using a double-layer target consisting of metal and plastic foil

Conclusions

The results collected in a series of laser shots lead to following conclusions:

- a) A 1 μ m Cu foil is still too thick. This has the consequence that the plasma jet is formed too late, when the Cu plasma had already cooled down. Better results could be obtained if Cu foils of 0.1 μ m thickness were used.
- b) The relation between thickness of the Cu foil and the CH foil is important. If CH foil is too thin, the relatively small amount of CH plasma is not sufficient to ensure proper radial collimation of the Cu plasma. On the other hand, if the CH foil is too thick, the plastic plasma blocks the outflow of the Cu plasma.

Unfortunately, manufacturing of ultra-thin foils that might lead to improved results in future experiments involving this scenario of plasma jet generation is beyond present technical capabilities of IPPLM.

Results obtained within this project were presented at the 39-th EPS Conference on Plasma Physics in Stockholm, July 2012 [3].

Collaboration

Association EURATOM - IPP.CR

References

- [1] Kasperczuk, T. Pisarczyk, T. Chodukowski, Z. Kalinowska, P. Parys, O. Renner, S. Yu. Gus'Kov, N. N. Demchenko, J. Ullschmied, E. Krousky, M. Pfeifer and K. Rohlena: *Laser-produced aluminum plasma expansion inside a plastic plasma envelope*, Physics of Plasmas **19**, 092106 (2012).
- [2] A. Kasperczuk, T. Pisarczyk, T. Chodukowski, Z. Kalinowska, S. Yu. Gus'Kov, N. N. Demchenko, D. Klir, J. Kravarik, P. Kubes, K. Rezac, J. Ullschmied, E. Krousky, M. Pfeifer, K. Rohlena, J. Skala and P. Pisarczyk: *Plastic plasma as a compressor of aluminum plasma at the PALS experiment*, Laser and Particle Beams **30**, 1-7 (2012).
- [3] A. Kasperczuk, T. Pisarczyk, T. Chodukowski, Z. Kalinowska, J. Ullschmied, E. Krousky, M. Pfeifer, K. Rohlena, J. Skala, and P. Pisarczyk. *Methods of backward and forward formation of metallic plasma jets at PALS*, Proc. 39th EPS Conference & 16th Int. Congress on Plasma Physics, Stockholm, July 2 6, P4-128 (2012).